Doctoral Thesis

Physiological Control of Left Ventricular Assist Devices

Author(s):
Ochsner, Gregor M.

Publication Date:
2014

Permanent Link:

https://doi.org/10.3929/ethz-a-010252528 →

Diss. ETH No. 22061

PHYSIOLOGICAL CONTROL OF LEFT VENTRICULAR ASSIST DEVICES

A thesis submitted to attain the degree of

Doctor of Sciences of ETH Zurich
(Dr. sc. ETH Zurich)

presented by

Gregor Meinrad Ochsner

MSc ETH in Mechanical Engineering
born on 30.07.1985
citizen of Einsiedeln

accepted on the recommendation of
Prof. Dr. L. Guzzella
Prof. Dr. med. V. Falk.

2014

Gregor Meinrad Ochsner
gregor.ochsner@alumni.ethz.ch

ETH Zurich
Institute for Dynamic Systems and Control
Sonneggstrasse 3
8092 Zurich, Switzerland

Contents

Acknowledgments

This thesis is the result of an interdisciplinary research project between the Institute for Dynamic Systems and Control at ETH Zurich, the Clinic for Cardiovascular Surgery at the University Hospital Zurich, the Clinic for Cardiovascular Surgery at Bern University Hospital (Inselspital), and the ARTORG Center for Biomedical Engineering Research at the University of Bern.
First and foremost, I want to express my deepest gratitude to Prof. Dr. Lino Guzzella for accepting me as a PhD student and for his guidance during my doctoral studies. Next, I wish to thank Prof. Dr. med. Volkmar Falk for accepting to be my co-examiner and for his support during the last two years of my doctoral studies.
Furthermore, I thank the collaborators of our research project, namely the cardiac surgeons PD Dr. med. André Plass, Prof. Dr. med. Hendrik Tevaearai, and PD Dr. med. Markus Wilhelm for sharing their clinical experience with us and PD Dr. Stijn Vandenberghe for helping us with his expertise as well as with the many devices he let us borrow. I thank Dr. Alois Amstutz for supporting me with his profound knowledge in almost any field.
Moreover, I thank Dr. Marianne Schmid Daners for supervising our research project, for her constant support, and for keeping all obstacles out of my way. I also thank Dr. Christopher Onder for managing the Institute and for sharing his profound scientific knowledge with me.
Furthermore, I wish to express my gratitude to all my colleagues at our Institute for their invaluable help and their great company. Most of all, I owe my thanks to Dr. Raffael Amacher for being the smart, calm, and helpful colleague and person that he is. The current thesis would not have been possible without him.
I also wish to thank Alex Braun, David Brühlmann, Daniel Burch, Marc-André Corzillius, Gregy Huber, and Daniel Wagner for setting up the hybrid mock circulation, Brigitte Rohrbach for carefully revising my papers as well as this thesis, and Annina Fattor, Kerstin Fischer, Barbara Kornexl, Katharina Munz, Aleksandra Müller, and Claudia Wittwer for their kind help with all my administrative problems.

Abstract

This thesis describes a physiological controller for turbodynamic ventricular assist devices (VADs). VADs are blood pumps that are implanted in patients with severe heart failure and can be used temporarily until a later heart transplantation or permanently as an alternative to heart transplantation. Typically, VADs are implanted between the left ventricle (LV) and the aorta.

The flow generated by turbodynamic VADs depends on the speed of the rotor. In current clinical practice, this speed is chosen by the physician and is kept constant. Changes in the hemodynamic status of the patient can render the chosen pump speed inappropriate such that undesired and potentially harmful events like over- or underpumping can occur. Therefore, it is desirable to have an automatic control algorithm that matches the flow generated by the pump to the perfusion requirement of the patient and that effectively avoids over- and underpumping.

A preload sensitive speed (PRS) controller is developed in order to achieve a physiological adaptation of turbodynamic VADs. This controller changes the pump speed according to the end-diastolic volume of the LV. The control law behind the PRS controller is inspired by the Frank-Starling law of the heart and thereby closely imitates the human physiology. In vitro experiments show that the behavior of the PRS-controlled VAD is very similar to the behavior of the native heart. Thus far, however, no experiments have been conducted in vivo.

The introduction of an LV volume feedback in the PRS controller is necessary to compensate for unknown disturbances. However, since feedback can lead to instability, a stability analysis of the PRS controller was conducted. A simplified model of the circulation and the VAD was implemented with a wide range of parameter combinations and its stability was investigated using the Nyquist criterion. For all parameter combinations, the closed loop system proved to be stable with a minimum gain margin of 3 and an infinite phase margin.

In order to obtain physiological experimental results in vitro, a hybrid mock circulation was developed. It combines a numerical model of the human cardiovascular system with a real hydraulic blood pump. The numerical-hydraulic interface between the numerical model and the pump consists of two pressure-controlled reservoirs and a flow probe, which en-

able a real-time interaction of the two parts. The hybrid mock circulation shows an unmatched physiological behavior, is very flexible, and allows for a wide range of testing scenarios.

Zusammenfassung

Diese Dissertation beschreibt einen physiologischen Regler für eine turbodynamische Herzunterstützungspumpe. Solche Pumpen werden in Patienten und Patientinnen implantiert, welche an schwerer Herzinsuffizienz leiden. Sie werden entweder temporär, bis zu einer späteren Herztransplantation oder permanent, als Alternative zur Herztransplantation eingesetzt. Herzunterstützungspumpen werden hauptsächlich zwischen dem linken Ventrikel (LV) und der Aorta implantiert.
Der Fluss, den eine turbodynamische Pumpe erzeugt, hängt unter anderem von der Drehzahl der Pumpe ab. Im klinischen Alltag wird die Drehzahl vom Arzt bestimmt und konstant gehalten. Wenn sich der hämodynamische Zustand des Patienten oder der Patientin in dieser Zeit ändert, passt die eingestellte Drehzahl jedoch nicht mehr zu diesem Zustand. Dabei können unerwünschte Phänomene wie Überpumpen oder Unterpumpen auftreten, welche für den Patienten oder die Patientin eine Gefahr darstellen. Deshalb soll ein physiologischer Regler in eine solche Pumpe integriert werden, welcher den Fluss durch die Pumpe automatisch dem Bedarf des Patienten anpasst und dabei Über- sowie Unterpumpen verhindert.
In dieser Dissertation wird ein vorlastsensitiver Geschwindigkeitsregler beschrieben, welcher die Drehzahl einer turbodynamischen Herzunterstützungspumpe anhand des gemessenen enddiastolischen Volumens des LV anpasst. Der Regler wird in der ganzen Dissertation als PRS-Regler bezeichnet. Das Regelgesetz des PRS-Reglers ist vom Frank-Starling-Mechanismus inspiriert und imitiert damit das Verhalten des menschlichen Herzens. In-vitro-Experimente bestätigen, dass das Verhalten des PRS-Reglers dem Verhalten des gesunden Herzens tatsächlich sehr ähnlich ist. In-vivo-Experimente wurden mit dem PRS-Regler bisher noch keine durchgeführt.
Um unbekannte Störungen zu unterdrücken, braucht der PRS-Regler eine Rückführung des gemessenen LV Volumens. Da das Schliessen des Regelkreises jedoch zu Instabilität führen kann, wurde für den PRS-Regler eine Stabilitätsuntersuchung durchgeführt. Dazu wurde ein vereinfachtes Modell des Herz-Kreislaufsystems und der Herzunterstützungspumpe implementiert, welches mithilfe des Nyquistkriteriums auf Stabilität untersucht werden kann. Der geschlossene Regelkreis ist für alle untersuchten Parameterkombinationen stabil und weist eine Verstärkungsreserve von mindestens 3 und eine unendliche Phasenreserve auf.

Um in vitro verlässliche physiologische Resultate zu erhalten, wurde ein neuartiger, hybrider Blutpumpenprüfstand entwickelt. Dieser Prüfstand besteht aus einem numerischen Modell des menschlichen Herz-Kreislaufsystems und einer echten hydraulischen Blutpumpe. Das numerisch-hydraulische Interface, bestehend aus zwei druckgeregelten Behältern und einer Flussmesssonde, ermöglicht eine Echtzeitinteraktion zwischen dem numerischen Modell und der Pumpe. Dieser hybride Blutpumpenprüfstand zeigt ein bisher unerreichtes physiologisches Verhalten, ist sehr flexibel und eignet sich für eine Vielzahl unterschiedlicher Experimente.

Nomenclature

Symbols

C	Compliance	$[\mathrm{mL}/\mathrm{mmHg}]$
$C(s)$	Controller	
$e(t)$	Controller input error signal	
f	Frequency	[Hz]
$h(t)$	Pump pressure head	[mmHg]
$I(t)$	Pump motor current	[A]
k	Gain	
L	Intertance	$[\mathrm{mmHg}\cdot\mathrm{s}^2/\mathrm{mL}]$
$\overset{*}{m}(t)$	Air-mass flow	$[\mathrm{g}/\mathrm{s}]$
$N(t)$	Rotational speed	[rpm]
$p(t)$	Pressure	[mmHg] or [Pa]
$P(s)$	Plant	
$P(t)$	Power	[W]
$q(t)$	Flow	$[\mathrm{mL}/\mathrm{s}]$ or $[\mathrm{L}/\mathrm{min}]$
$r(t)$	Controller reference signal	
r	Suction resistance gain	$[\mathrm{s}/\mathrm{mL}]$
$R(s)$	Laplace transform of r(t)	
R	Resistance	$[\mathrm{mmHg}\cdot\mathrm{s}/\mathrm{mL}]$
s	Laplace variable	$[\mathrm{s}^{-1}]$
t	Time	[s]
T/τ	Time constant	[s]
$T(s)$	Complementary sensitivity	
$u(t)$	Controller output signal	
$v(t)$	Nonlinear plant input signal	
$V(t)$	Volume	[mL] or [L]
$w(t)$	Nonlinear plant output signal	
$W(t)$	Work	[J]
$x(t)$	Suction index signal ($q(t)$, $I(t)$, or $h(t)$)	
$X(f)$	Fourier transform of $x(t)$	

$y(t)$	Controlled feedback signal	
$Y(s)$	Laplace transform of $y(t)$	
$z(t)$	Nonlinear plant state vector	
α	Inverse of lead magnitude gain	
δ	Damping	
Δ	Difference	
Π_{ind}	Pulsatility index	[mmHg]
σ	Standard deviation	
Θ_{ind}	Harmonic index	
$\varnothing$	Diameter	[m]

Indices

a	Active
ao	Aorta
arw	Anti-reset windup
av	Aortic valve
b	Baroreflex
co	Cardiac output
d	Derivative
des	Desired
dia	Diastole
ds	Downstream
ed	End diastolic
filt	Filtered
fl	Fluid level
gs	Gain scheduling
i	Integral
ind	Index
iv	Inlet valve
l	Lead / linear
la	Left atrium
lp	Low pass

lv	Left ventricle
max	Maximum
mv	Mitral valve
n	Normalized
ov	Outlet valve
p	Pressure / passive / proportional / pump
pa	Pulmonary arteries
pi	Pump inlet
prsw	Preload recruitable stroke work
pv	Pulmonary valve
q	Quadratic
ra	Right atrium
raw	Unfiltered
res	Resistance
rot	Rotor
rpa	Pulmonary arterial resistance
rsa	Systemic arterial resistance
rv	Right ventricle
s	Speed / sampling
sa	Systemic arteries
sp	Setpoint
suc	Suction
sv	Systemic veins
sys	Systole
th	Suction threshold
tv	Tricuspid valve
tve	Time-varying elastance
us	Upstream
vad	Ventricular assist device
vp	Pulmonary veins

Acronyms and Abbreviations

CO	Cardiac output
EDV	End-diastolic volume
HQ	Pressure head vs. pump flow
HR	Heart rate
IIR	Infinite impulse response
LA	Left atrium
LV	Left ventricle
MCS	Mechanical circulatory support
MIMO	Multiple-input multiple-output
PC	Personal computer
PI	Proportional-integral
PID	Proportional-integral-derivative
PMMA	Polymethyl methacrylate
PPLUT	Pump power lookup table
PRS	Preload responsive speed
PRSW	Preload recruitable stroke work
PV	Pressure volume
RA	Right atrium
RGA	Relative gain array
RMS	Root mean square
RV	Right ventricle
SISO	Single-input single-output
VAD	Ventricular assist device

Chapter 1

Introduction

1.1 Physiology of the human cardiovascular system

This section summarizes the physiology of the human cardiovascular system with a focus on hemodynamics and blood flow regulation. For an in-depth introduction to the physiology of the cardiovascular system, see [1]. The current thesis investigates the physiological control of left ventricular assist devices (VADs), i.e., the description in the current section is focused on the left side of the heart.

1.1.1 Hemodynamics

The main purpose of the cardiovascular system is the distribution of oxygen and nutrients to all tissues of the body. The cardiovascular system consists of the right and the left sides of the heart as well as the systemic and the pulmonary circulations. Figure 1.1 shows a schematic diagram of the human cardiovascular system. The pulmonary circulation leads deoxygenated blood from the right ventricle (RV) through the pulmonary arterial tree into the lungs, where the blood is enriched with oxygen. From there, the blood flows through the pulmonary veins into the left atrium (LA). The systemic circulation leads oxygenated blood from the left ventricle (LV) through the aorta, the arteries, and the arterioles into the capillaries, where the oxygen is transferred to the surrounding tissue. From there, the deoxygenated blood flows through the systemic veins into the right atrium (RA).

Figure 1.2 shows a sketch of the human heart. Each side of the heart consists of an atrium and a ventricle. The ventricles are the main pumping chambers, while the atria act as primer pumps to improve the filling of the ventricles. Unidirectional flow valves are located at the inlets and outlets of the ventricles. The valves of the RV are called tricuspid and pulmonary valve; the valves of the LV are called mitral and aortic valve.

Throughout the cardiac cycle, the heart muscle contracts and relaxes, which–together with the unidirectional flow valves–results in a pumping function of the ventricles. The filling phase of the ventricle is called diastole; the ejection phase is called systole. Figure 1.3 shows the pressure-volume (PV) diagram of the LV, which illustrates the relationship between pressure and volume in the LV during one cardiac cycle. Figure 1.4 shows the time course of the pressures in the LV, the LA, and the aorta over two

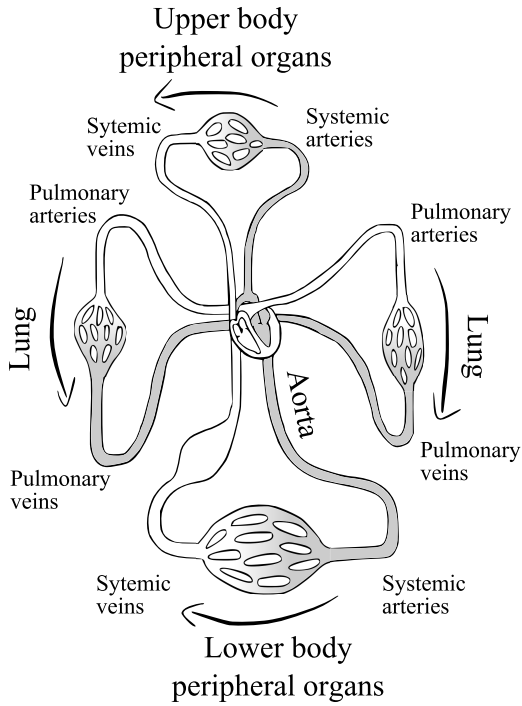

Figure 1.1: Schematic diagram of the human cardiovascular system. The heart is located in the center. The pulmonary circulation consists of the pulmonary arterial system, the pulmonary venous system, and the microcirculation in the lungs. The systemic circulation consists of the systemic arterial system, the systemic venous system, and the microcirculation in the peripheral organs. The grey color indicates where the oxygen level in the blood is high. The bump in the systemic veins of the lower body indicates that more than 60% of the total blood volume is stored in these vessels.

consecutive cardiac cycles. Figures 1.5 and 1.6 describe the diastole and the systole of the LV in more detail.

Both the systemic and the pulmonary circulations can be divided into three parts: the arterial system, the microcirculation, and the venous system. The purpose of the large arterial vessels is the efficient transport of blood and a low-pass filtering of the flow. The former is achieved by a large vessel diameter of around 30 mm, while the latter is achieved by the Windkessel effect, which is a result of the distensible vessel walls [2].

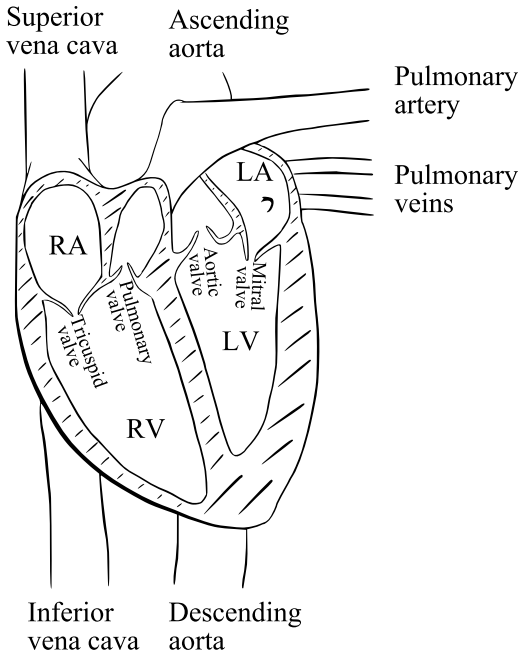

Figure 1.2: Sketch of the human heart with the four heart chambers, the valves, and the connecting vessels. The four heart chambers are called right atrium (RA), right ventricle (RV), left atrium (LA), and left ventricle (LV). The tricuspid valve and the pulmonary valve are the inlet and outlet valves of the RV, respectively. The mitral valve and the aortic valve are the inlet and outlet valves of the LV, respectively. The vessels connected with the right side of the heart are the systemic veins consisting of the superior vena cava and the inferior vena cava, as well as the pulmonary artery. The vessels connected with the left side of the heart are the pulmonary veins and the aorta.

The main purpose of the microcirculation is the transfer of oxygen, carbon dioxide, and nutrients between the blood and the surrounding tissue. This transfer occurs in the capillaries. In addition, the arterioles upstream of the capillaries have the ability to change their diameter and thereby the resistance to the flow, which is used for a local perfusion control. The venous systems lead the blood from the microcirculation back to the heart. The systemic venous system additionally acts as the main blood reservoir and contains over 60% of the total blood volume. The high compliance of the systemic veins has the effect that the inflow and the outflow of the veins

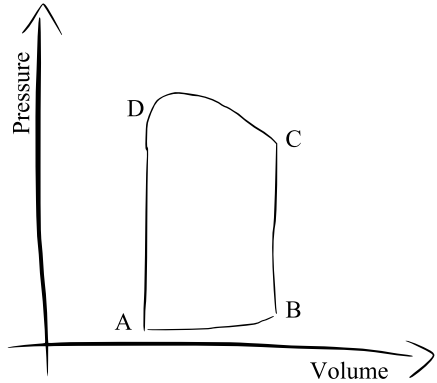

Figure 1.3: Pressure-volume (PV) diagram of the LV. For each cardiac cycle, the PV relationship of the LV is shown as a counterclockwise loop with the time as the implicit curve parameter. Point A denotes the end of relaxation and the start of filling. Point B denotes the end of filling and the start of contraction. Point C denotes the start of ejection. Point D denotes the end of ejection and the start of relaxation. The area inside the loop corresponds to the hydraulic work delivered by the ventricle.

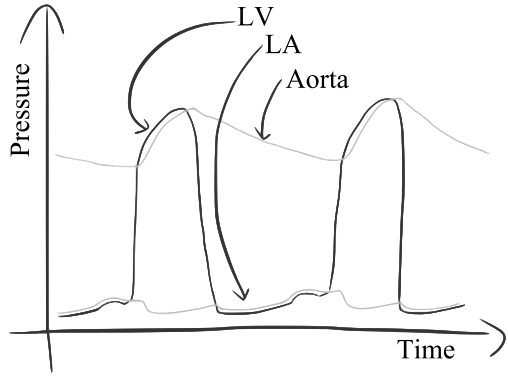

Figure 1.4: Time course of the pressures in the LV, the LA, and the aorta for two consecutive heartbeats. The LV pumps blood from the LA into the aorta. When the LV pressure is higher than the LA pressure, blood flows into the LV. When the LV pressure is between the LA pressure and the aortic pressure, both valves remain closed. When the LV pressure is higher than the aortic pressure, blood flows out of the LV.

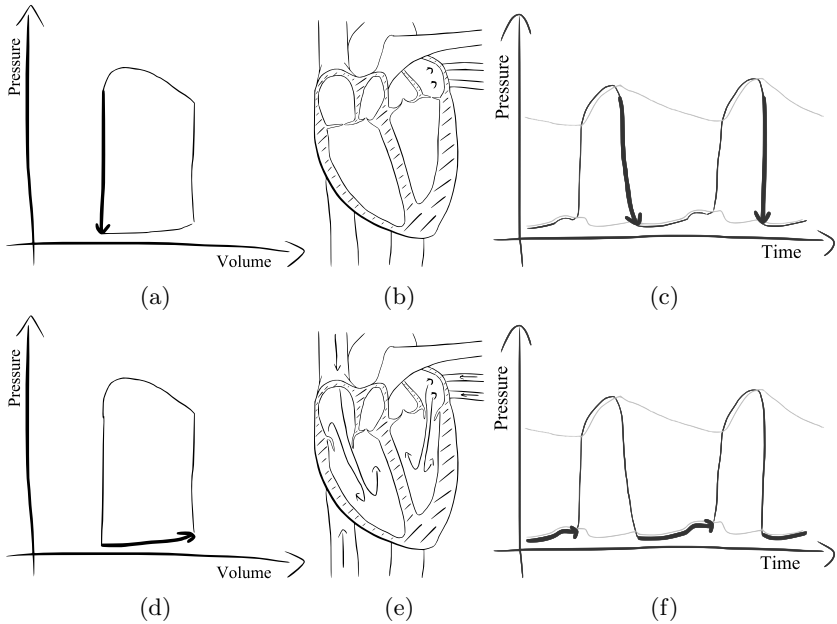

Figure 1.5: The diastole of the heart depicted with the PV diagram of the LV, a sketch of the heart, and the time course of the pressures. Panels (a), (b), and (c) depict the isovolumic relaxation phase after the end of ejection. In this phase, the pressure in the LV quickly drops from the systolic to the diastolic level. The valves remain closed. Panels (d), (e), and (f) depict the filling phase. In this phase, blood enters the LV through the LA and the mitral valve.

are not strongly coupled in the short term. With the ability to change their compliance, the systemic veins regulate the amount of blood flowing to the RA, which is the major control mechanism for the total blood flow through the circulation as described in Section 1.1.2. The term cardiac output (CO) denotes this total blood flow and is approximately 5 $^{\mathrm{L}}/_{\mathrm{min}}$ for a healthy adult person at rest.

1.1.2 Regulation of the blood flow

The heart is the driver for the blood flow in the circulation. However, due to the complex interaction of the heart and the circulation, the heart itself is not the ultimate factor that determines the amount of blood flow.

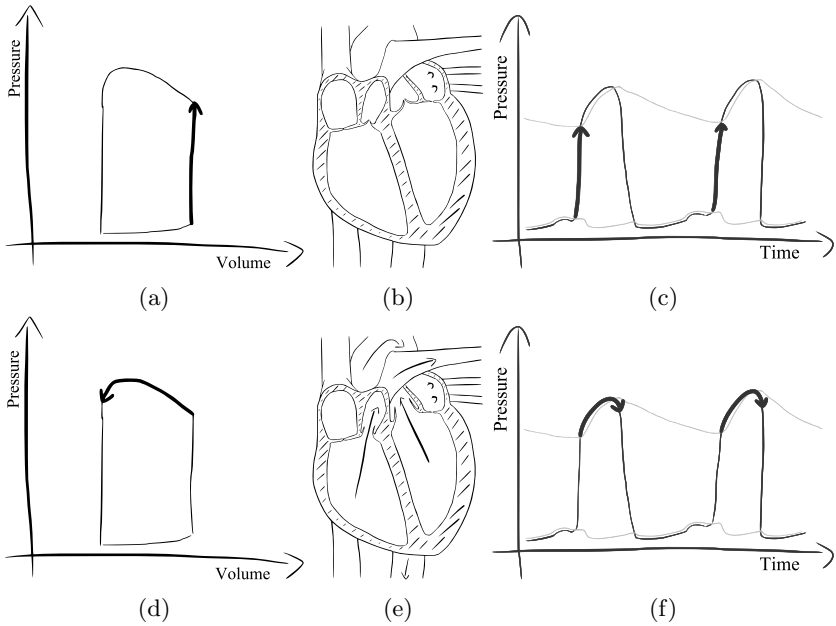

Figure 1.6: The systole of the heart depicted with the PV diagram of the LV, a sketch of the heart, and the time course of the pressures. Panels (a), (b), and (c) depict the isovolumic contraction phase after the end of filling. In this phase, the muscle contracts and the LV pressure rises until it exceeds the pressure in the aorta. Panels (d), (e), and (f) depict the ejection phase, where blood flows from the LV through the aortic valve into the aorta.

Four inputs determine the CO of each ventricle: preload, afterload, heart rate (HR), and contractility. The preload is the pressure upstream of the ventricle; the afterload is the pressure downstream of the ventricle. These two inputs are determined by the interaction of the circulation and the heart. The contractility describes the strength of the cardiac contraction. The HR describes the repetition frequency of the cardiac cycle.
The influence of these four inputs was described more than 100 years ago by the Frank-Starling law of the heart [3]. Figure 1.7 shows a graphical representation of the Frank-Starling law. This figure shows how the stroke volume, i.e., the amount of blood ejected per heartbeat, depends on preload, afterload, and contractility. The CO can be calculated by multiplying the stroke volume with the HR. In [4], the preload recruitable stroke

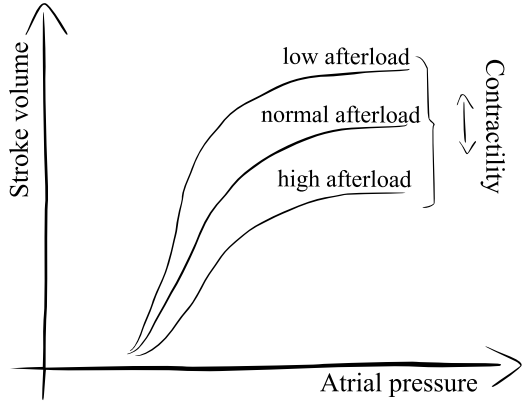

Figure 1.7: Graphical representation of the Frank-Starling law, which shows how the output of the heart (stroke volume) depends on preload, afterload, and contractility.

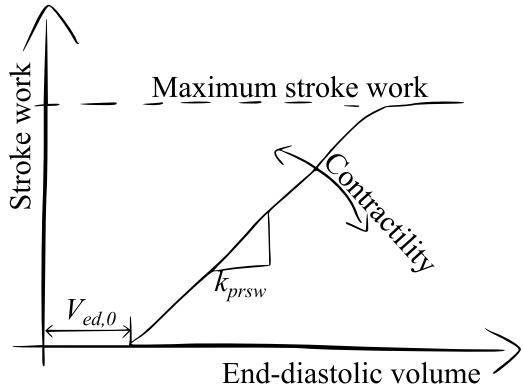

Figure 1.8: Graphical representation of the preload recruitable stroke work (PRSW), which is a linear, afterload-independent model of the Frank-Starling law. The model is completely defined by the slope k_{prsw}, the x-axis intercept $V_{\mathrm{ed},0}$, and the maximum stroke work. The slope k_{prsw} is defined by the contractility of the ventricle.

work (PRSW) is introduced as a linear, afterload-independent model of the Frank-Starling law. Figure 1.8 shows a graphical representation of the PRSW.

The sensitivity of the CO to the four inputs can be investigated with the Frank-Starling law. However, such an investigation neglects the interaction between the heart and the circulation. In the complete cardiovascular system, the CO is determined by the venous return, i.e., by the blood flow of the veins to the heart [1]. When the CO deviates from the venous return, the mismatch of in- and outflow to and from the atrium causes a change in preload until the CO matches the venous return again. Compared to the venous return, the CO is much more sensitive to the preload, i.e., a change in preload has a stronger influence on the CO than on the venous return. Therefore, the CO may be said to be determined by venous return. In engineering terms, the afterload can be viewed as a disturbance to this system. The HR and the contractility only play an important role during exercise when the preload sensitivity of the ventricle reaches its upper limit.

1.2 Heart failure

Heart failure describes the condition of the heart not being able to provide a sufficient blood flow to perfuse the body of a patient. Heart failure is a major clinical and public health problem [5]. More than 23 million people suffer from heart failure worldwide, and a vast majority of these patients is older than 65 years [6]. The main cause for heart failure are high blood pressure and ischemic cardiomyopathy, but also diabetes plays an increasingly important role [7]. Heart failure patients suffer from a continuous deterioration of their condition until death. The five-year mortality is 45-60% [6].

1.2.1 Treatment of end-stage heart failure

The treatment of heart failure depends on the status of the disease [8]. The ultimate options for the treatment of end-stage heart failure are heart transplantation and long-term mechanical circulatory support (MCS). Heart transplantation remains the gold standard for the treatment of end-stage heart failure, but a shortage of donor hearts strongly limits the number of transplantations [9]. This limitation of heart transplantation has been promoting the use of MCS devices in the last decade.
Originally, MCS was intended to bridge the time to transplantation [10], i.e., the MCS device is implanted to keep the patient alive until a donor

heart is available. However, the shortage of donor organs often prevents a later transplantation. Therefore, the focus of MCS has shifted toward destination therapy and bridge to recovery. Destination therapy denotes the use of an MCS device as a permanent implant, while bridge to recovery denotes the use of an MCS device to promote a functional recovery of the native heart. Whereas destination therapy has become standard clinical practice [11], bridge to recovery is still a field of basic research [12].

1.3 Ventricular assist devices

Mechanical circulatory support devices can be subdivided with regard to several properties [13]: cardiac assist versus cardiac replacement, univentricular versus biventricular support, and partial versus full support. When the native heart of a patient is explanted and completely replaced by two mechanical pumps, the device used is called a total artificial heart (TAH). The native heart is explanted to create space for the implantation of the TAH. A VAD is a single pump, which is implanted to pump from the LV to the aorta or from the RV to the pulmonary artery, i.e., the native heart is not explanted. The VAD can completely take over the pumping function of one ventricle, however, the native ventricle is normally still pumping. Most commonly, only the LV is failing and only a left VAD is implanted (univentricular support). When both the LV and the RV are failing, two VADs can be implanted (biventricular support). Partial assist devices are smaller pumps that can only assume a part of the pumping function of the ventricle. These devices generally are implanted at an early stage of heart failure in order to stop the progress of the disease. Partial assist devices are smaller, less invasive, and can be implanted without performing a thoracotomy. Since at the time of this writing, a vast majority of the implanted MCS devices are left VADs [11], the present thesis is focused on these devices.

VADs can be subdivided into three generations of pump types [10]. First generation VADs are pulsatile volumetric displacement pumps. These VADs consist of a pumping chamber and two unidirectional-flow valves. The pumping chamber is rhythmically inflated and deflated and thereby moves the blood against a pressure gradient. Second and third generation VADs are axial or centrifugal turbodynamic pumps in which a rotating impeller exerts a pressure on the blood. Second generation VADs are

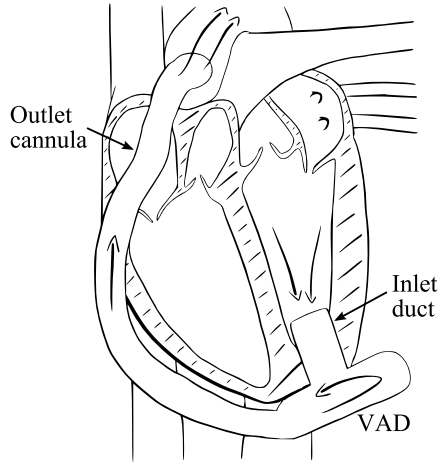

Figure 1.9: A turbodynamic VAD implanted between the LV and the aorta.

supported by classical contact bearings, while third generation VADs are supported by contactless bearings. Figure 1.9 shows the human heart with a turbodynamic VAD implanted between the LV and the ascending aorta.

1.3.1 Deltastream DP2

All experiments presented in the current thesis were conducted with a Deltastream DP2 (Medos Medizintechnik AG, Stolberg, Germany) non-implantable blood pump. This pump is different from a VAD with respect to several aspects such as size, durability, and hemolysis levels. However, for the in vitro experiments conducted during the research for the current thesis, only the hydraulic performance is relevant, which qualitatively is the same for any turbodynamic pump. The results presented in the current thesis can be obtained with any other blood pump or VAD, as long as the required pressure head (H) or pump flow (Q) do not exceed its operating range. Figure 1.10 shows the measured pressure head - pump flow (HQ) diagram of the DP2 pump. In order to implement our own physiological controller, the pump was modified such that the pump speed could be controlled as desired.

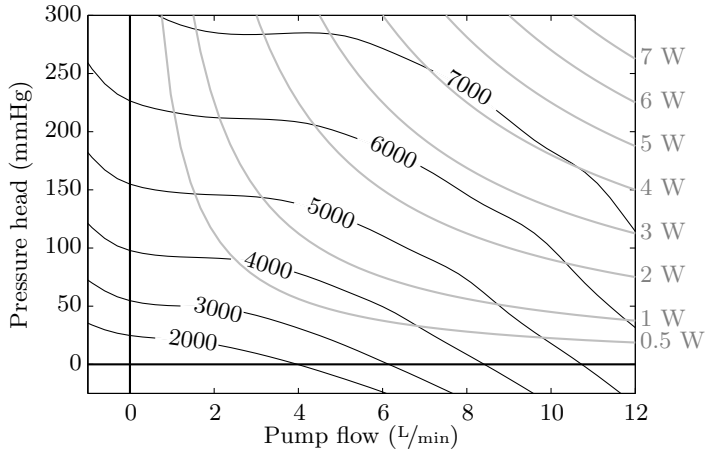

Figure 1.10: HQ diagram of the Deltastream DP2 blood pump. Each point in this diagram represents a stationary operating point of the pump defined by the pump speed, the pressure head, and the pump flow. The pump speed is denoted in revolutions per minute (rpm). The gray lines depict the hydraulic power at each operating point. This diagram is based on static measurements conducted on the hybrid mock circulation.

1.4 Physiological control of VADs

Pulsatile VADs are mostly operated at a constant pump rate and with constant pneumatic inflation and deflation pressures. The PVAD (Thoratec Corporation, Pleasanton, CA, USA) offers a full-to-empty mode in which the ejection is started immediately after the pump is completely filled [14]. Thereby, the pump rate adapts to the preload. Aside from this mode, pulsatile VADs are more sensitive to the pressure upstream than to the pressure downstream of the pump and thereby show an intrinsic physiological adaptation. Therefore, pulsatile VADs are mainly used for biventricular support, which requires a flow balance between the left and the right VAD.

Some turbodynamic VADs feature periodic speed variations for pump washout or can intermediately reduce the pump speed when suction is detected. Aside from that, clinically used VADs are typically operated at a constant speed. However, the flow through a VAD is not constant but to some extent depends on the pressure head, which pulsates during the cardiac cycle and which changes when the preload or the afterload of the LV change. Under exercise conditions, when the preload increases and the afterload decreases, the VAD flow increases as well. However, compared to the physiological circulation, this adaptation is strongly attenuated [15]. The physiological control of VADs aims at actively changing the pump speed of a VAD in order to achieve a true adaptation of the pump flow to the individual requirement of the patient.

In addition to the physiological adaptation, the active control of the pump speed may enhance the safety of the VAD patient. The limits for a safe operation of a VAD are called over- and underpumping. Figure 1.11 shows the effects of over- and underpumping. These limits depend on the state of circulation and are not constant. Therefore, keeping the pump speed constant can still lead to a violation of these limits. Underpumping means that the pump speed is too low, which can lead to a stagnation of the flow or even a regurgitation. Stagnation presumably increases hemolysis and the risk for thrombi [16]. In addition, underpumping may lead to an underperfusion of the patient. Overpumping means that the pump speed is too high, which leads to an emptying of the LV and consequently to a collapse of the ventricular walls [17]. This phenomenon is called suction or ventricular suction. It can intermediately block the flow through the pump

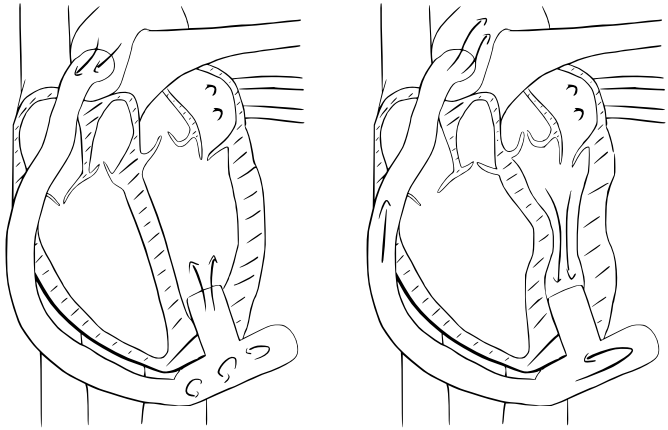

(a) Underpumping (b) Overpumping

Figure 1.11: The limits for physiological VAD control are over- and underpumping. Underpumping means that the pump speed is too low, such that the blood stagnates or flows backwards. Presumably, stagnation increases hemolysis and the risk for thrombi. Overpumping means that the pump speed is too high, which leads to an emptying of the LV and to a collapse of the ventricular walls. Additionally, the shifted septum may lead to an insufficiency of the tricuspid valve.

and can damage the myocardium. Overpumping can have negative effects even before suction occurs: A permanent closure of the aortic valve, which happens at high levels of support, may damage the valve. Additionally, a shifted septum may lead to a tricuspid valve insufficiency.
The task of physiological VAD control can therefore be summarized as follows: Adapt the pump speed of the VAD to meet the patient's perfusion requirement while avoiding the limits of over- and underpumping.

1.5 Scientific contribution

This thesis describes two major innovations for the physiological control of VADs, namely the hybrid mock circulation and the PRS controller.
The hybrid mock circulation is a test bench for blood pumps which combines a numerical model of the human cardiovascular system with a real hydraulic blood pump. Whereas the concept of combining numerical and

hydraulic parts has been proposed earlier [18, 19, 20], to the best knowledge of the author, this mock circulation represents the fist successful implementation of the concept. The core contributions are the proper definition of the interface signals that must be transferred between the numerical and the hydraulic part and the successful implementation of a fast pressure control system using pneumatics [21]. This fast control system enables the implementation of ventricular suction [22], which is an important feature that is typically not implemented in mock circulations. The hybrid mock circulation shows an unmatched physiological behavior and, due to the numerical implementation of the cardiovascular system, is very flexible.

[21] G. Ochsner, R. Amacher, A. Amstutz, A. Plass, M. Schmid Daners, H. Tevaearai, S. Vandenberghe, M. J. Wilhelm, and L. Guzzella, "A novel interface for hybrid mock circulations to evaluate ventricular assist devices," *IEEE Trans. Biomed. Eng.*, vol. 60, pp. 507–516, 2013

[22] G. Ochsner, R. Amacher, and M. Schmid Daners, "Emulation of ventricular suction in a hybrid mock circulation," in *Proc. of the 12th European Control Conference, 2013*, 2013, pp. 3108–3112

The PRS controller is a physiological control algorithm for VADs and is based on a measurement of the LV volume [23]. Most physiological VAD controllers presented in the literature are somehow inspired by the Frank-Starling law of the heart, i.e., they adapt the pump speed based on a measurement or estimation of the preload. The PRS controller works similarly, as it imitates the PRSW, which is a quantitative, afterload-independent, linear model of the Frank-Starling law. The core contributions of the PRS controller are the concept of measuring the LV volume for VAD control and the definition of a control law that is very directly based on the human physiology while still representing a classical control element. Experiments conducted on the hybrid mock circulation test bench have shown that the PRS controller behaves very similarly to the native heart and is therefore a promising approach for physiological VAD control.

[23] G. Ochsner, R. Amacher, M. J. Wilhelm, S. Vandenberghe, H. Tevaearai, A. Plass, A. Amstutz, V. Falk, and M. Schmid Daners, "A

physiological controller for turbodynamic ventricular assist devices based on a measurement of the left ventricular volume," *Artif. Organs*, 2013

In addition to the contributions presented in the current thesis, I worked in close collaboration with my colleagues on the research about the speed modulation of turbodynamic VADs [24, 25, 26, 27]. Speed modulation describes the variation of the pump speed synchronized to the cardiac cycle. These publications represent a valuable contribution to the understanding of the interaction between a turbodynamic VAD and the pathological heart. The interested reader is referred to [28].

[24] R. Amacher, G. Ochsner, A. Ferreira, S. Vandenberghe, and M. Schmid Daners, "A robust reference signal generator for synchronized ventricular assist devices," *IEEE Trans. Biomed. Eng.*, vol. 60, no. 8, pp. 2174–2183, 2013

[25] R. Amacher, J. Asprion, G. Ochsner, H. Tevaearai, M. J. Wilhelm, A. Plass, A. Amstutz, S. Vandenberghe, and M. Schmid Daners, "Numerical optimal control of turbo dynamic ventricular assist devices," *Bioeng.*, vol. 1, pp. 22–46, 2014

[26] R. Amacher, G. Ochsner, and M. Schmid Daners, "Synchronized pulsatile speed control of turbodynamic left ventricular assist devices: Review and prospects," *Artif. Organs*, 2014

[27] S. E. Jahren, G. Ochsner, F. Shu, R. Amacher, J. F. Antaki, and S. Vandenberghe, "Analysis of pressure head-flow loops of pulsatile rotodynamic blood pumps," *Artif. Organs*, vol. 38, pp. 316–326, 2014

1.6 Outline

This thesis is structured in as follows: Part I describes the hybrid mock circulation, which is a setup for the in vitro testing of VADs. Chapter 2 describes the hybrid mock circulation in general [21], while Chapter 3 describes how the mock circulation is extended to emulate ventricular suction [22]. Part II describes the PRS controller, which is a physiological control algorithm for VADs. Chapter 4 describes the PRS controller in general and presents experimental results [23]. The experimental results provided

in Chapter 4 were conducted on the hybrid mock circulation described in Part I. Chapter 5 describes a stability analysis for the PRS controller. This chapter has not been published elsewhere. Finally, a conclusion and an outlook on the future research are described in Chapter 6.

Part I

Hybrid Mock Circulation

Chapter 2

Hybrid Mock Circulation

This chapter presents a novel mock circulation for the evaluation of VADs, which is based on a hardware-in-the-loop concept. A numerical model of the human blood circulation runs in real-time and computes instantaneous pressure, volume, and flow rate values. The VAD to be tested is connected to a numerical-hydraulic interface, which allows the interaction between the VAD and the numerical model of the circulation. The numerical-hydraulic interface consists of two pressure-controlled reservoirs, which apply the computed pressure values from the model to the VAD, and a flow probe to feed the resulting VAD flow rate back to the model. Experimental results are provided to show the proper interaction between a numerical model of the circulation and a mixed-flow blood pump.
The content of this chapter is completely taken from [21].

2.1 Introduction

Despite significant clinical and technical developments, heart failure remains one of the major health challenges in developed countries. In extreme situations of heart failure, the assistance of an MCS system is required. Several devices are available depending on their clinical indication. VADs represent the most important class of MCS systems and can be used as a "bridge to transplantation", "bridge to recovery", or as a "destination therapy" [10]. VADs are blood pumps implanted in parallel to the failing heart, i.e., they pump blood from the LV and/or RV or the LA and/or RA into the aorta and/or pulmonary artery, respectively. Depending on the flow they generate, VADs can be divided into two categories, namely pulsatile and continuous-flow VADs. A pulsatile VAD is a positive displacement pump similar to a physiologic ventricle: A blood chamber with

inlet and outlet unidirectional valves is rhythmically inflated and deflated. This inflation and deflation is caused by pressurized air or a piston actuator, and it moves the blood against a pressure gradient. A continuous-flow VAD is a turbodynamic pump with a spinning rotor exerting pressure on the blood, which displaces the blood against a pressure gradient. Despite its name, a continuous-flow VAD can generate a pulsatile flow as well. It can be generated actively, by a pulsing action of the rotational speed of the rotor, or passively, by experiencing a pulsing pressure gradient across the pump. The design of a continuous-flow VAD can be axial, centrifugal, or mixed-flow (diagonal).

Three different types of preclinical models are used for the evaluation and testing of VADs, namely numerical models, mock circulations, and animal models. Due to their various advantages and disadvantages (see Table 2.1), all three types of models are typically used for the development of MCS devices. This thesis focuses on mock circulations. Conventional mock circulation models are widely used, featuring various levels of complexity, physiological behavior, and development costs [29, 30, 31, 32, 33]. In the last decade, several research groups have started including numerical models in their mock circulations, which yielded semi-hybrid [34, 35, 36, 37, 38, 39, 40, 41] or full-hybrid [18, 19, 20] mock circulations. In the former type, certain aspects of the circulation are influenced or replaced by a numerical model, whereas in the latter type, the complete circulation is simulated using software. Because our research group intends to develop a physiological controller for VADs, we need a numerical model and a mock circulation as preliminary testing environments. We thus decided to develop a full-hybrid mock circulation, which can be used for purely numerical simulations and as a hydraulic mock circulation.

The main difficulty in developing such a full-hybrid mock circulation is the implementation of the numerical-hydraulic interface, which allows the interaction between the numerical model and the VAD. This interface requires sensors, actuators, and a control system with a high bandwidth. To our knowledge, such an interface has not been successfully implemented thus far. In [18], the concept has been proposed, but without any experimental results. The authors of [19] also presented a concept, which was implemented but only partially. The use of a piston actuator to control the pressure is promising, but the use of mechanical valves introduces undesirable hydraulic effects. As described in [20], gear pumps can be used

to control the flow at the interface. Because no feedback is implemented and the quality of the feed-forward control is not shown, it is not clear how well the measured flow rate tracks the reference signal, which is an essential aspect of a hybrid mock circulation.
The mock circulation presented here addresses these problems and introduces a novel interface between a numerical model and a VAD. This interface uses pressurized air as an actuator and is fast enough for reference tracking of physiological pressure values. It thereby enables the realization of the full-hybrid mock circulation.

Table 2.1: Advantages and disadvantages of different models for VAD testing

	Animal Model	**Mock Circulation**	**Numerical Model**
+	• Inherent physiological behavior • Close to clinical setting	• Wide range of complexity • Can be inexpensive (for simple setup) • High repeatability • High controllability • Features can be modeled without complete understanding (e.g. valve regurgitation)	• Wide range of complexity • Inexpensive (software) • Absolute repeatability • Absolute controllability • High flexibility and modularity (features can be added, parameters changed) • Interpretation of results easier • Can be transferred easily from lab to lab (can be developed based on literature only)
–	• Time consuming and expensive • Ethically problematic • Low repeatability • Low controllability (pathological case difficult to model) • Mammal-specific results	• Can be complex and expensive (when physiological) • Certain features are difficult to model (e.g. preload sensitivity of the ventricle) • Interpretation of results can be difficult • Undesired effects present (e.g. valve water hammer)	• Many physiological aspects are neglected (every feature needs to be programmed) • Certain features are difficult to model (e.g. turbulence, wave travel) • VAD hardware cannot be tested (only numerical model of VAD can be tested)

2.2 Materials and methods

2.2.1 Concept

The concept of the mock circulation system presented here is referred to as a hardware-in-the-loop system. The device to be tested is hardware; the environment with which the device interacts is simulated using software. Figure 2.1 depicts the structure of the mock circulation. It consists of three main parts: A numerical model of the human blood circulation, the VAD to be evaluated, and the numerical-hydraulic interface in-between. The task of the numerical circulation model (see Section 2.2.3) is to provide a physiological environment for the evaluation of the VAD. The blood pump used for the experiments in this chapter is a non-implantable mixed-flow blood pump (see Section 2.2.2). The task of the numerical-hydraulic interface is to allow the interaction between the numerical circulation model and the VAD. This interface was developed specifically for the mock circulation presented in this work.
The interaction between the numerical circulation model and the VAD requires a choice of appropriate interface signals, which are passed from the VAD to the model and vice versa. This choice is explained using the governing differential equation of a turbodynamic VAD: The change in the VAD flow rate is given by [42]

$$\frac{\mathrm{d}q_{\mathrm{vad}}(t)}{\mathrm{d}t} = \frac{1}{L}\Big(p_{\mathrm{us}}(t) - p_{\mathrm{ds}}(t) + k \cdot N(t)^2 - R_l \cdot q_{\mathrm{vad}}(t) - R_q \cdot q_{\mathrm{vad}}(t) \cdot |q_{\mathrm{vad}}(t)|\Big), \quad (2.1)$$

where $q_{\mathrm{vad}}(t)$ is the instantaneous flow rate, $p_{\mathrm{us}}(t)$ and $p_{\mathrm{ds}}(t)$ are the pressures up- and downstream of the VAD, and $N(t)$ is the pump speed. The parameters L, k, R_l, and R_q denote the inertance, the pump gain, the linear, and the quadratic resistance of the VAD, respectively. The terms on the right-hand side of (2.1) are causes effecting an acceleration or deceleration of the flow. The flow rate resulting from this acceleration and deceleration is therefore the effect. When this model of the VAD is simulated numerically, the pressures and the pump speed are inputs, while the resulting flow rate is the output. The same choice is made for the signals at the mock circulation. The pressures are the signals sent from

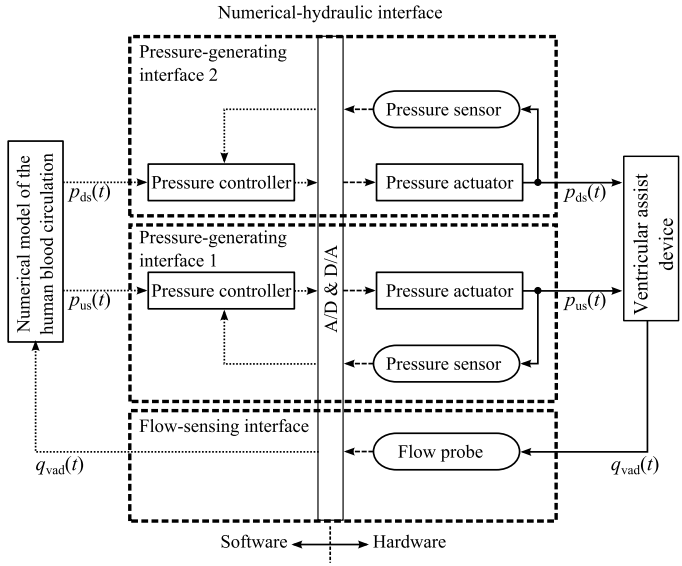

Figure 2.1: Structure of the mock circulation for the evaluation of a turbodynamic VAD. The solid lines denote physical quantities, the dashed lines denote electric signals, and the dotted lines denote digital signals, where $p_{\mathrm{us}}(t)$ is the pressure upstream of the VAD, $p_{\mathrm{ds}}(t)$ is the pressure downstream of the VAD, and $q_{\mathrm{vad}}(t)$ is the VAD flow rate. A/D & D/A denote the hardware responsible for the analog-to-digital and digital-to-analog conversion, respectively.

the numerical circulation model to the VAD, while the resulting flow rate through the VAD is fed back to the model. The numerical-hydraulic interface therefore consists of two pressure-generating interfaces (one for the pressure upstream and one for the pressure downstream of the VAD) and one flow-sensing interface.

2.2.2 Hardware

Figure 2.2(a) shows the setup of the mock circulation. The testing of a turbodynamic VAD requires two pressure-generating interfaces. The pressure-generating interface 1 (upstream) is connected to the inflow cannula, while the pressure-generating interface 2 (downstream) is connected to the outflow cannula of the VAD. The two interfaces are then connected via a backflow pump (Moyno 500 Pumps-200 Series, Moyno, Inc., Spring-

field, OH, USA), which yields a closed fluid circuit. The backflow pump is a progressive cavity pump, which is a positive displacement pump with very low flow pulsations. The pump is driven by a brushless DC-motor equipped with a 3.5:1 gearbox and a motor controller (EC45 / GP52C / DEC 70/10, Maxon Motor AG, Sachseln, Switzerland). This mock circulation setup requires three controllers, namely one fluid-level controller and two pressure controllers. The fluid level in the two pressure-generating interfaces is controlled using the backflow pump (see Section 2.2.3). The pressure in each pressure-generating interface is set to track the reference signal from the numerical circulation model (see Section 2.2.3). The flow-sensing interface is implemented by installing a flow probe (TS410 / ME-11PXL, Transonic Systems Inc., Ithaca, NY, USA) on the VAD cannula and providing the numerical circulation model with the sensor output.

Figure 2.2(b) shows a diagram of one pressure-generating interface developed for this mock circulation. The basic element of this interface is a sealed cylinder (height = 15 cm, $\varnothing = 15$ cm) made of polymethyl methacrylate (PMMA), which is filled to about 90% with the working fluid. The working fluid is a glycerine-water mixture with a volume ratio of 2:3,[1] which, at room temperature, has the viscosity of blood [42]. The cylinder has two fluid ports. One port is connected with the cannula of the VAD and the second port is connected with the backflow pump. The volume above the fluid acts as an air receiver. Since the fluid pressure is equal to the air pressure in the cylinder (plus the constant hydrostatic pressure), the air pressure is used to control the fluid pressure. The air pressure is controlled by the air mass in the cylinder, which can be changed by opening and closing the inlet and outlet valves, respectively. The proportional solenoid inlet valve (PVQ33-5G-23-01F, SMC Pneumatics, Tokyo, Japan) connects the receiver to the compressed air supply network, where a pressure of approximately 3 bar (absolute) prevails. The two proportional solenoid outlet valves (PVQ33-5G-40-01F, SMC Pneumatics, Tokyo, Japan) connect the receiver to a vacuum chamber, where a pressure of approximately 0.5 bar (absolute) prevails. The inlet valve has an opening of 2.3 mm and can be used up to a pressure difference of 3.5 bar, the outlet valves have an opening of 4.0 mm and can be used up to a pressure difference of 1.2 bar. This configuration of valves was chosen because the resulting maximum air-mass flow through the inlet valve is approximately

[1] One reservoir contains approx. 920 mL of glycerine and 1380 mL of water.

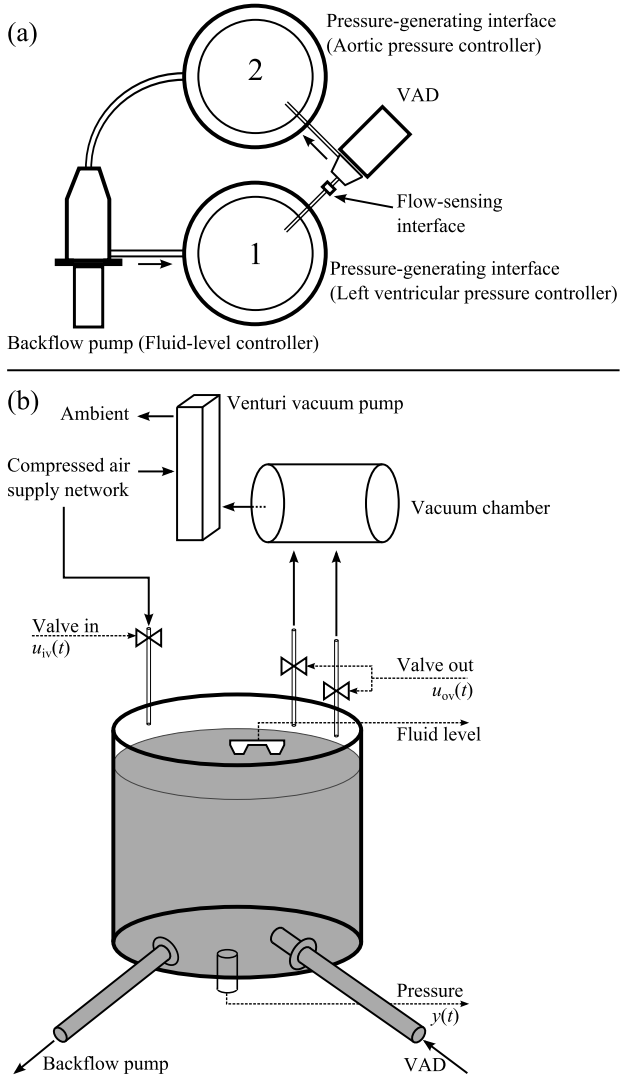

Figure 2.2: The mock circulation setup: (a) Top view of the complete setup to test a VAD; (b) Sketch of the pressure-generating interface 2. The solid lines denote physical quantities, the dashed lines denote electric signals. Pressure and fluid level are sensor outputs; valve in and valve out are actuator inputs.

equal to the maximum air-mass flow through the two outlet valves. The response time of the valves cannot be determined accurately in the current setting, but the delay between a change in the valve input and a change in the measured pressure is approximately 5 ms. The vacuum chamber is a cylinder made of PMMA with a volume of one liter, which is continuously evacuated by a venturi vacuum pump (ZL112-K15LOUT-E26L-Q, SMC Pneumatics, Tokyo, Japan). A pressure sensor (PN2009, IFM Electronic GmbH, Essen, Germany) continuously measures the pressure in the fluid. An infrared range finder (GP 2Y0D810Z0F, Sharp, Osaka, Japan) continuously measures the fluid level.
The blood pump included in the setup is the device to be evaluated. The experiments for this chapter were conducted using the Deltastream DP2 non-implantable mixed-flow blood pump with an inflow and an outflow cannula (length = 20 cm, $\varnothing_i = 12.7$ mm, $\varnothing_o = 17.5$ mm) made of Tygon R-3603. This pump was later equipped with an encoder (ME22, PWB Encoders GmbH, Eisenach, Germany) and an industrial motor controller (Accelus ASP-090-09, Copley Controls Corp., Canton, MA, USA). These modifications allowed the pump speed to be controlled as desired.[2]

2.2.3 Software

A personal computer (PC) running Windows XP included in the mock circulation setup is responsible for five tasks: Data acquisition, simulation of the numerical circulation model, control of the fluid level, reference tracking of the pressures, and control of the VAD. The PC is running MATLAB Real-Time Windows Target (The MathWorks, Inc., Natick, MA, USA), and is equipped with a data acquisition card (MF624 multifunction I/O card, Humusoft s.r.o., Prague, Czech Republic), which is responsible for the data input and output. The model is executed at 5 kHz, and the integrators are implemented with a fourth-order Runge-Kutta approximation. All sensor inputs are sampled at 5 kHz and logged at 1 kHz. All measured signals are post-processed by a low-pass filter with a cut-off frequency of 200 Hz. This filtering is done by taking the Fourier transform of the raw signal, removing all frequency content above 200 Hz, and taking the inverse Fourier transform.

[2] The blood pump speed controller is described in Section 3.2.1.

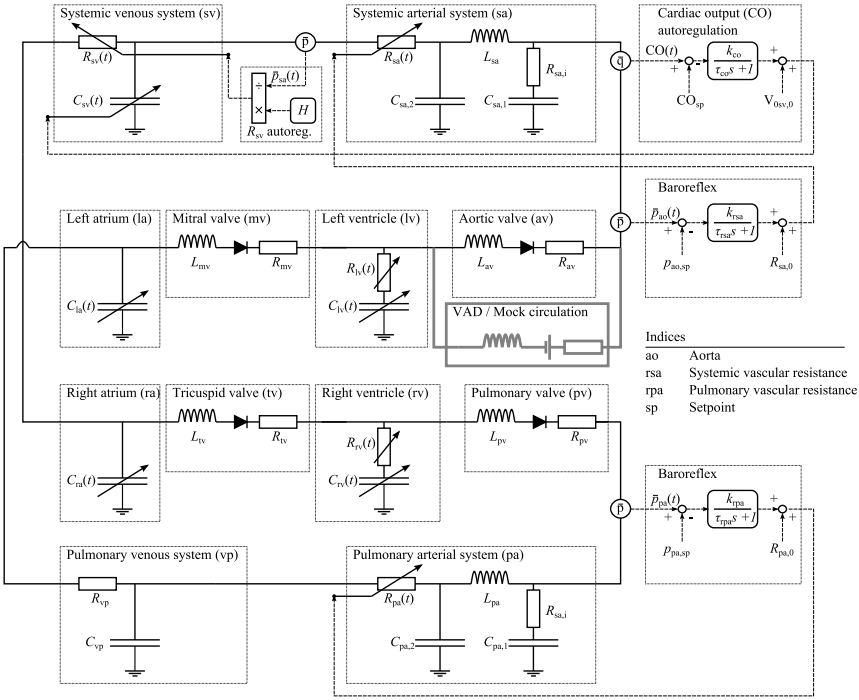

Figure 2.3: Electric analog of the numerical circulation model. The VAD / Mock circulation block is included in the figure to indicate where the interface is implemented; it is not included in the simulation. A description and validation of the model can be found in [43].

Numerical circulation model

The type and complexity of the numerical model, which is used to simulate the circulation, can be chosen almost arbitrarily. Two requirements have to be met when a numerical model is programmed for this application: First, because the model interacts with a real device, it must be executable in real-time. Second, because the numerical-hydraulic interfaces can only transmit lumped signals, the model must be able to provide and accept such signals. Based on these requirements, a lumped-parameter model is considered to be suited best for this application.

Figure 2.3 depicts the numerical model used for the experiment below. This model has been taken from [43], where it is described in detail.

The model includes a systemic and a pulmonary circulation. Five-element Windkessel models are used to simulate the arterial systems, whereas classic Windkessel models are used to simulate the venous systems. The pressure in both arterial systems is regulated by a baroreflex, which adapts the arterial resistance. A CO autoregulation adapts the unstressed volume of the systemic veins. The resistance of the systemic veins is adapted by an R_{sv} autoregulation. Both atria and both ventricles are contracting actively using a time-varying elastance model. A validation of this model in the physiological and pathological state is provided in [43].
The interface between the model and the mock circulation is implemented as follows: In every time-step of the simulation the computed pressures in the LV and in the aorta are transmitted from the model to the respective pressure controller, where they serve as the reference signal $r(t)$. Also in every time-step, the measured flow-rate value is transmitted from the VAD to the volume integrators of the model, where it is an inflow to the aorta and an outflow from the LV.

Fluid-level control

The task of the fluid-level controller $C_{\mathrm{fl}}(s)$ is to keep the fluid level in the pressure-generating interfaces constant by changing the speed of the backflow pump. The controller input is the deviation of the measured fluid level in the pressure-generating interface 2 (see Figure 2.2) from its reference value, while the controller output is the voltage sent to the backflow pump motor controller. The fluid volume in the pressure-generating interface has no influence on the VAD flow rate, only the pressure is relevant. The fluid-level control is implemented to prevent an overflow or a complete drainage of the interfaces in spite of a net flow through the VAD, which is the disturbance for this control system. Because the reference value for this controller is constant and only the mean disturbance flow rate needs to be compensated, the fluid-level control task is not very challenging. A proportional-integral (PI) controller with roll-off and anti-reset windup is implemented for this task [44]. The transfer function of this controller is given by

$$C_{\mathrm{fl}}(s) = k_{\mathrm{fl}} \cdot \left(1 + \frac{1}{T_{\mathrm{fl}} \cdot s}\right) \cdot \frac{1}{\tau_{\mathrm{fl}} \cdot s + 1}, \tag{2.2}$$

where $k_{\mathrm{fl}} = 833.3\,\mathrm{V/m}$ is the proportional gain, $T_{\mathrm{fl}} = 2\,\mathrm{s}$ is the integrator time constant, $\tau_{\mathrm{fl}} = 0.25\,\mathrm{s}$ is the roll-off time constant, and s is the Laplace

variable. The parameters of the controller were tuned manually until the control error during the experiment was minimal and no speed oscillation could be heard.

Pressure reference tracking

For the proposed concept to work as desired, the pressure in the pressure-generating interfaces must track the reference signals from the numerical circulation model. This is the task of the two pressure controllers $C_p(s)$. Each pressure-generating interface is controlled independently, but the two controllers are structurally identical. The controller input is the respective deviation of the measured pressure $y(t)$ from its reference signal $r(t)$, while the controller output $u(t)$ is the normalized current sent to the respective inlet and outlet proportional valves.
The first step of the controller derivation is the definition of the specifications it must fulfill. Three specifications are defined for the pressure controller: Zero steady-state error, a small step-response overshoot, and a sufficiently high bandwidth. The required bandwidth is defined by analyzing the frequency content of the reference pressure trajectories which were generated by simulating the numerical circulation model. As a result of this analysis, the maximum frequencies are assumed to be 100 $^{\mathrm{rad}}/_{\mathrm{s}}$ (15.9 Hz) and 200 $^{\mathrm{rad}}/_{\mathrm{s}}$ (31.8 Hz) for the aortic and the left ventricular pressures, respectively. These values are noteworthy because they are more than one order of magnitude larger than the HR (1-2 Hz), and they differ by a factor of two. These results are important since they clearly state that a control system that has a bandwidth similar to the HR is not able to emulate physiological pressure trajectories.
The pressure controllers are derived by choosing a suitable control structure and finding the optimal parameters using a numerical optimization procedure. The control structure is chosen to be a PI controller with a lead extension. The transfer function of this controller is given by

$$C_p(s) = k_p \cdot \left(1 + \frac{1}{T_i \cdot s}\right) \cdot \left(\frac{T_l \cdot s + 1}{\alpha \cdot T_l \cdot s + 1}\right), \tag{2.3}$$

where k_p is the proportional gain, T_i is the integrator time constant, T_l is the lead time constant, and α^{-1} is the lead magnitude gain. The numerical optimization procedure is used to find the optimal parameters by minimiz-

ing the deviation of the magnitude of the complementary sensitivity $T(s)$ from the magnitude of a desired complementary sensitivity $T_{\text{des}}(s)$ in the frequency range of two decades around the desired bandwidth:

$$\min_{k_p,T_i,T_l,\alpha} \int_{10^1}^{10^3} \left(|T_{\text{des}}(\omega)| - |T(\omega)|\right)^2 \mathrm{d}\omega. \tag{2.4}$$

The complementary sensitivity is defined as [44]

$$T(s) = \frac{Y(s)}{R(s)} = \frac{C_p(s) \cdot P(s)}{1 + C_p(s) \cdot P(s)}, \tag{2.5}$$

where $P(s)$ is the transfer function of the plant, $Y(s)$ is the Laplace transform of the measured pressure signal $y(t)$, and $R(s)$ is the Laplace transform of the reference pressure signal $r(t)$. The complementary sensitivity is the transfer function from the reference input $r(t)$ to the plant output $y(t)$, i.e., it describes the reference tracking behavior of the closed-loop system. The desired complementary sensitivity $T_{\text{des}}(s)$ is chosen to be a second-order system:

$$T_{\text{des}}(s) = \frac{k_{\text{des}}}{\left(\tau_{\text{des}}^2 \cdot s^2 + 2 \cdot \tau_{\text{des}} \cdot \delta_{\text{des}} \cdot s + 1\right)}, \tag{2.6}$$

where k_{des} is the desired steady-state gain, τ_{des} is the desired time constant and δ_{des} is the desired damping. A simplex algorithm (fminsearch) in MATLAB is used to minimize the objective function. This function takes the parameters k_p, T_i, T_l, and α as inputs and returns a quality measure for the parameters: First, according to (2.3), (2.5), and (2.6), it calculates $T(s)$ and $T_{\text{des}}(s)$ as continuous-time transfer functions. The calculation of (2.5) requires a linear model of the plant $P(s)$, which is described in Appendix A at the end of this chapter. Second, it calculates the magnitude of both transfer functions $T(s)$ and $T_{\text{des}}(s)$ at 200 discrete, logarithmically spaced frequencies. Finally, the sum of the squared differences is calculated to approximate (2.4), which yields the quality measure to be minimized. The parameters for $T_{\text{des}}(s)$ are chosen such that the previously defined specifications are met: The steady-state gain k_{des} is chosen equal to one to ensure that no steady-state error occurs. The step-response overshoot is determined by the damping δ_{des}. By choosing a damping larger than 0.5 the resulting step-response overshoot is less than 20% [44]. The bandwidth

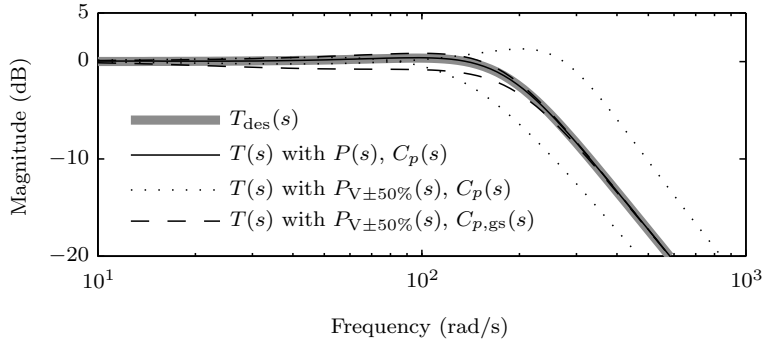

Figure 2.4: Magnitude of the complementary sensitivity $T(s)$ of the control system for the left ventricular pressure. The solid line denotes the nominal transfer function. The dotted lines denote $T(s)$ when the receiver volume is changed by $\pm 50\%$ and the nominal controller is used. The dashed lines denote $T(s)$ when the receiver volume is changed by $\pm 50\%$ and the controller is gain-scheduled.

is determined by the damping and the time constant. For the left ventricular pressure controller they are chosen to be $\tau_{\text{des}} = 0.0055\,\text{s}$ and $\delta_{\text{des}} = 0.55$, respectively. For the aortic pressure controller they are chosen to be $\tau_{\text{des}} = 0.006\,\text{s}$ and $\delta_{\text{des}} = 0.75$, respectively. The optimization procedure is run separately for each controller. Figure 2.4 shows the complementary sensitivity $T(s)$ for the left ventricular pressure controller. Table 2.2 lists the optimal parameters for both pressure controllers as found by the optimization procedure.

Table 2.2: Pressure Controller Parameters

LV		**Aorta**	
Parameter	**Value**	**Parameter**	**Value**
k_p	$7.620 \cdot 10^{-6}\,\text{Pa}^{-1}$	k_p	$6.340 \cdot 10^{-6}\,\text{Pa}^{-1}$
Ti	$0.0237\,\text{s}$	Ti	$0.0234\,\text{s}$
T_l	$0.0624\,\text{s}$	T_l	$0.0631\,\text{s}$
α	0.0723	α	0.0840

For the implementation, the controller is extended with anti-reset windup [44] and gain-scheduling [45]. Figure 2.5 shows the resulting control struc-

ture. Anti-reset windup is normally implemented in a PI controller with output saturation[3] to counteract the occurrence of an overfull integrator (reset windup): Since the controller output is already at its maximum or minimum, when the output of the controller goes into saturation, the integrator continues to integrate the error $e(t)$ without contributing to its reduction. When, after a certain time in saturation, the error changes its sign, the overfull integrator prevents the system from reacting as desired, since the integrator needs to be emptied first. In order to prevent this situation of an overfull integrator, anti-reset windup empties the integrator while the controller output is in saturation. The anti-reset windup gain is chosen to be $k_{\mathrm{arw}} = 3\,\mathrm{s}^{-1}$.

Gain-scheduling is implemented to adapt the controller gain to the fluid level. The dynamics of the plant depend approximately linearly on the receiver volume, which is determined by the fluid level. The nominal plant $P(s)$, which is used for the derivation of the nominal controller $C_p(s)$, is derived with a receiver volume of $V_0 = 0.2\,\mathrm{l}$. To analyze the influence of the receiver volume on the dynamics, the plant is linearized at different receiver volumes ($V_{+50\%} = 0.3\,\mathrm{l}$ and $V_{-50\%} = 0.1\,\mathrm{l}$), which yields the two models $P_{\mathrm{V}\pm 50\%}(s)$. The dotted lines in Figure 2.4 show how $T(s)$ changes when $P_{\mathrm{V}\pm 50\%}(s)$ and the nominal controller $C_p(s)$ are used for its calculation. In order to cope with the changing plant dynamics, the controller gain is implemented as a linear function of the measured receiver volume $k_{p,\mathrm{gs}}(t) = (k_p/V_0) \cdot V(t)$. The dashed lines in Figure 2.4 show how $T(s)$ changes when it is calculated with $P_{\mathrm{V}\pm 50\%}(s)$ and the gain-scheduled controller $C_{p,\mathrm{gs}}(s)$. The variations in $T(s)$ are clearly reduced with the gain-scheduled controller compared to the nominal one. Gain-scheduling is allowed in this context since, as shown in Appendix A at the end of this chapter, the fluid-level dynamics are much slower than the air-pressure dynamics.

The controller output $u(t)$ is added to a nominal inlet valve output $u_{\mathrm{iv},0}$ and subtracted from a nominal outlet valve output $u_{\mathrm{ov},0}$ to calculate the values applied to the valves. An increasing value of $u(t)$ therefore opens the inlet valve and closes the outlet valves at the same time. The nominal valve outputs are chosen such that a small air-mass flow exists through the

[3] The normalized current signal sent to the valves can only take values between 0 and 1.

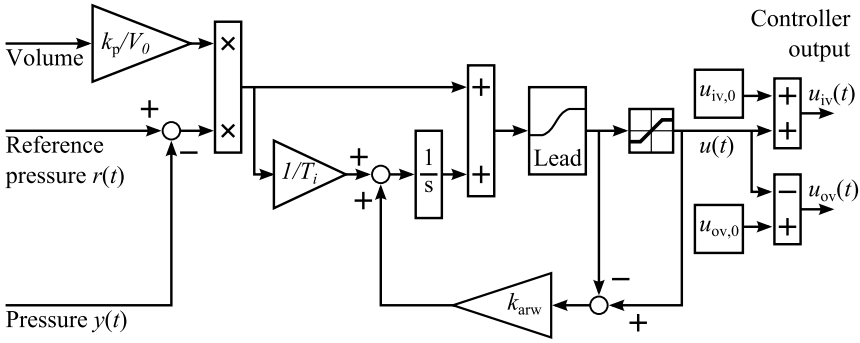

Figure 2.5: Control structure of the implemented pressure controller.

valves ($u_{iv,0} = 0.5467$, $u_{ov,0} = 0.5214$). This configuration yields a very fast valve response time.

2.2.4 Experiment

The goal of the experiment shown here is the analysis of the controller performances and the verification of the proposed mock circulation concept. The numerical circulation model is set to a pathological state by reducing the contractility of the LV to 34% of its physiological value and by setting the HR to 90 bpm [43]. Before the start of the experiment, the numerical circulation model is run offline to obtain a baseline "measurement" without pump support. For the experiment, the blood pump is installed between the LV and the aorta. At the beginning of the experiment, the pump is set to a constant speed of 3500 rpm and the system is run until steady-state is reached. Then the pump speed is ramped up to 4800 rpm within 1 s where it is held constant again until steady-state is reached. This procedure allows a fair comparison of the state of the system at baseline (no pump), at a low support level (3500 rpm), and at a high support level (4800 rpm). The figures in Section 2.3 show a 20 s excerpt from this experiment starting 2 s before the speed ramp.

This experiment was chosen for three reasons: First, the high HR yields steep pressure transients and is therefore challenging for the pressure controllers. Second, the large increase of the pump speed causes a large variation of physiologic parameters including the reference pressures. And

third, the fast change of the pump speed emphasizes the necessity for a real-time interaction between model and pump.

The quality of the pressure reference tracking is analyzed by the time course of the pressure reference tracking error $e(t) = r(t) - y(t)$ and by the time course of the resulting flow rate error. For the flow rate error analysis, a numerical model of the blood pump is simulated once with the two reference pressures $r(t)$ as inputs and once with the two measured pressures $y(t)$ as inputs. Subtracting the two resulting flow rates yields an estimate of the flow rate error. The numerical model of the blood-pump used for these simulations is completely described by (2.1) with the parameters $L = 0.0388\,\mathrm{mmHg{\cdot}s^2/mL}$, $R_l = 0.0958\,\mathrm{mmHg{\cdot}s/mL}$, $R_q = 0.0042\,\mathrm{mmHg{\cdot}s^2/mL^2}$, and $k = 6.131 \cdot 10^{-6}\,\mathrm{mmHg/rpm^2}$. These parameters were identified using static and dynamic measurements at the mock circulation.

2.3 Results

Section 2.3.1 shows the measurement results of the experiment focused on the interaction between the numerical circulation model and the pump. Section 2.3.2 analyzes the quality of the fluid-level and pressure controllers.

2.3.1 Mock circulation

The panels in Figure 2.6 depict the measurement results of the experiment. Figure 2.6(a) shows the reference and the measured pump speed with the ramp from 3500 rpm to 4800 rpm between $t = 2\,\mathrm{s}$ and $t = 3\,\mathrm{s}$. The oscillations of the measured signal are caused by the pressure pulsations up- and downstream of the pump. Figure 2.6(b) shows the increase in the measured pump flow rate from 3.1 $^{\mathrm{L}}/_{\mathrm{min}}$ at the low support level to 5.7 $^{\mathrm{L}}/_{\mathrm{min}}$ at the high support level. The reduction of the pulsatility toward the end of the experiment is mainly caused by the smaller pressure pulsations in the LV. The CO increases from 3.5 $^{\mathrm{L}}/_{\mathrm{min}}$ without pump support to 4.2 $^{\mathrm{L}}/_{\mathrm{min}}$ at the low support level to 5.7 $^{\mathrm{L}}/_{\mathrm{min}}$ at the high support level. The aortic valve thus stays closed after the pump-speed ramp. Figure 2.6(c) shows the reference and the measured pressures in the LV and the aorta. The LV is emptied during the high support level, and the systolic pressure decreases from 104.7 mmHg at baseline and 105.7 mmHg at the low support level to 17.7 mmHg at the high support level. The mean aortic pressure increases from 81.2 mmHg at baseline to 90.8 mmHg at the low support level to 107.0 mmHg at the high support level. Figure 2.6(d) shows the PV diagram of the LV. The pressure signal for this plot is measured, whereas the volume signal is simulated. At the low support level, the PV loop looks similar to the baseline, while at the high support level the PV loop becomes bell shaped with a reduced stroke volume, a reduced end-diastolic volume (EDV), and a lower systolic pressure. The mean LA pressure is reduced from 21.5 mmHg at baseline to 15.1 mmHg at the low support level to 2.7 mmHg at the high support level.

2.3.2 Controller performance

Fluid-level controller

Figure 2.7 depicts the results of the experiment to analyze the quality of the fluid-level and the pressure controllers. It has been stated in Sec-

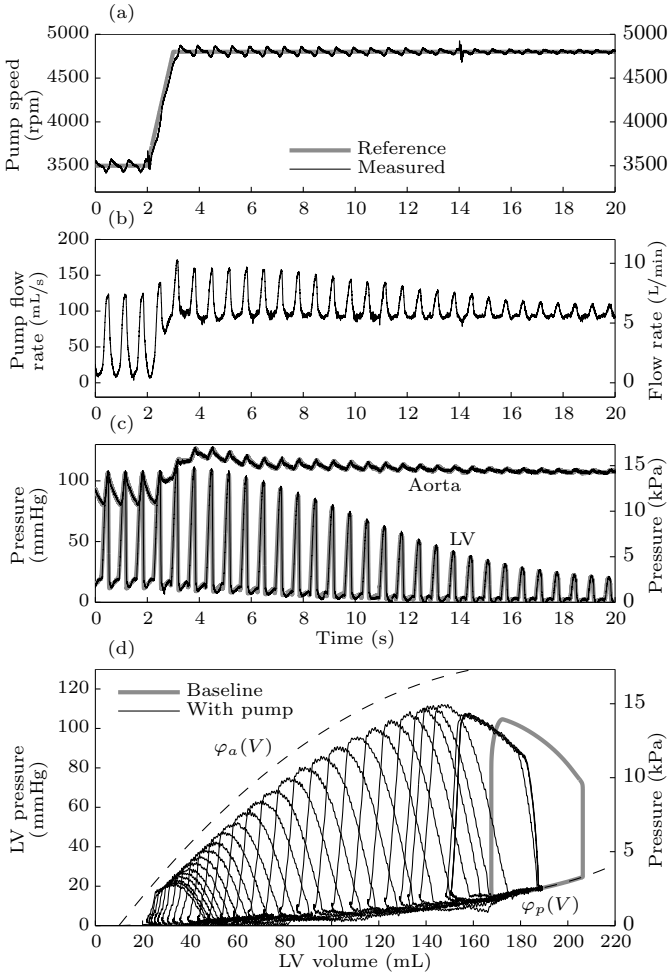

Figure 2.6: Measurement results of the experiment. The upper three panels depict the time course of (a) the pump speed, (b) the resulting flow rate through the pump, and (c) the pressures upstream and downstream of the pump. Panel (d) depicts the PV diagram for this experiment. The functions $\varphi_a(V)$ and $\varphi_p(V)$ denote the end-systolic pressure-volume relationship and the end-diastolic pressure-volume relationship, respectively.

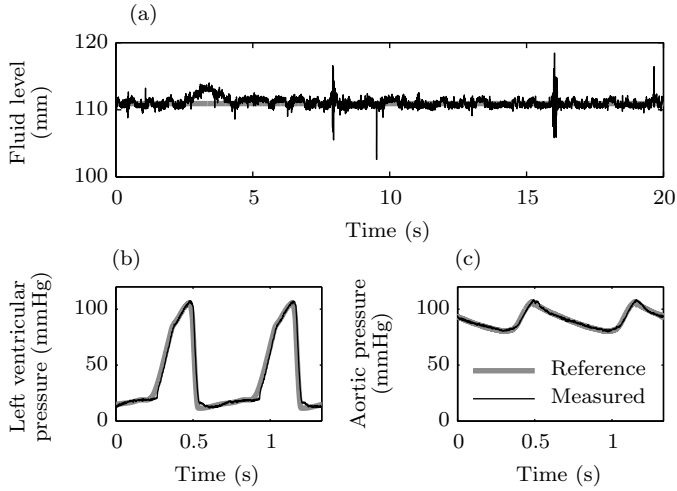

Figure 2.7: Measurement results to analyze the performance of the controllers. The fluid-level is shown for the complete experiment; the pressures are shown for the first two beats only. (a) Fluid-level controller, (b) left ventricular pressure controller, (c) aortic pressure controller.

tion 2.2.3 that in fact, the task of fluid-level control is not very challenging. Figure 2.7(a) shows that the deviation of the measured fluid level from the reference signal is less than 5 mm despite a rapid increase in the pump flow rate.

Pressure controller

In contrast, the pressure reference tracking is very challenging and is the key aspect of the mock circulation concept proposed here. Figures 2.7(b) – (c) show a detailed view of the reference tracking for the left ventricular and the aortic pressure controllers. Figures 2.8(a) – (b) show an analysis of the reference tracking error signal for the pressure controllers. Figure 2.8(a) shows the error signal $e(t) = r(t) - y(t)$ as measured during the experiment. The maximum error in the aortic pressure is smaller than 5 mmHg, whereas the maximum error in the left ventricular pressure is larger than 25 mmHg. This large error occurs during the steep transients and can be attributed to a phase shift between the two signals $r(t)$ and $y(t)$. The root-mean-square (RMS) errors for the aortic and the left ventricular pressure are

0.89 mmHg and 4.58 mmHg, respectively. Figure 2.8(b) shows the error signal for the same measurement when the reference signal is delayed by 10 ms, i.e., $e(t) = r(t + 0.01) - y(t)$. The maximum error in the aortic pressure decreases to less than 4 mmHg, and the maximum error in the left ventricular pressure decreases to less than 9 mmHg. The RMS error with the delayed reference signals is 0.95 mmHg and 1.79 mmHg, respectively. Figures 2.8(c) – (d) show the analysis of the flow rate error introduced by the pressure error as explained in Section 2.2.4. Figure 2.8(c) shows the flow rate error signal for the original pressure values, while 2.8(d) shows the flow rate error signal when the reference pressures are delayed by 10 ms. As for the pressure error, the bulk of the flow rate error can be attributed to a small phase shift between $r(t)$ and $y(t)$. When this delay is taken into account, the maximum flow rate error introduced by the pressure controllers decreases from more than 12 $^{\mathrm{mL}}/_{\mathrm{s}}$ to less than 5 $^{\mathrm{mL}}/_{\mathrm{s}}$. The RMS flow-rate error decreases from 3.79 $^{\mathrm{mL}}/_{\mathrm{s}}$ to 1.72 $^{\mathrm{mL}}/_{\mathrm{s}}$

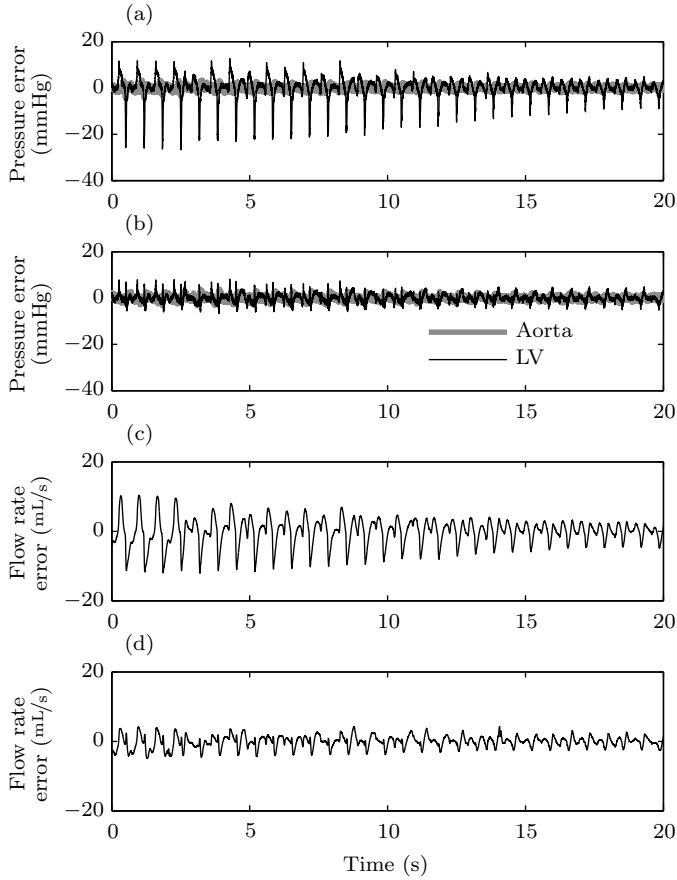

Figure 2.8: Analysis of the control error. (a) Pressure control error $e(t) = r(t) - y(t)$, (b) pressure control error with delayed reference signal $e(t) = r(t + 0.01) - y(t)$, (c) simulated flow rate error, (d) simulated flow rate error with delayed reference signals.

2.4 Discussion

Based on the references [46, 47, 48, 49] and according to the cardiac surgeons involved in our group (André Plass, Hendrik Tevaearai, Markus J. Wilhelm), the results observed with our system are in good agreement with those observed in patients assisted with a VAD in clinical routine. These results demonstrate that the proposed concept works as desired for the setup with a mixed-flow blood pump attached to the LV and the aorta. This concept combines the advantages of numerical models and classic mock circulations and should become an alternative method to animal experiments in the future.

As opposed to traditional mock circulations, our system offers more flexibility since all conditions and setups can be changed directly in the numerical model, i.e., without altering the circuit. Besides hemodynamic parameters, our system allows the introduction of anatomical physiological or pathological changes such as a valve regurgitation. Even the change from a ventriculo-aortic to an atrio-aortic cannulation can be made in the numerical model. Another advantage over the classic mock circulation is the full insight into the model. Every feature has been programmed, i.e., all phenomena can be attributed to a certain cause, which is often not possible in classic mock circulations. The improved insight also results from the possibility to log every signal of the circulation without installing any sensors. Last but not least, the development of such a model can be based on the literature, where models for many aspects of the circulation can be found. This knowledge is mostly well documented, is easy to find, and it significally reduces the effort to produce a good model.

The advantage of this concept over purely numerical models is the use of the real VAD instead of a VAD model. The real VAD can be tested with the real inputs and outputs that would be used clinically. For the development of flow or pressure observers [17], cardiac index observers [50], or control strategies [51], the implementation on a real device is a significant step from the purely numerical simulation.

Whereas the numerical circulation model already includes a baroreflex, a CO, and an R_{sv} autoregulation and seems well suited for this application, several features which are not yet included are expected to improve the validity of the results further. These features include an interaction between the LV and the RV, suction at the inflow cannula, valve regurgitation, and

the influence of the respiration on the circulation. Due to the flexibility of the full-hybrid mock circulation, it will be possible to gradually extend it by these features.

Section 2.3.2 shows the results for the fluid-level and pressure controllers. The results for the fluid-level controller show a good disturbance rejection also against fast disturbances from the blood pump. The results for the pressure controllers show a small phase shift between the reference signal $r(t)$ and the measured signal $y(t)$. This phase shift can be attributed on one hand to slight delays in the sensors and actuators and on the other hand to a phase of the controller. The maximum delay introduced by this phase shift is around 10 ms. At an HR of 90 bpm this delay corresponds to only 1.5% of the duration of the cardiac cycle and is therefore negligible. When this delay is taken into account, the estimation of the flow rate error results in an RMS error of 1.72 $^{\mathrm{mL}}/_{\mathrm{s}}$ and a maximum error of 5 $^{\mathrm{mL}}/_{\mathrm{s}}$. Compared to the measured maximum flow rate, the maximum error corresponds to 2.5%. Since this value is in the same range as the accuracy of the flow probes, a further improvement of the pressure controllers is not considered necessary.

The measurements show that a bandwidth of 200 $^{\mathrm{rad}}/_{\mathrm{s}}$ is sufficient for the left ventricular pressure controller at 90 bpm. In the current setup, the bandwidth of the pressure controllers cannot be increased significantly without sacrificing their robust behavior. If the frequency content of the reference pressures were even higher (e.g. due to ventricular suction), the quality of the reference tracking no longer could be ensured. The critical hardware components are the valves and the pressure sensors. The valves must be fast, and the noise introduced by the sensors must be very small in order to avoid any additional phase from low-pass filtering.

Thus far, only the configuration with a turbodynamic blood pump has been verified. If a different type of MCS device needs to be evaluated, the mock circulation setup can be adapted. For instance, a pulsatile VAD requires a second flow-sensing interface because in- and outflow rates are not identical. Aside from this change in the setup, the ability of the controllers to cope with the different flow of a pulsatile VAD will have to be verified, which is a goal we have set for the near future.

2.5 Conclusion

It has been demonstrated that the novel interface presented in this chapter enables the realization of the concept of the full-hybrid mock circulation that is superior to the conventional mock circulation. It represents a useful tool for researchers involved in the design and development of MCS devices.

Appendix A

This section describes the derivation of the linear model of the plant $P(s)$, which is used for the pressure controller synthesis. The basis for this linear model is a detailed nonlinear grey-box model of the complete mock circulation. This nonlinear model contains submodels describing both fluid reservoirs, both air pressure receivers, the blood pump, the backflow pump, and the vacuum pump and chamber. The complete model has 17 state variables. The inputs are the reference voltages to the blood pump and the backflow pump, the normalized current inputs to the valves (one inlet and one outlet valve per reservoir[4]) and the vacuum pump on/off signal. The outputs are the pressures in the reservoirs and the blood-pump flow rate. The model is based on first principles, and the parameters are identified using static and dynamic measurements from the mock circulation. Each submodel is identified individually. The static behavior of the blood pump (parameters R_l, R_q, and k) is identified using a slow pump-speed ramp, whereas the dynamic behavior (parameter L) is identified using a chirp signal on the applied pressure head. For the identification of the air valves, the two fluid ports of one receiver are clamped, i.e., the air volume stays constant. Pulse signals of various levels are then sent to the valves, and the resulting pressure is measured. This procedure allows a concurrent identification of the temperature dynamics, which are visible in the pressure when all valves are closed. The parameters of the backflow pump and the vacuum pump are determined using the data sheet from the manufacturer.

In order to obtain a linear single-input single-output (SISO) model of the plant, four steps are taken: First, an artificial valve input is created, which simultaneously actuates the inlet and outlet valves.[5] Second, all inputs except for the two valve inputs and all outputs except for the two pressures are omitted. Third, the model is linearized numerically at a nominal steady-state setpoint. And fourth, the cross-couplings between the two tanks are analyzed in order to determine whether a multiple-input multiple-output (MIMO) controller is necessary or if two SISO controllers are sufficient. The analysis of the cross-couplings is made by calculating

[4] There are two outlet valves per reservoir, but the two valves are actuated with the same current signal.

[5] An increasing value of the artificial valve input concurrently opens the inlet valve and closes the outlet valve from their nominal positions.

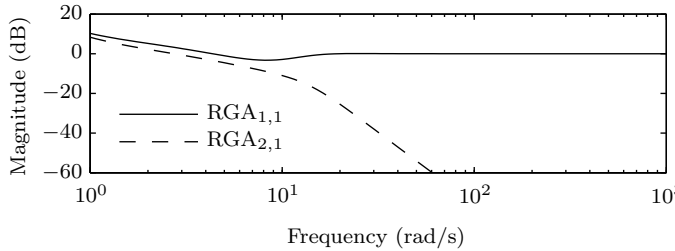

Figure 2.9: Analysis of the relative gain array transfer function to determine the cross-couplings of the MIMO system. The magnitude of $\mathrm{RGA}_{1,1}$ shows the influence of the valve input on the corresponding pressure; the magnitude of $\mathrm{RGA}_{2,1}$ shows the influence of the valve input on the pressure in the other tank.

the relative gain array (RGA) transfer function [52]. Figure 2.9 shows the magnitude plots of one diagonal and one off-diagonal entry of the RGA. Clearly, up to a frequency of $10\,{}^{\mathrm{rad}}/_{\mathrm{s}}$, the cross-couplings are relevant, i.e., a change in the pressure in one tank has an influence on the pressure in the other tank (via the fluid, which is moved through the blood pump). At higher frequencies, the inertance of the fluid attenuates these disturbances such that the pressures can be considered independent. Because the two pressure control systems both have a bandwidth above $100\,{}^{\mathrm{rad}}/_{\mathrm{s}}$, the dynamics of the fluid does not have to be considered for their derivation, i.e., two SISO controllers are sufficient for the pressure control task. The linear SISO model of sixth order $P(s)$ therefore only includes the temperature and pressure dynamics of one receiver with a constant volume, the vacuum chamber pressure dynamics, and the valve dynamics. The states describing the other pressure chamber, the dynamics of the fluid, the blood-pump, and the backflow pump can be ignored. Three independent equilibrium values must be chosen for the linearization, namely the pressure in the air receiver p_0, the air-mass flow through the valves $\overset{*}{m}_0$, and the volume of the air receiver V_0. For the calculation of the nominal model $P(s)$, these values were chosen to be $p_0 = 1.1\,\mathrm{bar}$, $\overset{*}{m}_0 = 0.1\,{}^{\mathrm{g}}/_{\mathrm{s}}$, and $V_0 = 0.2\,\mathrm{l}$, respectively. The transfer function of the nominal plant is given by

$$P(s) = \frac{\sum_{j=0}^{4} b_j \cdot s^j}{\sum_{i=0}^{6} a_i \cdot s^i}, \tag{2.7}$$

where the coefficients b_j and a_i are listed in Table 2.3. This is the model used for the synthesis of the two pressure controllers. For the calculation

Table 2.3: Coefficients of $P(s)$

Coefficient	**Value**	**Coefficient**	**Value**
a_0	$4.608 \cdot 10^5$	b_0	$2.913 \cdot 10^6$
a_1	$8.910 \cdot 10^5$	b_1	$5.003 \cdot 10^6$
a_2	$4.607 \cdot 10^5$	b_2	$1.995 \cdot 10^6$
a_3	$7.051 \cdot 10^4$	b_3	$1.617 \cdot 10^5$
a_4	$4.203 \cdot 10^3$	b_4	$3.159 \cdot 10^3$
a_5	$1.077 \cdot 10^2$		
a_6	1		

of the nominal model $P(s)$, these

Chapter 3

Emulation of Ventricular Suction on the Hybrid Mock Circulation

Ventricular suction occurs when a turbodynamic VAD tries to pump more blood from the ventricle than is available. Suction causes a stagnation of the blood flow and can damage the heart muscle and must therefore be avoided in clinical practice. This chapter shows how ventricular suction is implemented on the hybrid mock circulation to allow testing of suction detection algorithms and physiological VAD controllers. Experimental results show that suction can be emulated as desired.
The content of this chapter is completely taken from [22].

3.1 Introduction

Mechanical circulatory support denotes the use of mechanical pumps to support the blood circulation of patients suffering from heart failure. In the last decade, MCS has gained much significance for the treatment of heart failure. This increase yields from a shortage in donor hearts and from improved outcomes of MCS. The most important class of MCS devices are turbodynamic VADs [10]. Turbodynamic VADs, also known as rotary VADs or continuous-flow VADs, are pumps with a spinning rotor exerting a pressure on the blood. VADs are implanted between the LV or the LA and the aorta, or between the RV or the RA and the pulmonary artery, i.e., they pump in parallel to the failing heart. Nowadays, clinically used VADs are operated at a constant pump speed, which is chosen by the physician or the patient. This mode of operation lacks an adaptation of the pumping function to the requirement of the patient and therefore reduces the quality of life of VAD recipients. To overcome this problem,

control algorithms for a physiological adaptation of VADs have been developed [46, 15].
The task of a physiological VAD controller is the adaptation of the pump speed to meet the patients blood perfusion requirement in a safe manner. The requirements which need to be met by the controller are manifold, but the hard constraints, which limit the allowed pump speed, are easily explained in the following. When the pump speed is chosen too low, the blood flows backwards through the pump, which potentially increases blood damage (hemolysis, platelet activation) and leads to a congestion in the pulmonary veins, potentially causing lung edema. When the pump speed is chosen too high, the ventricle is emptied and the ventricular wall gets sucked onto the inflow cannula of the VAD. This event is called suction and is dangerous because the blood flow is disturbed and the heart muscle can be injured. It is therefore necessary for any VAD controller that suction is avoided.
VAD controllers are tested in different types of models, namely numerical models, mock circulation models, and animal models. These models have their advantages and disadvantages and are all used during the development of VAD controllers. In order to properly test VAD controllers, these models must be able to emulate suction. Animal models inherently offer this feature. For classic mock circulations and numerical models, approaches to emulate ventricular suction have been presented in the literature [53, 54].
Chapter 2 introduces the hybrid mock circulation, which integrates a numerical model and a classic mock circulation, combining the advantages of both models. Thus far, this test bench has not been able to emulate suction. In this chapter we present a method to implement ventricular suction on a hybrid mock circulation. Experimental results are provided, which show that the reference pressures during suction cannot be tracked accurately, but the overall behavior of suction can be emulated sufficiently well.

3.2 Materials and methods

3.2.1 Hybrid mock circulation

Overview

The hybrid mock circulation developed in our group consists of a numerical model of the human blood circulation running in real-time and a numerical-hydraulic interface to allow an interaction between this numerical model and a real VAD. Whereas the numerical circulation model was developed based on existing work [43], the interface was developed specifically for the purpose of the hybrid mock circulation. Figure 3.1 shows a picture of this interface. The fluid circuit of the interface consists of two pressure-controlled reservoirs (a), (b), the blood pump (c), and the backflow pump (d). The blood pump is the device to be tested. Again, the Deltastream DP2 is used as the blood pump. The blood-pump controller is described in more detail below. The backflow pump (d) is installed in the circuit to keep the fluid-level in the two reservoirs (a), (b) constant despite a flow through the blood pump. The input to the backflow pump controller is the fluid-level in the reservoirs measured by infrared range finders (e). The pressure in the reservoirs is controlled to track the reference signals from the numerical circulation model. The pressure in each reservoir is controlled independently using pressurized air. The pressure control system consists of one proportional solenoid inlet valve and two proportional solenoid outlet valves (f) per reservoir, a vacuum pump (g) and a vacuum receiver (h), one air-pressure sensor (i) per reservoir, and one fluid-pressure sensor per reservoir (not visible in picture). The pressure control algorithm is described in more detail below.

Depending on the pump speed and the pressure difference across the pump, a flow rate results, which is measured using clamp-on ultrasonic flow probes (k). The measured flow rate signal from one probe is fed back to the numerical circulation model, where it is used as an outflow from the LV and an inflow to the aorta. This setup allows a real-time interaction between the simulated blood circulation and the real blood pump. In the previous chapter, the overall delay from a reference pressure signal to a measured flow signal was identified to be approximately 10 ms. The test bench is equipped with a PC running MATLAB Real-Time Windows Target, which executes five tasks: simulation of the numerical circulation model, data logging, blood-pump control, backflow pump control, and pressure con-

trol.
The numerical circulation model from [43] consists of a systemic and a pulmonary circulation, each with an arterial and a venous part. The arterial trees are modeled by five-element Windkessel models; the venous parts are modeled by three-element Windkessel models [2]. The pressure in both arterial trees is regulated by a baroreflex, which adapts the respective arterial resistance. The CO is controlled by an autoregulation mechanism, which adapts the unstressed volume of the systemic veins. The heart consists of two atria and two ventricles, all of which are contracting actively triggered by a time-varying elastance model. Figure 3.2(a) shows measured PV diagram for the circulation model in different conditions obtained at the hybrid mock circulation. The time-varying elastance model is implemented by a time-varying function $F_{\mathrm{tve}}(t) \in [0, 1]$ (see Figure 3.2(b)), which indicates the contractile state of the muscle fibres and which is used to interpolate between the dashed lines in Figure 3.2(a). The upper dashed line is not touched by the PV loop due to the modeled visco-elasticity of the LV during systole.

Blood pump controller

The blood pump is equipped with an industrial motor-control unit. In the original setup of the test bench, the motor-control unit was operated in speed-control mode, i.e., an analog signal from the test bench PC was used as the reference pump speed. Because many VAD controllers and suction detection algorithms make use of the pump motor current signal, a measurement of this signal is required in the setup. The measurement of the current in the three motor phases rendered impractical and the digital output of the motor-control unit could not be used because the sampling rate is too low.
In order to get an estimate of the motor current, the speed control of the blood pump is implemented as a cascaded control system, where the outer speed-control loop is running on the test bench PC and the inner current-control loop is running on the motor-control unit. The motor-control unit is therefore operated in current-control mode, i.e., the analog signal from the PC is a reference current signal. Because the current control has a bandwidth of 600 Hz, the reference current available on the PC is used as an estimate of the actual motor current.
The speed-control loop implemented on the PC is a PI controller. The

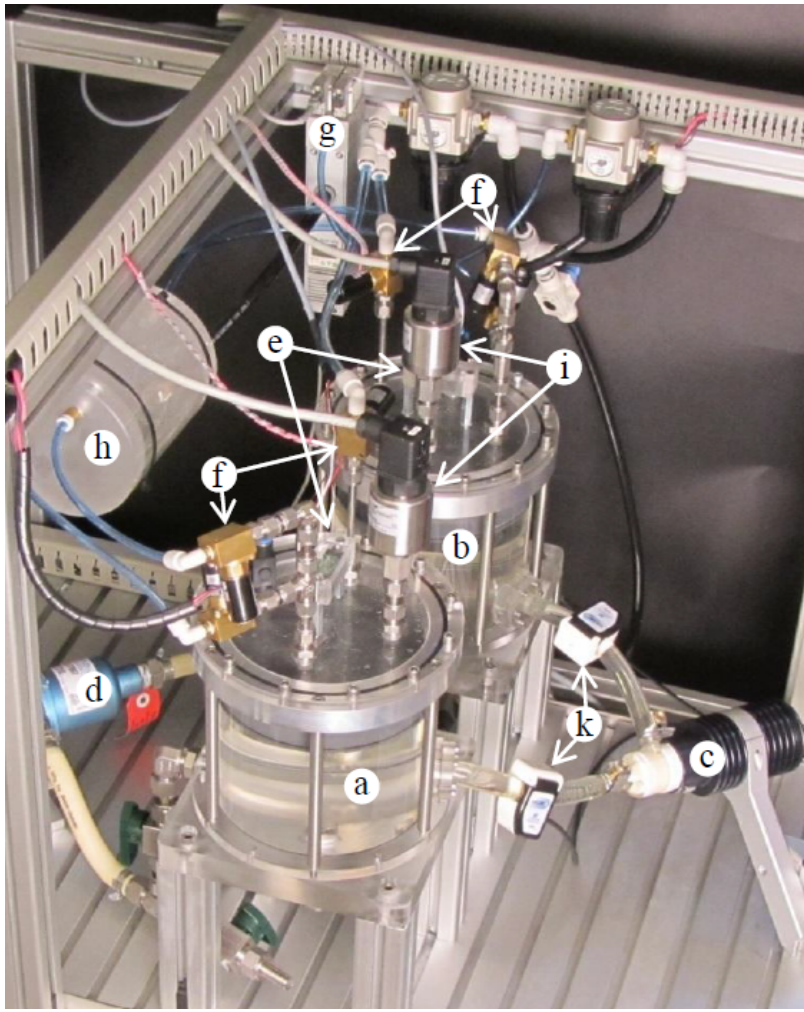

Figure 3.1: Picture of the hybrid mock circulation consisting of two pressure-controlled reservoirs (a), (b), a blood pump (c), a backflow pump (d), two fluid-level sensors (e), one proportional solenoid inlet valve and two proportional solenoid outlet valves (f) per reservoir, a vacuum pump (g), a vacuum receiver (h), two air-pressure sensors (i), and two ultrasonic flow probes (k). The two fluid-pressure sensors are not visible from this angle.

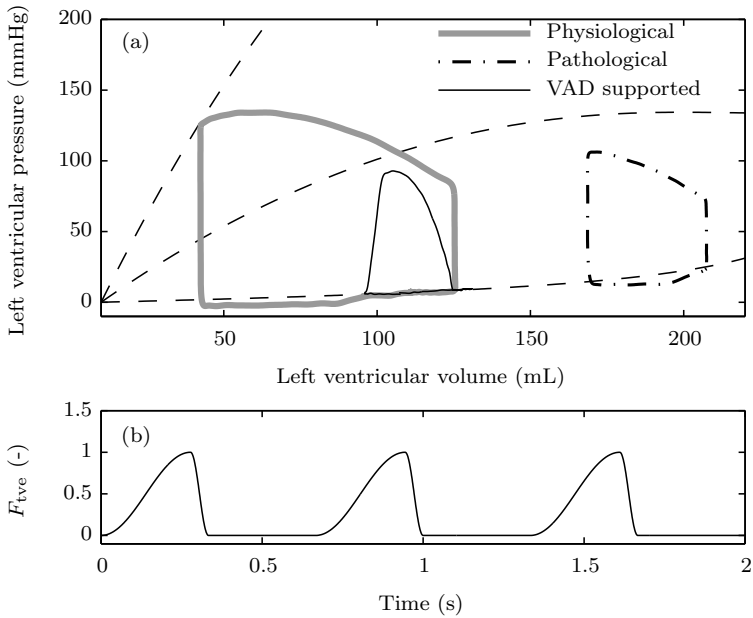

Figure 3.2: Panel (a) shows measured PV loops from the hybrid mock circulation. The loops labelled "Physiological" and "Pathological" were obtained with a clamped pump cannula; the loop labelled "VAD supported" was obtained with the pathological circulation and a pump speed of 4180 rpm. The dashed lines are used for the calculation of the time-varying elastance. Panel (b) shows a 3 s excerpt of the trigger function for the time-varying elastance. This function is used to interpolate between the dashed lines in panel (a).

transfer function is given by [44]

$$C_s(s) = k_{p,s} \cdot \left(1 + \frac{1}{T_{i,s} \cdot s}\right), \tag{3.1}$$

where s is the Laplace variable, $k_{p,s}$ =0.005 $^{\mathrm{A}}/_{\mathrm{rpm}}$ is the proportional gain and $T_{i,s} = 0.2\,\mathrm{s}$ is the integrator time constant. The measured pump speed signal is low-pass filtered by a second-order infinite impulse response (IIR) filter. The transfer function of this filter is given by

$$F_s(s) = \left(\frac{1}{\tau_s \cdot s + 1}\right)^2, \tag{3.2}$$

where $\tau_s = 0.0045\,\mathrm{s}$ is the filter time constant.

Pressure controller

The most challenging task of the numerical-hydraulic interface is the pressure control of the two reservoirs. Two SISO controllers are implemented for this task. In order to improve the pressure control for the suction emulation, the controllers were changed from their initial implementation described in Section 2.2.3. The input to the controllers is the deviation of the measured from the reference pressure signal; the output is the current sent to the proportional inlet and outlet air valves. Proportional-integral-derivative (PID) controllers are used; their transfer function is given by [44]

$$C_p(s) = k_{p,p} \cdot \left(1 + \frac{1}{T_{i,p} \cdot s} + T_{d,p} \cdot s\right), \tag{3.3}$$

where $k_{p,p}$ is the proportional gain, $T_{i,p}$ is the integrator time constant, and $T_{d,p}$ is the derivative time constant. The two pressure controllers have different specifications and parameters. The specifications include zero steady-state error, a small step-response overshoot, and a high bandwidth. Table 3.1 lists the parameters for the pump inlet and the pump outlet pressure controllers. The resulting control systems have a bandwidth of 25.5 Hz and 27.2 Hz, respectively.

Table 3.1: Pressure Controller Parameters

Pump inlet / LV		**Pump outlet / aorta**	
Parameter	**Value**	**Parameter**	**Value**
$k_{p,p}$	$4 \cdot 10^{-5}\,\mathrm{Pa}^{-1}$	$k_{p,p}$	$3 \cdot 10^{-5}\,\mathrm{Pa}^{-1}$
$T_{i,p}$	0.1 s	$T_{i,p}$	0.1 s
$T_{d,p}$	0.005 s	$T_{d,p}$	0.01 s

3.2.2 Suction model

Suction describes the phenomenon when a VAD tries to pump more blood from the ventricle than is available. Since the test bench is a hybrid mock circulation, there exist two possibilities to implement suction. The first option is to use a hardware device on the inflow cannula of the VAD, which can block the flow when suction occurs. A possible hardware approach is presented in [53]. The second option is to implement a suction model in software and to use the simulated pump inlet pressure as the reference signal for the pressure controller rather than the LV pressure. A possible approach to model suction in a numerical environment is presented in [54]. The major advantage of the hybrid mock circulation over classic mock circulations is its flexibility, which is due to the possibility to change most parameters in the numerical model. Therefore, we decided to pursue the software approach.
The implementation of suction in the numerical model is realized as follows. The signal used as the reference for the pressure controller no longer is the LV pressure $p_{\mathrm{lv}}(t)$ but the pump inlet pressure $p_{\mathrm{pi}}(t)$. These pressures coincide as long as no suction occurs. When suction occurs, the inflow of the cannula is blocked, which is modeled by a suction resistance $R_{\mathrm{suc}}(t)$, and the two pressures differ. The suction resistance can change depending on the suction state and it is computed by

$$R_{\mathrm{suc}}(t) = \begin{cases} 0 & p_{\mathrm{lv}}(t) \geq p_{\mathrm{th}} \\ -r \cdot \left(p_{\mathrm{lv}}(t) - p_{\mathrm{th}}\right) & p_{\mathrm{lv}}(t) < p_{\mathrm{th}}, \end{cases} \tag{3.4}$$

where $r = 3.5\,{}^{\mathrm{s}}/_{\mathrm{mL}}$ is a gain, and $p_{\mathrm{th}} = 0\,\mathrm{mmHg}$ is the suction pressure threshold. The pump inlet pressure $p_{\mathrm{pi}}(t)$ downstream of this resistance is

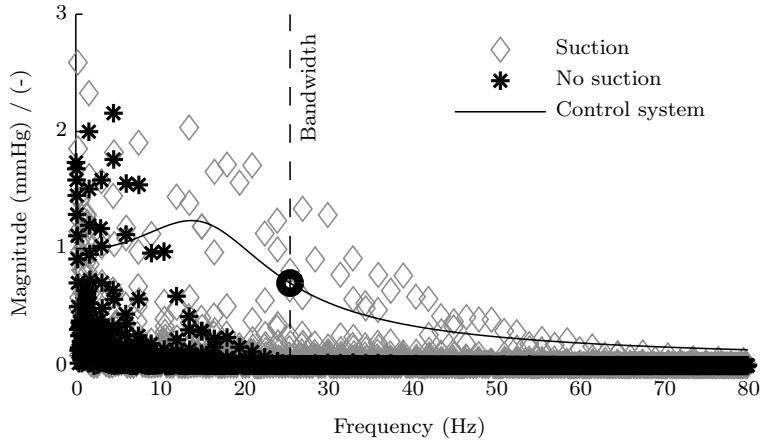

Figure 3.3: Fourier analysis of the reference pressure signals at the pump inlet. The solid line represents the magnitude of the closed-loop transfer function of the pressure control system; the vertical line shows where this magnitude drops below -3 dB. Clearly, the frequency content of the reference signal without suction is below the bandwidth whereas this is not the case for the signal with suction. Accurate reference tracking can thus only be ensured when no suction occurs. The axes are cropped for a better visibility of the relevant features.

computed by

$$p_{\mathrm{pi}}(t) = p_{\mathrm{lv}}(t) - R_{\mathrm{suc}}(t) \cdot q_{\mathrm{vad}}(t), \tag{3.5}$$

where $q_{\mathrm{vad}}(t)$ is the VAD flow rate.

3.2.3 Frequency analysis of reference signal

The main problem for an emulation of suction in the hybrid mock circulation is the higher frequency content of the pump inlet pressure reference signal during suction. Figure 3.3 depicts the frequency spectrum of $p_{\mathrm{pi}}(t)$ with suction and without suction together with the closed-loop transfer function of the pressure controller. Clearly, the bandwidth of the control system is high enough to track the reference signal without suction, but will not be able to accurately track the reference signal with suction. Due to delays in the control system, a significant increase of the bandwidth is not possible without sacrificing the robust behavior of the controllers.

3.2.4 Experiments

Two experiments are conducted at the test bench for this chapter. Both experiments are inspired by in vivo suction measurements. The goal of the experiments is an analysis of the reference tracking during suction and an analysis of the overall suction emulation. For both experiments, the numerical circulation model is set to a pathological state by reducing the LV contractility to 34% of the physiological value and by setting the HR to 90 bpm [43].

Pump speed ramp

The first experiment inspired by [55] consists of a slow pump speed ramp from 3000 rpm to 7000 rpm. This experiment is conducted to analyze the reference tracking behavior of the controller and to analyze the overall behavior of suction.

Suction indices

In the second experiment inspired by [56], the pump speed is increased from 3800 rpm to 5800 rpm in steps of 200 rpm. At every step, the speed is held constant for 30 s of which the last 10 s are used to calculate two

suction indices. The pulsatility index (Π_{ind}) is a time-domain index and is calculated by

$$\Pi_{\text{ind}} = \frac{\max\left(x_{\text{vad}}(t)\right) - \min\left(x_{\text{vad}}(t)\right)}{2}, \tag{3.6}$$

where $x_{\text{vad}}(t)$ is either the pump flow rate $q_{\text{vad}}(t)$, the pump motor current $I_{\text{vad}}(t)$, or the pump pressure head $h_{\text{vad}}(t)$. This index describes the amplitude of the respective signal. The harmonic index (Θ_{ind}) is a frequency-domain index and is calculated by

$$\Theta_{\text{ind}} = \frac{\int_{f_0-\delta f}^{f_0+\delta f} X_{\text{vad}}(f)\mathrm{d}f}{\int_{f_0+\delta f}^{f_{\max}} X_{\text{vad}}(f)\mathrm{d}f}, \tag{3.7}$$

where f is the frequency variable, f_0 is the fundamental frequency (HR), $\delta f = 0.1\,\text{Hz}$ is a frequency window constant, $f_{\max} = 80\,\text{Hz}$ is the maximum frequency, and $X_{\text{vad}}(f)$ is the magnitude of the discrete Fourier transform of either the pump flow rate, the pump motor current, or the pump pressure head. This index describes the ratio between the integral over the fundamental frequency and the integral over the higher harmonics. The second experiment is conducted to make a quantitative assessment of the suction emulation.

3.3 Results

3.3.1 Pump speed ramp

Figure 3.4 shows the experimental results of the pump speed ramp from 3000 rpm to 7000 rpm. Figure 3.4(a) shows the reference and the measured pump speed. The small oscillations visible in the measured pump speed signal with the same frequency as the HR are caused by the changing hydraulic load from the beating heart. Figure 3.4(b) shows the reference and the measured pump inlet pressure and the simulated LV pressure. The reduction of the pressure in the ventricle is caused by the increasing flow rate through the pump, which reduces the blood volume in the ventricle. After 23 s suction occurs, which causes the pump inlet pressure to become increasingly negative while the LV pressure stays around 0 mmHg. From the agreement between the reference and the measured signal, one can see that the reference tracking is accurate before suction but not anymore during suction. Figure 3.4(c) shows the measured pump flow rate. This measurement shows the typical reduction of the flow pulsatility toward suction and the distorted flow rate signal during suction. Figure 3.4(d) shows the pump motor current. Similar to the flow rate signal, the motor current gets less pulsatile toward suction and is distorted with high-frequency oscillations during suction.

3.3.2 Suction indices

Figure 3.5 shows the results of the analysis of the suction indices. The indices are computed using (3.6) and (3.7) on the measured pump flow rate, the pump motor current, and the pump pressure head. All six indices show a clear minimum around the onset of suction.

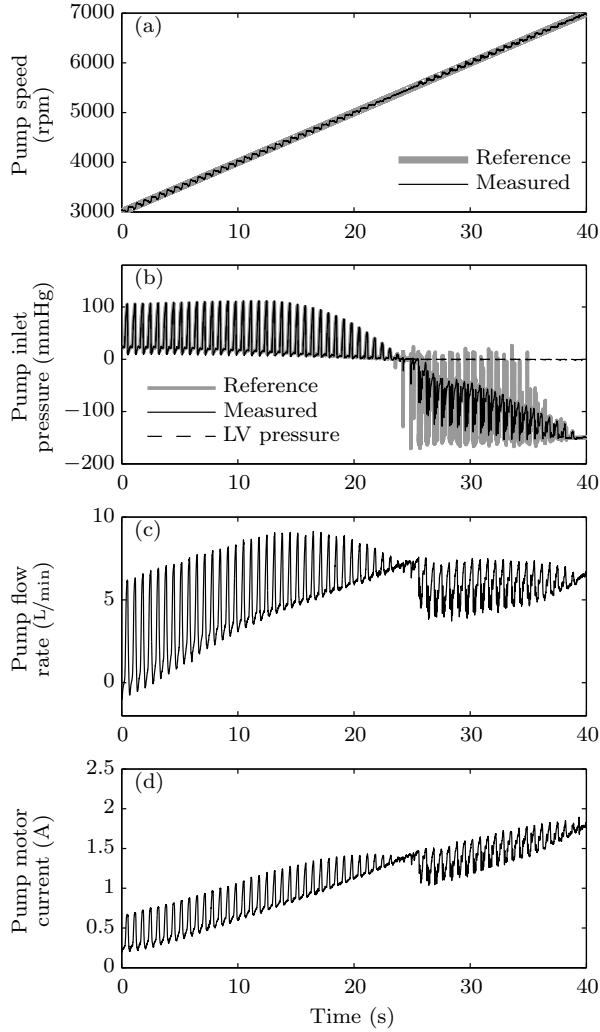

Figure 3.4: Suction emulation experimental results. Panel (a) shows the time course of the reference and the measured pump speed. Panel (b) shows the time course of the reference and the measured pump inlet pressure. The reference tracking is accurate before suction but not anymore during suction. The simulated LV pressure (dotted line) coincides with the pump inlet pressure before suction but does not become negative. Panel (c) shows the resulting pump flow rate. Panel (d) shows the required motor current for the pump.

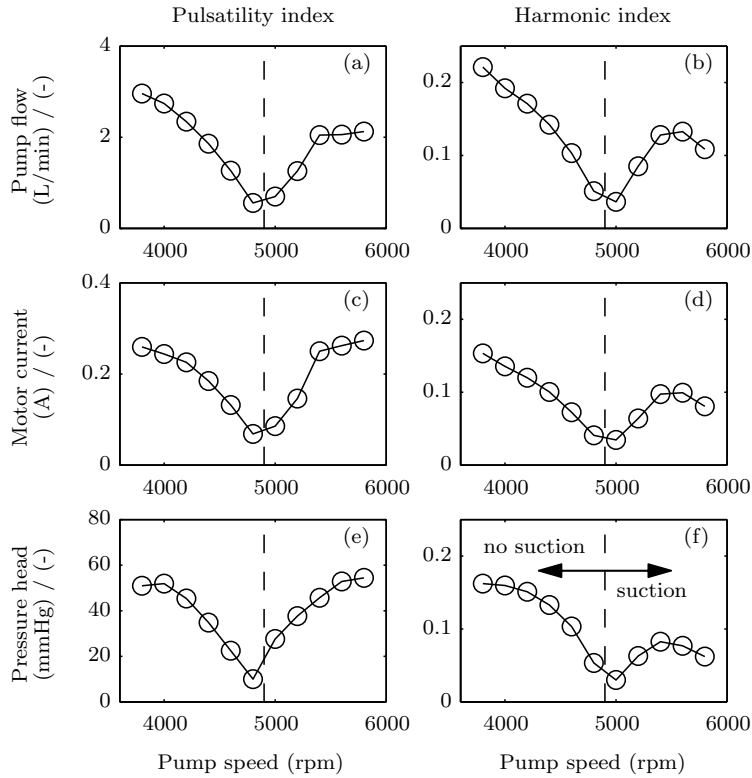

Figure 3.5: Analysis of two suction detection indices. The pump speed is increased from 3800 rpm to 5800 rpm in steps of 200 rpm and held constant for 30 s. The last 10 s of every step are taken to compute the indices using (3.6) and (3.7). The panels on the left hand side represent the pulsatility index (Π_{ind}) in the respective unit; the panels on the right hand side represent the harmonic index (Θ_{ind}), which has no unit. Panels (a) and (b) show the indices for the pump flow rate; panels (c) and (d) show the indices for the pump motor current; panels (e) and (f) show the indices for the pump pressure head. All pump speed values above 4800 rpm yield ventricular suction.

3.4 Discussion

This chapter presents an approach to emulate ventricular suction on the hybrid mock circulation. The mock circulation is a highly flexible, physiological test bench for VADs. It has been developed as a testing environment for VAD controllers and pressure or flow observers [23] and the results from this chapter show that the test bench is also able to emulate ventricular suction. With this improvement, the hybrid mock circulation is becoming an alternative method for preliminary animal experiments.

Figure 3.4 shows that the pressure controller is not able to accurately track the reference signal. This behavior was predicted by an analysis of the frequency content of the reference signals with and without suction (see Figure 3.3). Nevertheless, the overall behavior of suction agrees well with in vivo experimental results [55]. This observation can also be explained by the analysis in Figure 3.3. The bandwidth of the pump inlet pressure controller lies at 25.5 Hz, but the amplitude spectra of $p_{\mathrm{pi}}(t)$ and $p_{\mathrm{lv}}(t)$ already differ significantly below the bandwidth when suction occurs. Additionally, the reference tracking at e.g. 30 Hz is not accurate, but the output still has more than half the amplitude of the reference signal.

Figure 3.5 shows a quantitative analysis of the suction emulation. Even though the numbers do not exactly match numbers from in vivo experiments [56], it is assumed that the variability between different in vivo experiments (different animal, different pump, different positioning of the cannula) is in the same range. All six indices show a clear minimum around the onset of suction. Figure 3.4 and 3.5 show a difference in the pump speed when suction occurs. The reason for this difference is the relatively fast pump speed ramp in the first experiment compared to the second one, i.e., the first experiment includes the dynamics of the circulation model, whereas the second experiment shows a steady-state analysis.

Part II

Preload Responsive Speed (PRS) Controller

Chapter 4

In vitro Evaluation of the PRS Controller

The current chapter presents a novel physiological control algorithm for VADs, which is inspired by the PRSW. This controller adapts the hydraulic power output of the VAD to the EDV of the LV. We tested this controller on a hybrid mock circulation where the LV volume is known, i.e., the problem of measuring the LV volume is not addressed in the current chapter. Experiments were conducted to compare the response of the controller with the physiological and with the pathological circulation, with and without VAD support. A sensitivity analysis was performed to analyze the influence of the controller parameters and the influence of the quality of the LV volume signal on the performance of the control algorithm. The results show that the controller induces a response similar to the physiological circulation and effectively prevents over- and underpumping, i.e., ventricular suction and backflow from the aorta to the LV, respectively. The same results are obtained in the case of a disturbed LV volume signal. The results presented in the current chapter motivate the development of a robust, long-term stable sensor to measure the LV volume.
The content of this chapter is completely taken from [23].

4.1 Introduction

Heart transplantation remains the gold standard for the treatment of patients with end-stage heart failure. However, the gap between an increasing number of transplantation candidates and a shortage of suitable organs urges physicians to look for alternative therapies. VADs were originally conceived for bridging to transplantation, but the recent developments progressively allowed them to be considered for destination therapy (permanent implantation) [11] or possibly for bridging toward recovery (tem-

porary implantation until spontaneous sufficient functional recovery of the native heart) [12]. While recovery is the most desirable outcome of VAD therapy, it occurs unfortunately only in very few patients and often only to a limited extent that does not permit the VAD's weaning and explantation. VADs can be categorized into three pump-type generations [10]. First-generation VADs include pneumatically or electrically actuated pulsatile volume-displacement pumps. Based on a chamber with two unidirectional (inflow and outflow) valves, these types of VADs imitate the working principle of the human heart. Although bulky, noisy and energetically inefficient, they provide a physiological pulsatile perfusion. Pulsatile VADs are nowadays used mainly for bi-ventricular support, where both the RV and the LV fail. Second- and third-generation VADs are axial and centrifugal turbodynamic pumps, respectively. These pumps generate a pressure by a spinning rotor in the blood stream and generate a continuous, low-pulsatile flow. The rotor is either fixed by mechanical bearings or suspended by hydrodynamic or magnetic levitation. As compared to first-generation systems, they are smaller, quieter, more efficient, and more reliable.
Current turbodynamic VADs sometimes employ periodical speed variations for pump washout and can intermediately reduce the speed when suction occurs. Besides that, they are operated at a constant speed, and therefore have only limited ability to adapt to varying pre- and afterload conditions which occur when VAD patients are discharged from the hospital. The requirements for physiological VAD control are manifold and potentially conflicting [57]. As long as the pump speed is not modulated during one heartbeat (speed pulsing), a controller for a turbodynamic VAD has only one degree of freedom–the pump speed–and thus cannot meet several requirements simultaneously. The set of requirements thus can be reduced to one task: The physiological controller must prevent overpumping or underpumping, and within these limits, adapt the pump speed to meet the patient's requirement. Overpumping denotes a misactuation of the VAD where the pump speed is set too high, which may lead to suction and collapse of the LV walls [17]. Conversely, underpumping describes a situation where the pump speed is set too low, so that backflow through the pump may occur with subsequent possible congestion upstream of the LV (lung edema). Stagnation or backflow in the pump additionally promotes hemolysis [16], which is to be avoided.

The control of turbodynamic VADs has been extensively researched during the last three decades. Many of the publications related to VAD control do not describe controllers in the classical sense, but rather present algorithms with which suction can be detected [17, 58, 59, 60, 61, 62, 63, 64, 65, 54]. Such suction detectors alone can be used as physiological controllers by operating the pump close to the speed which would eventually lead to ventricular suction. This strategy imitates the Frank-Starling law [1], since the VAD flow adapts to the venous return. If a suction detector alone is used for VAD control, it must be able to differentiate between various levels of suction, such that a certain level of suction can be maintained. Most commonly, a suction detector is used as an add-on to a physiological controller. In this case, the physiological controller adapts the pump speed according to the patient's perfusion requirement. As soon as suction occurs, the physiological controller is overruled by the suction detector to apply a suction release strategy.

Physiological controllers can be subdivided into four categories: preload-based, afterload-based, HR-based, and multivariable controllers. Preload-based controllers [66, 46, 67, 68, 69, 70, 15] adapt the pump speed according to a parameter which is mostly influenced by the preload of the LV such as the pulsatility of the flow or the motor current, or the gradient of the pump flow versus the pump speed. These controllers try to imitate the Frank-Starling law of the heart. Afterload-based controllers [71, 72, 73, 74] adapt the pump speed according to the aortic pressure or the pump pressure head. These controllers intend to keep aortic pressure (or the pump pressure head) constant, such that the CO is regulated via the vascular resistance. HR-based controllers [75, 15] detect the HR of the patient and adapt the pump speed according to a predefined relationship between the HR and the desired pump flow. Complex multivariable controllers [76, 77] try to estimate the state of the cardiovascular system and adapt the pump speed to meet several constraints simultaneously.

In the current chapter we present a novel control algorithm for VADs, which is based on a measurement of the LV volume. This algorithm addresses the problem of finding an appropriate pump speed in order to prevent dangerous situations like ventricular suction and to improve the quality of life of VAD patients by imitating the function of the native heart. The algorithm extracts the EDV and the HR from the LV volume signal and constitutes a combination of a preload-based and an HR-based

controller. The controller we describe will be named “preload responsive speed controller” (PRS controller) from here on. The current chapter includes experimental results obtained from a hybrid mock circulation and a sensitivity analysis of the PRS controller toward a disturbed LV volume signal.

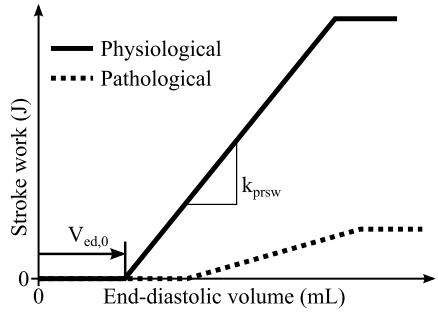

Figure 4.1: Theoretical description of the preload recruitable stroke work (PRSW) for a physiological and a pathological heart.

4.2 Materials and methods

4.2.1 PRS controller

The PRS controller presented in the current chapter is based on the theory of venous return [1] and the Frank-Starling law of the heart. In [4] the authors present the concept of the PRSW (see Figure 4.1) as a linear, afterload-independent model of the Frank-Starling law. This model states that the stroke work of the LV increases linearly with the EDV. An increased contractility of the LV increases the slope of the PRSW [78]. The PRSW of a pathological LV has a decreased slope, a lower maximum value, and is shifted rightwards, if the LV is dilated. Since the output (stroke work) of the heart is proportional to the input (EDV), the PRSW can be understood as a proportional controller for the hydraulic work generated by the LV. The PRS controller presented in the current chapter imitates the PRSW by a proportional controller that computes the desired pump work per heartbeat based on the measured EDV. Multiplied with the measured HR of the pathological LV, this work can be converted to a desired hydraulic pump power.

Figure 4.2 shows the structure of the PRS controller with the measured LV volume $V_{\mathrm{lv}}(t)$ as the input and the desired pump speed $N_{\mathrm{des}}(t)$ as the output. It is implemented as a discrete-time system with a sampling time of 10 ms. The structure of the controller can be subdivided into three stages. In the first stage, signal processing algorithms are used to determine the EDV $V_{\mathrm{ed}}(t)$ and the HR from $V_{\mathrm{lv}}(t)$. In the second stage,

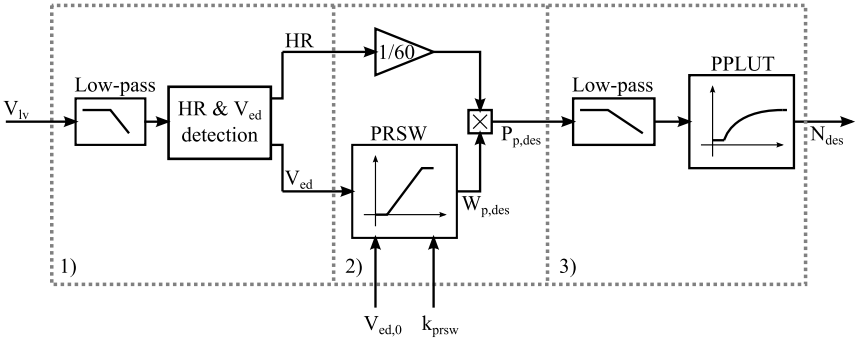

Figure 4.2: Structure of the PRS controller. Stage 1 extracts the HR and $V_{\mathrm{ed}}(t)$ from $V_{\mathrm{lv}}(t)$. Stage 2 calculates the desired hydraulic pump power $\mathrm{P}_{\mathrm{p,des}}(t)$ from the HR and the PRSW. Stage 3 calculates the desired pump speed $\mathrm{N}_{\mathrm{des}}(t)$ to achieve the desired hydraulic pump power. The inputs $V_{\mathrm{ed,o}}$ and k_{prsw} represent the parameters to adapt the PRS controller from patient to patient.

the extracted signals are used to calculate a desired hydraulic pump power imitating the PRSW. The third stage of the algorithm uses the desired pump power to compute a pump speed that approximately achieves the desired pump power. The three stages are detailed in the following.

The first stage of the control structure takes $V_{\mathrm{lv}}(t)$ as the input and computes $V_{\mathrm{ed}}(t)$ as well as the HR. Figure 4.3 illustrates the signal processing procedure for a simulated LV volume signal with subsequently added zero-mean white noise ($\sigma = 5\,\mathrm{mL}$) and a sampling time of 10 ms. First, $V_{\mathrm{lv}}(t)$ is low-pass filtered using a second-order IIR filter with a cut-off frequency of $16.8\,\mathrm{rad/s}$ (2.67 Hz), yielding $V_{\mathrm{lv,filt}}(t)$. Then, using a sliding window, the last 3 s of $V_{\mathrm{lv,filt}}(t)$ are acquired at every time step. Figure 4.3a) shows the 3 s window with the raw and the filtered LV volume signals. The instantaneous HR and EDV values are calculated from this window as follows: First, an affine function is fitted to $V_{\mathrm{lv,filt}}(t)$ using the least-squares method. This affine function represents the offset and a linear trend of the LV volume. Second, this affine function is subtracted from the $V_{\mathrm{lv,filt}}(t)$, which yields a zero-mean sine-like signal as shown in Figure 4.3b). Third, all zero crossings and the direction of their crossing are detected. Fourth, the time intervals between all subsequent downward crossings and all subsequent upward crossings are calculated. Fifth, the HR is calculated from the median of all previously calculated time intervals. And sixth, the maxi-

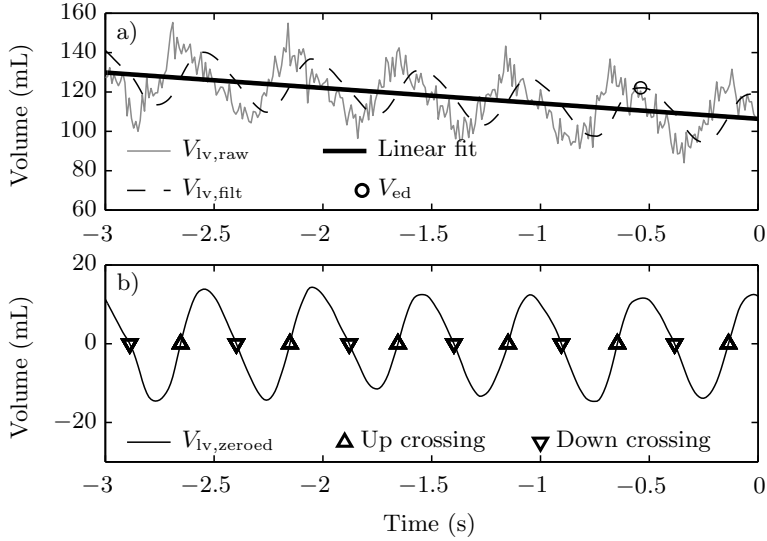

Figure 4.3: Graphical representation of the HR and V_{ed} detection algorithm. The panels show a 3 s sliding window of the raw, the filtered, and the zeroed V_{lv} signals.

mum value of $V_{lv,filt}$ between the last downward crossing and the preceding upward crossing is identified as $V_{ed}(t)$, as indicated in Figure 4.2a). All six steps of the first stage of the control algorithm are repeated at every time-step.

If the HR is irregular, the HR and EDV detection described above is not valid, since $V_{lv}(t)$ does not have a sine-like shape. In such a case, a simplified HR and EDV detection algorithm can be chosen. The simplified algorithm does not calculate the HR but assumes a constant value of 90 bpm. The EDV is detected by identifying the maximum value of the last second of $V_{lv,filt}(t)$.

The second stage of the control structure consists of one part imitating the PRSW and an additional part to include the HR. As a description of the physiological ventricle, the PRSW is a linear relationship between the EDV and the stroke work. In the PRS controller, the PRSW is a linear mapping from the measured $V_{ed}(t)$ to a desired pump work per heart beat $W_{p,des}(t)$:

$$\mathrm{W}_{\mathrm{p,des}}(t) = \left(V_{\mathrm{ed}}(t) - V_{\mathrm{ed},0}\right) \cdot k_{\mathrm{prsw}} \tag{4.1}$$

where $V_{\mathrm{ed},0}$ is the x-axis intercept and k_{prsw} is the gain of the PRSW (see Figure 4.1). When interpreted as a proportional controller, $V_{\mathrm{ed},0}$ is the setpoint and k_{prsw} is the gain. Because the desired hydraulic power would be set to zero when V_{ed} is equal to $V_{\mathrm{ed},0}$, the controller has a steady-state offset, i.e., it normally operates at a larger volume than $V_{\mathrm{ed},0}$. The two parameters $V_{\mathrm{ed},0}$ and k_{prsw} can be adapted by the physician, trained medical personnel, or the patient. The desired hydraulic pump power $\mathrm{P}_{\mathrm{p,des}}(t)$ is calculated by

$$\mathrm{P}_{\mathrm{p,des}}(t) = \mathrm{W}_{\mathrm{p,des}}(t) \cdot \frac{\mathrm{HR}(t)}{60}. \tag{4.2}$$

The third stage of the control algorithm consists of a low-pass filter and a lookup table. The low-pass element is a first-order IIR filter with a cut-off frequency of $1\,{}^{\mathrm{rad}}/_{\mathrm{s}}$ (0.16 Hz). The pump-power lookup table (PPLUT) is a mapping between the hydraulic pump power and the pump speed. The actual power delivered by the pump is not only a function of the pump speed, but it is also a function of the resistance against the pump flow and the fluid viscosity. However, for the implementation in the PRS controller, these dependencies are neglected and the pump speed is directly mapped to a hydraulic pump power. Figure 4.4 shows the PPLUT implemented in the PRS controller. The mapping is not based on the electric power because the efficiency of the pump depends on the operating point, and because the required electric power to generate a desired hydraulic power can be influenced strongly e.g. by a thrombus in the pump. The derivation of the PPLUT and a sensitivity analysis of the PRS controller toward an offset in the PPLUT are provided in Appendix B at the end of this chapter.

4.2.2 Mock circulation

All experiments were conducted using the hybrid mock circulation described in Chapter 2, which is based on a hardware-in-the-loop concept, i.e., the VAD to be tested is a real hydraulic device, whereas the human circulation is completely simulated in software. A numerical-hydraulic interface allows a real-time interaction between the pump and the circulation model. This interface consists of two pressure controlled reser-

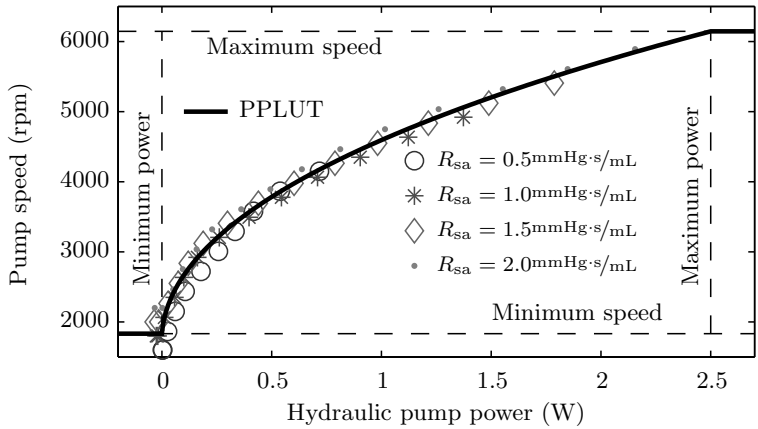

Figure 4.4: The pump-power lookup table (PPLUT) implemented in the PRS controller is used to determine the desired pump speed $N_{des}(t)$ based on the desired hydraulic pump power $P_{p,des}(t)$. The form of the curve illustrates that the hydraulic power is more sensitive to the pump speed when the pump speed is high rather than low. This curve implemented in the PRS controller inverts this behavior, i.e., it reduces the controller gain when the aforementioned sensitivity is high. The markers indicate the experimental results for the derivation of the PPLUT, which is described in Appendix B at the end of this chapter.

voirs and a flow probe. The reservoirs represent the LV and the aorta and are equipped with PI controllers, which apply the pressures from the circulation model to the reservoirs. The VAD is attached to these two reservoirs, i.e., ventriculo-aortic cannulation is simulated. The flow probe (TS410/ME-11PXL, Transonic Systems, Inc., Ithaca, NY) measures the resulting flow through the VAD, which is sent to the circulation model and used as an outflow of the ventricle and an inflow to the aorta. The fluid in the mock circulation is a 2:3 volume mixture of glycerin and water, which mimics the viscosity of blood [42].
The numerical circulation model implemented on the hybrid mock circulation was taken from the literature [43]. The model consists of a systemic and a pulmonary circulation, each consisting of an arterial and a venous part. The heart consists of two actively contracting ventricles and two actively contracting atria. A time-varying elastance model is used to simulate the cardiac contractions. The systemic and the pulmonary pressures are regulated by baroreflex mechanisms, which adapt the respective arterial resistance. The CO is regulated by an autoregulation mechanism, which adapts the unstressed volume of the systemic veins. The incorporates ventricular suction as described in Chapter 3. The model can be adapted to simulate a physiological or a pathological condition. The pathological circulation is simulated by a reduced contractility of the LV, i.e., the maximum elastance is reduced from 3.5 to 0.25 $^{\mathrm{mmHg}}/_{\mathrm{mL}}$. The maximum elastance was evaluated by a simulated vena cava occlusion maneuver. The numerical circulation model runs at 5 kHz; data is stored at 1 kHz.
The experiments described below were conducted using the Deltastream DP2 mixed-flow turbodynamic blood pump. We modified the pump such that the pump speed can be controlled as desired.

4.2.3 Experiments

The experiments conducted are divided into two studies. The first study analyzes the nominal PRS controller and three different baseline measurements. The second study contains experiments to carry out a sensitivity analysis of the PRS controller. This part investigates the sensitivity of the CO and the EDV to changes in the controller parameters (k_{prsw} and $V_{\mathrm{ed},0}$), to the simplified HR and EDV detection algorithm, to changes in the contractility of the pathological LV, as well as to a disturbed LV volume measurement. Table 4.1 lists all configurations investigated.

Two experiments are conducted with each configuration, namely a preload variation experiment and an afterload variation experiment. Figure 4.5 shows the prescribed cardiovascular parameters for the two experiments. The preload variation experiment is conducted by prescribed changes in the unstressed volume of the systemic veins and by changes in the HR. In the physiological circulation the HR is varied between 60 and 80 bpm; in the pathological circulation the HR is varied between and 65 and 135 bpm. The systemic arterial resistance is controlled by the baroreflex, and the CO autoregulation is inactive during the preload variation experiment. The afterload variation experiment is conducted by prescribed changes in the resistance of the systemic arteries and by a constant HR (60 and 90 bpm, respectively). The unstressed volume of the systemic veins is controlled by the CO autoregulation, and the arterial baroreflex is inactive during the afterload variation experiment. For each experiment, the system is run with constant inputs until steady state is reached, at which point the 45 s experiment is started. These experiments do not simulate specific maneuvers, clinical situations, or pharmacological interventions, but they represent fast, wide-range variations of cardiovascular parameters, which pose a challenge for VAD control.
The PRS controller requires a measurement of the LV volume. In the hybrid mock circulation $V_{\mathrm{lv}}(t)$ is not a physical signal but available from the real-time numerical circulation model. Thus, the exact value of $V_{\mathrm{lv}}(t)$ is available at all times and a hardware LV volume sensor is not required for the experiments. The LV volume sensor is emulated by a downsampling of $V_{\mathrm{lv}}(t)$ and adding zero-mean white noise. In the nominal condition, the sampling time of the LV volume sensor is 10 ms and no noise is added.

Baseline and nominal PRS controller study

The first study compares configuration 4 (C4), i.e., the nominal PRS controller, to three baseline experiments (C1, C2, and C3). Configurations C1 and C2 represent the case of the circulation without pump support in a physiological and a pathological circulation, respectively. Configuration C3 represents the current clinical practice with a VAD operated at a constant speed. The speed of 4180 rpm was chosen to achieve a CO of 5 $\mathrm{L/min}$ before the preload or afterload variation starts. Configuration C4 represents the nominal case of the PRS controller with a perfect LV volume measurement and nominal controller parameters. The nominal parameters are $k_{\mathrm{prsw}} =$

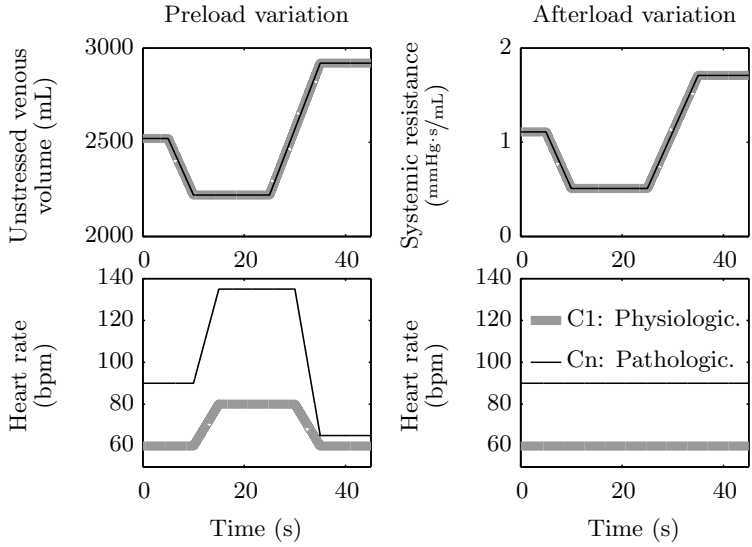

Figure 4.5: Prescribed cardiovascular parameters for the preload and the afterload variation experiments. Table 4.1 lists all configurations C1-C9; Cn denotes the configurations C2-C9. During the preload variation experiment, the systemic resistance is controlled by the baroreflex; during the afterload variation experiment, the unstressed venous volume is controlled by the CO autoregulation.

$10\,^{\mathrm{J}}/_{\mathrm{L}}$ and $V_{\mathrm{ed},0} = 80\,\mathrm{mL}$. With each configuration, the preload variation and the afterload variation experiment are conducted and the following signals are plotted: the CO, the LA pressure, the aortic pressure, and the LV volume. In addition, for C4 the following VAD signals are plotted: the pump speed, the pump flow, and the hydraulic pump power.

PRS controller sensitivity analysis

The second study investigates how the performance of the PRS controller is influenced by changes in the controller parameters, by the simplified HR and EDV detection algorithm, by changes in the LV contractility, and by a disturbed $V_{\mathrm{lv}}(t)$. For each experiment (C5, C6, C7, C8, and C9), the resulting CO and EDV signals are compared to the CO and EDV signals from the nominal controller (C4), which forms the baseline for this second study. For C5, k_{prsw} is changed to 5 and $15\,^{\mathrm{J}}/_{\mathrm{L}}$; for C6, $V_{\mathrm{ed},0}$ is changed to 30 and 130 mL. The latter experiment also corresponds to the situation when the LV volume sensor has an offset. For C7, the contractility of the pathological LV is changed to 0.125 and $1\,^{\mathrm{mmHg}}/_{\mathrm{mL}}$, which simulates a stressful situation or recovery of the LV. For C8, the simplified HR and EDV detection algorithm is used, which determines $V_{\mathrm{ed}}(t)$ as the maximum $V_{\mathrm{lv}}(t)$ value in the last second and assumes a constant HR of 90 bpm. For C9, the LV volume measurement is disturbed as follows. Five different noise levels and four different sampling times are analyzed. The noise is zero-mean and white with a standard deviation of $\sigma = \{0, 2, 4, 6, 10\}\,\mathrm{mL}$; the sampling times analyzed are $\mathrm{Ts} = \{10, 20, 50, 100\}\,\mathrm{ms}$. For each combination of noise and sampling time, the CO and EDV signals are acquired and compared to the CO and EDV signals from C4. The results are quantified by the RMS deviation. Current LV volume sensors typically do not suffer from white noise, but from other types of disturbances like interference in case of admittance catheters. Such disturbances are not investigated in the current thesis, but will have to be investigated once an LV volume sensor is available.

Table 4.1: Configurations for the experiments

Conf.	$\mathbf{E_{max}}$ [mmHg/mL]	**HR** [bpm]	**VAD support**	**HR and EDV detection**	**LV volume "measurement"**	$\mathbf{k_{prsw}}$ [J/L]	$\mathbf{V_{ed,0}}$ [mL]
C1	3.5	60-80	-	-	-	-	-
C2	0.25	65-125	-	-	-	-	-
C3	0.25	65-125	Constant speed	-	-	-	-
C4	0.25	65-125	PRS controller	Nominal	Perfect	10	80
C5	0.25	65-125	PRS controller	Nominal	Perfect	5/15	80
C6	0.25	65-125	PRS controller	Nominal	Perfect	10	30/130
C7	0.125-1	65-125	PRS controller	Nominal	Perfect	10	80
C8	0.25	65-125	PRS controller	Simplified	Perfect	10	80
C9	0.25	65-125	PRS controller	Nominal	Disturbed	10	80

4.3 Results

4.3.1 Baseline and nominal PRS controller study

Figures 4.6, 4.7, and 4.8 show the responses of C1, C2, C3, and C4 to preload and afterload variations. In each figure, the four panels on the left-hand side show the results of the preload variation experiment; the panels on the right-hand side show the results of the afterload variation experiment. The figures show the CO, the LA pressure, the aortic pressure, and the LV volume. The thick gray lines in the background of all three figures represent C1. The thin black lines in the foreground represent C2 (Figure 4.6), C3 (Figure 4.7), and C4 (Figure 4.8), respectively. A comparison of the aortic pressure in all three figures shows a reduced pulsatility for the VAD supported cases, which is caused by the operating principle of the VAD.

Figure 4.6 contrasts the configurations C1 and C2. Clearly, in the pathological circulation the CO and the aortic pressure are generally reduced, whereas the LA pressure and the LV volume are elevated compared to the physiological circulation. The CO in the physiological circulation changes strongly in response to preload variations, while staying almost constant during afterload variations. This behavior reflects the preload sensitivity and afterload insensitivity of the physiological heart. In the pathological circulation, the CO cannot increase in response to a preload increase, since the pathological heart is not able to generate more flow against the given afterload. Only a reduced afterload lets the CO increase in the pathological circulation.

Figure 4.7 contrasts the configurations C1 and C3. Compared to C2, the VAD recovers the CO, the aortic pressure, and the LA pressure to physiological values, as is visible in the first 5 s of the experiments. The pump speed was chosen to achieve a CO of 5 $^{\mathrm{L}}/_{\mathrm{min}}$ under these conditions. As long as the cardiovascular parameters of the patient stay constant, the VAD can restore the hemodynamics to a physiological range. When these parameters change, the chosen pump speed is not appropriate anymore. Clearly, the CO is less sensitive to preload changes and more sensitive to afterload changes compared to the physiological circulation. Additionally, the LV volume and the LA pressure show a large variation, which indicates over- and underpumping when the cardiovascular parameters change.

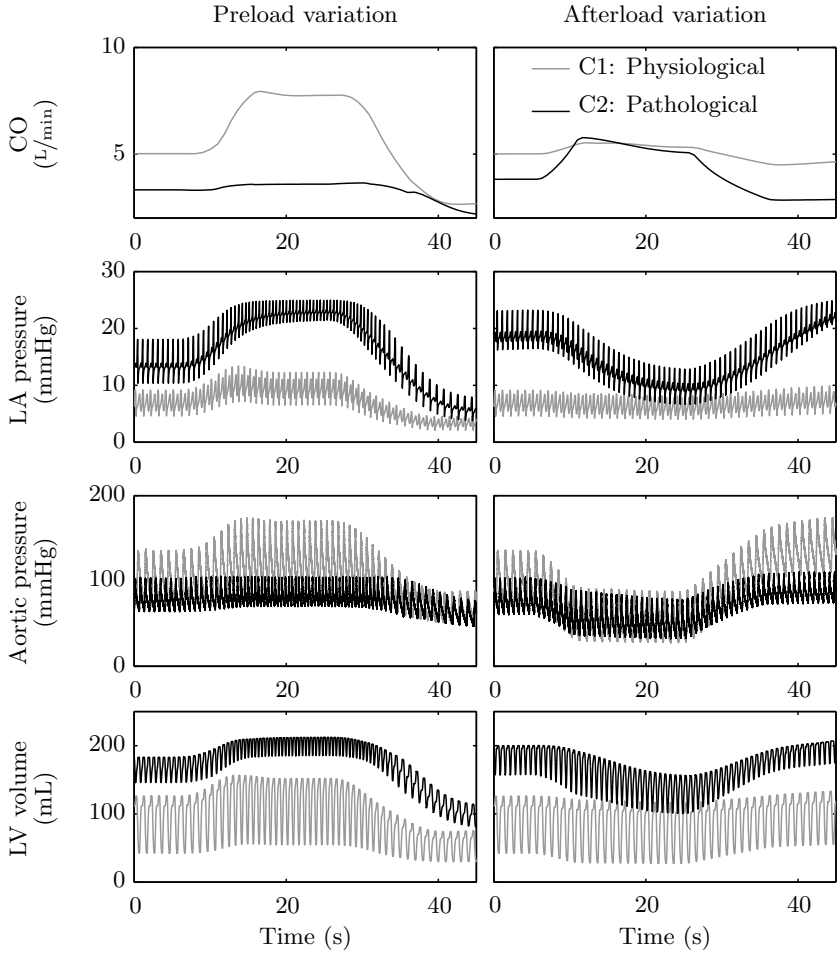

Figure 4.6: Comparison between the physiological and the pathological circulation without VAD support.

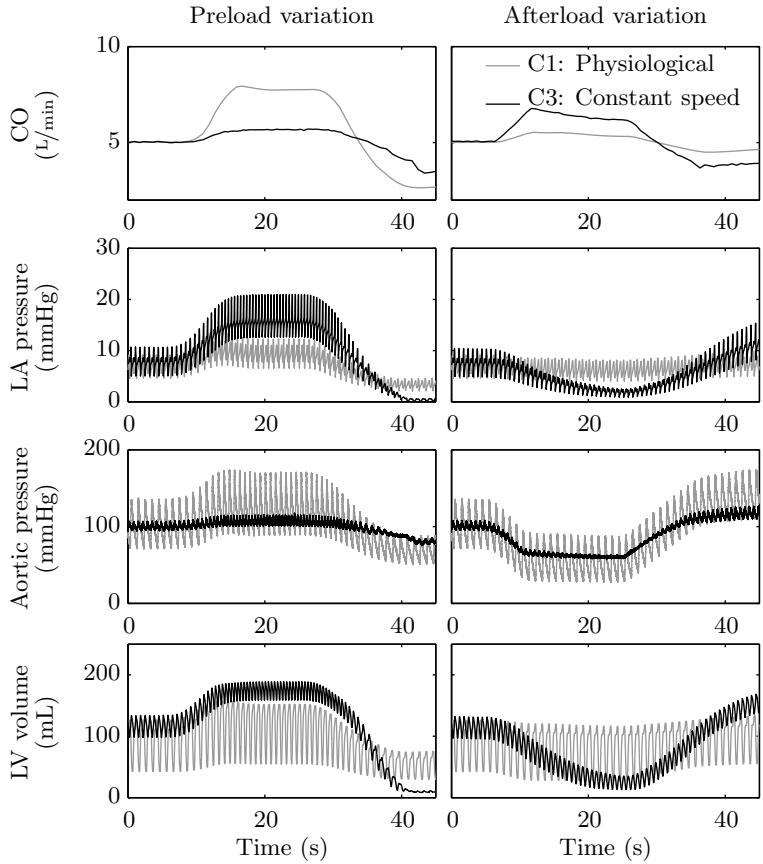

Figure 4.7: Comparison between the physiological circulation without VAD support and the pathological circulation supported with a VAD operated at a constant pump speed.

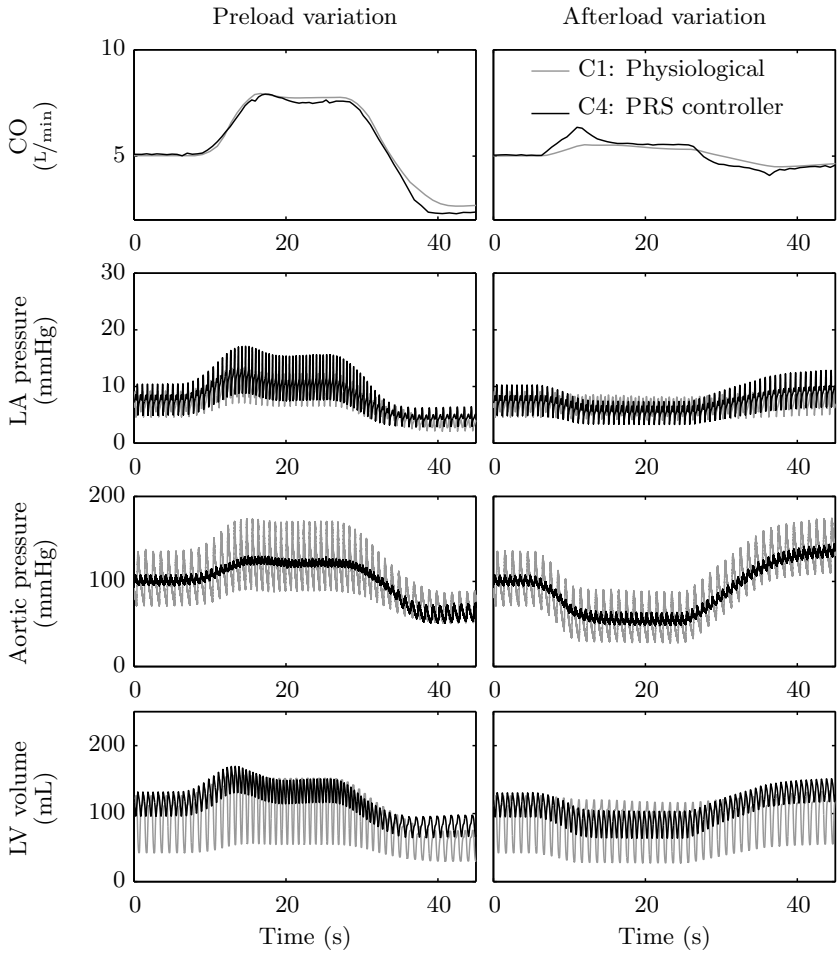

Figure 4.8: Comparison between the physiological circulation without VAD support and the pathological circulation supported with a VAD controlled by the PRS controller.

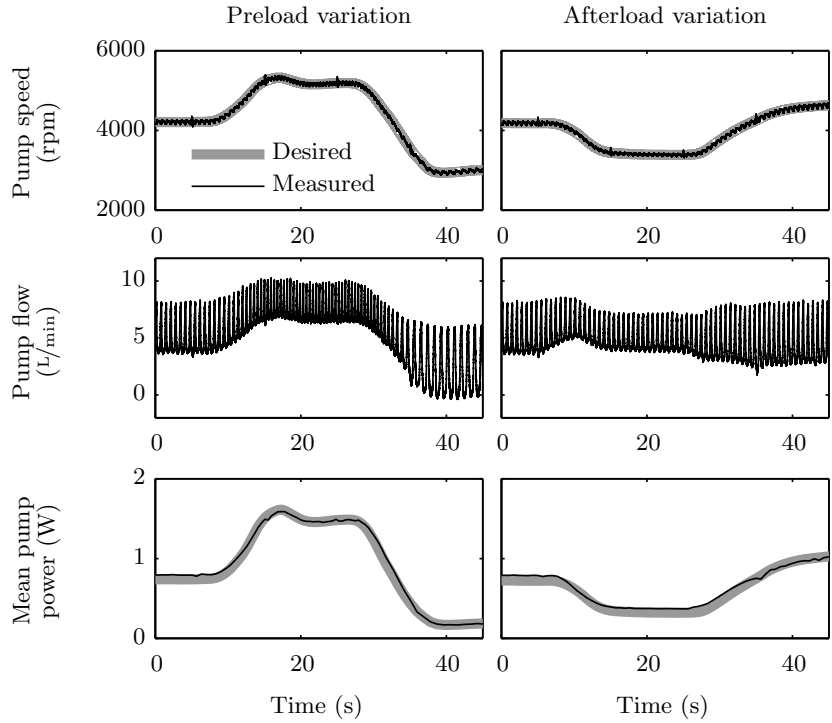

Figure 4.9: VAD signals for the experiments with the nominal PRS controller (C4).

Figure 4.8 contrasts the configurations C1 and C4. Clearly, the PRS controller behaves very similarly to the physiological circulation. All four signals stay within a physiological range, and under- or overpumping is effectively prevented as the LA pressure and the LV volume show. Figure 4.9 shows the VAD signals for C4. The desired pump power varies strongly during both experiments. By feeding the desired pump power into the PPLUT, the desired pump speed is calculated, which in turn is tracked by the pump speed controller. The pump speed tracking RMS error is 27.3 rpm. The actual pump power does not track the desired power accurately, which can be explained by the simplifying assumptions made for the derivation of the PPLUT. The pump power tracking RMS error is 0.05 W.

4.3.2 Sensitivity analysis of the PRS controller

Figures 4.10 and 4.11 show the CO and the EDV for the configurations C4, C5, and C6. In both figures, the thick gray lines represent C4, i.e., the nominal PRS controller. The dashed and the dotted lines represent the PRS controller with varied PRSW parameters. Since the CO autoregulation of the circulation model is inactive during the preload variation experiment and active during the afterload experiment, the CO varies less in the latter than in the former. Clearly, the qualitative behavior of the controller is not disturbed by the parameter variations, but the CO and the EDV are shifted. Table 4.2 lists the maximum deviation of the CO and the EDV from the nominal PRS controller for both parameter variations. The maximum overall CO deviation is less than 1.5 $^{\mathrm{L}}/_{\mathrm{min}}$, while the maximum overall EDV deviation is less than 42 mL.
Figure 4.11 additionally shows the influence of the simplified HR and EDV detection algorithm (C8) on the performance of the PRS controller. Since the simplified algorithm assumes a constant HR of 90 bpm, the controller performs very similarly to the nominal controller when the actual HR is 90 bpm. When the actual HR is higher, the simplified algorithm yields a slightly decreased CO and a slightly increased EDV and vice versa.
Figure 4.12 shows the influence of the contractility of the pathological LV on the performance of the PRS controller. This analysis is performed because the CO is determined by the combined hydraulic power of the VAD and the LV, and it is common that the contractility of the pathological LV changes due to physical activity or recovery. Clearly, the influence of the

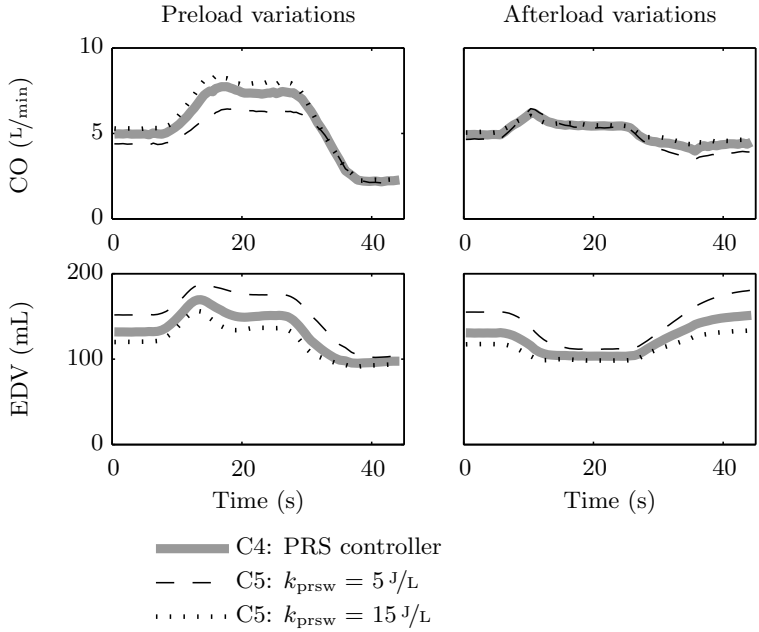

Figure 4.10: Influence of changes in k_{prsw}(C5) on the performance of the PRS controller. The figure shows how the CO and the EDV change when the controller gain is changed from its nominal value (10 J/L).

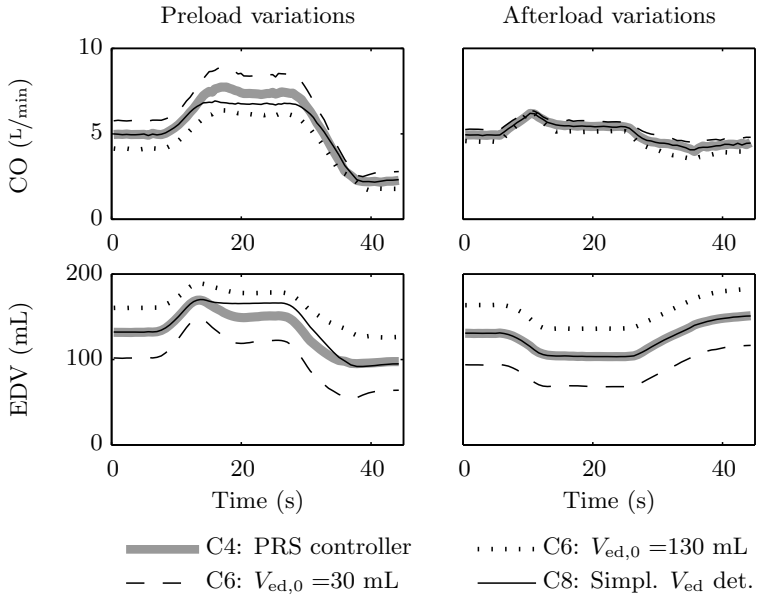

Figure 4.11: Influence of changes in $V_{ed,0}$ (C6) and influence of the simplified HR and detection algorithm (C8) on the performance of the PRS controller. The figure shows how the CO and the EDV change when the controller setpoint is changed from its nominal value (80 mL).

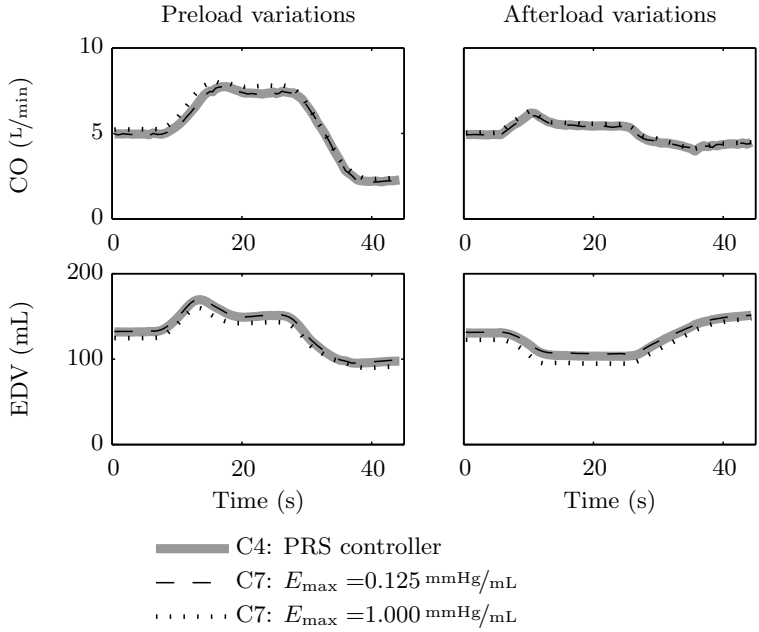

Figure 4.12: Influence of changes in E_{max} (C7) on the performance of the PRS controller. The figure shows how the CO and the EDV change when the contractility of the pathological LV changes from its nominal value (0.25 $^{mmHg}/_{mL}$).

Table 4.2: Maximum deviation of the CO and the EDV for changed PRS controller parameters compared with the nominal PRS controller (C4)

	Preload variation		**Afterlaod variation**	
	ΔCO [L/min]	**ΔV_{ed}** [mL]	**ΔCO** [L/min]	**ΔV_{ed}** [mL]
C5: $k_{\mathrm{prsw}} = 5\,\mathrm{J/L}$	-1.46	29.61	-0.62	29.49
C5: $k_{\mathrm{prsw}} = 15\,\mathrm{J/L}$	0.86	-18.47	0.35	-17.69
C6: $V_{\mathrm{ed},0} = 30\,\mathrm{mL}$	1.22	-41.54	0.45	-38.34
C6: $V_{\mathrm{ed},0} = 130\,\mathrm{mL}$	-1.40	40.10	-0.62	33.58

LV contractility is small. Even a fourfold increase of the LV contractility increases the CO by less than $0.8\,\mathrm{L/min}$.

Figure 4.13 shows how white noise and an increased sampling time influence the CO and the EDV. This influence is measured by the RMS deviation between the experiments with the nominal controller (C4) and the experiments with the disturbed LV volume measurement (C9). The RMS value is calculated over the preload and the afterload variation experiments. The lower left-hand corner represents the nominal condition with no noise and a sampling time of 10 ms. Both noise and increased sampling time influence the CO and the EDV, but the RMS deviation stays below $0.21\,\mathrm{L/min}$ and 3 mL, respectively. The qualitative behavior of the controller is preserved.

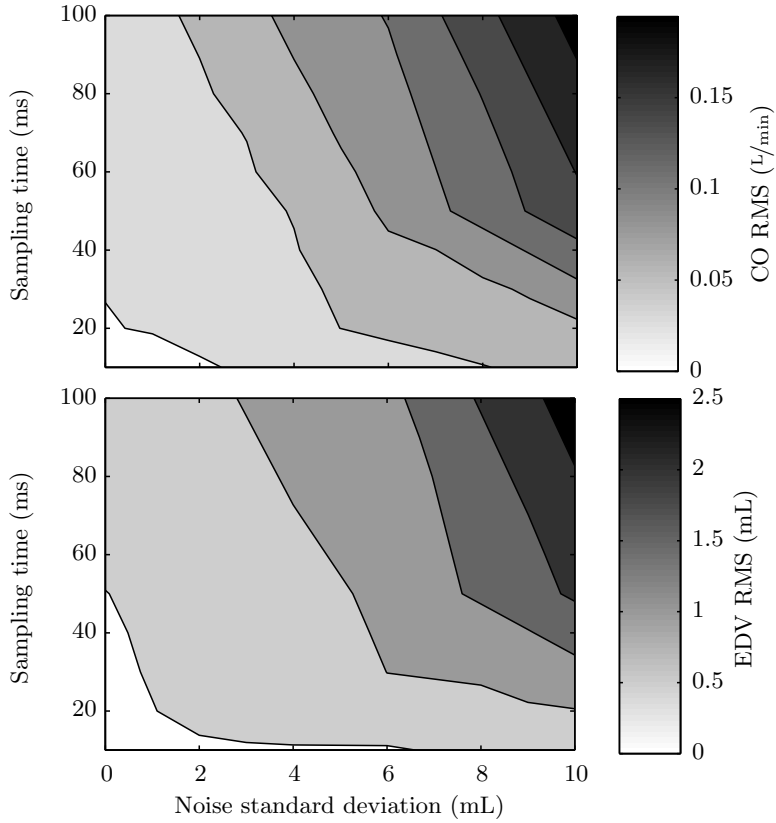

Figure 4.13: Influence of a disturbed LV volume "measurement"(C9) on the performance of the PRS controller. The panels show the RMS deviation of the CO and the EDV between the PRS controller with a perfect LV volume measurement and with a disturbed LV volume measurement.

4.4 Discussion

The experimental results show that the physiological control algorithm for VADs presented adapts the CO very similarly to the native heart, i.e., it shows a high sensitivity toward preload changes and a low sensitivity toward afterload changes. The pump speed adaptation is fast and keeps the LV volume in a safe range, and thus effectively prevents overpumping as well as underpumping. The PRS controller computes the desired pump speed based on the measured LV volume via the desired hydraulic pump power. The hydraulic pump power is only computed and used within the PRS controller and the detour via this auxiliary signal is taken for two reasons: First, it allows a virtual PRSW to be used with the physiologically interpretable parameters k_{prsw} and $V_{\mathrm{ed},0}$, and second, it helps to compensate the nonlinearities in the pump speed to pump flow behavior (see Figure 4.4). In addition, the hydraulic pump power could be used for diagnostic purposes.

The structure of our PRS controller is very simple, and only two parameters need to be defined, namely k_{prsw} and $V_{\mathrm{ed},0}$. The latter represents the volume at which the desired hydraulic power of the pump is zero, whereas k_{prsw} represents the gain of the hydraulic pump power over the measured $V_{\mathrm{ed}}(t)$. The values for these two parameters can be set as desired in order to adapt the pump flow to the patient's need. Chapter 5 describes a stability analysis of the PRS controller and provides an upper limit for k_{prsw}. The constant speed operation of VADs, which is the current clinical practice, is represented by $k_{\mathrm{prsw}} = 0\,\mathrm{J/L}$. Clearly, the PRS controller could be used as the low-level controller in a hierarchical control system. A high-level control system could then influence the k_{prsw} of the PRS controller while maintaining the safe operation provided by the PRS controller. Such a high-level controller could be based on an additional measurement, e.g. a measurement of the patient movement (acceleration sensor), the blood oxygen concentration, or the aortic pressure.

Most of the physiological VAD control systems presented in the literature do not use flow-rate, blood pressure, or volume sensors, but are based on intrinsic pump parameters such as the motor current and the pump speed. These parameters are easily obtainable, and using them in a VAD controller is indispensable either for control purposes or at least for fault detection. The reason for sensors typically not being used is their lack of

long-term stability when implanted in the human body [17]. However, a few controllers presented in the literature require an explicit measurement of either pressure [16, 72] or flow [15]. We are currently evaluating several measurement techniques in order to develop a robust, long-term stable LV volume sensor. In addition, it can be argued that the sole measurement of intrinsic pump parameters is not very robust, since the motor current can be disturbed by a thrombus inside the pump, for instance. In case the PRS controller is implemented on a clinical VAD in the future, estimators for flow and pressure would be implemented as well, be it for monitoring or fault detection purposes.

The parameter sensitivity analysis of k_{prsw} and $V_{\mathrm{ed},0}$ shows that the physiological behavior of the PRS controller was not achieved by fine-tuning of the controller parameters, but by an inherent physiological control structure. Both CO and V_{ed} are influenced by the parameter choice, but the qualitative behavior of the PRS controller is preserved. Additionally, both controller parameters are physiologically motivated, i.e., the range of reasonable values is limited. The results of the LV volume measurement analysis show that in the current structure, the PRS controller is very robust toward noise and a reduced sampling frequency. Current LV volume sensors typically do not suffer from white noise, but from other types of disturbances like interference in case of admittance catheters. Such disturbances are not investigated in the current thesis, but will have to be investigated once an LV volume sensor is available. For patients with an irregular HR, an alternative (and simpler) HR and EDV detection algorithm is proposed. This algorithm is more robust than the normal HR and EDV detection algorithm and yields similar results. Alternatively, previously developed algorithms for an HR detection could be used, which are robust toward an irregular HR [24].

The CO results from the combined hydraulic power of the PRS-controlled VAD and the LV. By simulating an inferior vena cava occlusion maneuver with the numerical circulation model in the physiological (C1) and the pathological (C2) condition, the slopes of the PRSW were identified. The sum of the slopes of the PRSW of the pathological LV (2.4 $^{\mathrm{J}}/_{\mathrm{L}}$) and the PRS controller (10 $^{\mathrm{J}}/_{\mathrm{L}}$) is almost equal to the slope of the PRSW of the physiological LV (12.9 $^{\mathrm{J}}/_{\mathrm{L}}$), which explains the very similar experimental results.

In clinical practice, VAD patients are exposed to various clinical conditions. Hypovolemia or hypertension are frequently observed conditions after the implantation of a turbodynamic VAD. Furthermore, arrhythmia conditions such as ventricular tachycardia or fibrillation may occur [79]. The performance of the PRS controller under such conditions has been investigated and is briefly discussed here. As expected, during hypovolemia, the pump speed is low such that suction does not occur, with the downside of a strongly reduced CO; during hypertension, the pump speed is high, such that the LA pressure is not strongly elevated, with the downside of maintaining an excessive arterial pressure. When ventricular fibrillation occurs, the low output of the RV is associated with a severe reduction of venous return to the left side of the heart, which in turn causes the PRS controller to markedly decrease the pump speed. As a consequence, the CO drops dramatically. These three examples illustrate the fact that the performance of the PRS controller may not be adequate in every clinical situation, although its action aims to imitate the native heart. It must be emphasized, though, that a VAD controller can only adapt the pump speed and is therefore not able to meet several requirements simultaneously: If for any reason venous return is pathologically low, any VAD controller is unable to keep the CO high and avoid suction at the same time; the VAD can only pump the blood that is available for pumping, otherwise suction occurs. Similarly, if the peripheral resistance is very high, a VAD controller is unable to keep the CO high and at the same time avoid hypertension. If any of these situations occurs, a VAD controller cannot resolve it, but must detect it and alarm. The treatment of the complication must then be conducted by the physician, trained medical personnel, or the patient.

In the current clinical practice, VADs are typically operated at a constant speed, which is chosen by the physician. The physiological controller presented in [15] has been tested in patients and has proven to yield improved hemodynamics compared to those obtained with a constant speed controller [80]. This controller uses an integral controller on the pump speed based on a measurement of the pump flow rate. The controller adapts the pump flow setpoint according to the measured HR and has additional features to avoid over- and underpumping. Furthermore, a sophisticated suction detection system has been implemented [65]. This controller and the PRS controller presented in the current thesis are based on the same

ideas but are implemented differently. In comparison, the PRS controller is simpler and yields a faster response. As a drawback, the measurement of the LV volume is not state-of-the-art as is the measurement of the pump flow.

4.5 Conclusion

The PRS controller yields a fast, physiological, and safe adaptation of the pump speed of a turbodynamic VAD to the patient's requirement. If a reliable LV volume sensor can be combined with the PRS controller, the pump flow is automatically adapted to the volume load of the patient's native heart. Hereby, a true physiological adaption of the pump can be achieved. This may markedly improve the functional capacity, safety, and quality of life of patients supported by a VAD. As a result, VADs can become even more attractive for use as permanent, lifelong support devices and as a viable alternative to heart transplantation.

Appendix B

The PPLUT was derived by conducting experiments on the mock circulation. Four experiments were conducted, each with a different fixed afterload and a slow pump speed ramp with the circulation model in the pathological condition. The fixed values for the systemic arterial resistance were $R_{\mathrm{sa}} = \{0.5, 1, 1.5, 2\}\,{}^{\mathrm{mmHg \cdot s}}/_{\mathrm{mL}}$, and the pump speed was ramped up from a zero-flow speed to a speed causing ventricular suction. The hydraulic pump power $P_p(t)$ was calculated by

$$P_p(t) = \big(p_{\mathrm{ao}}(t) - p_{\mathrm{lv}}(t)\big) \cdot q_{\mathrm{bp}}(t) \tag{4.3}$$

where $p_{\mathrm{ao}}(t)$ is the aortic pressure, $p_{\mathrm{lv}}(t)$ is the LV pressure, and $q_{\mathrm{bp}}(t)$ is the pump flow rate. For each experiment, the mean hydraulic pump power over every 20^{th} heartbeat was calculated and plotted versus the pump speed. Figure 4.4 shows the result of this analysis. Clearly, the power is mainly determined by the pump speed rather than the afterload. A least-squares fit of a third-order polynomial was chosen as the PPLUT. The polynomial was limited to a range of 0 to 2.5 W, which is also depicted in Figure 4.4. In order to analyze the sensitivity of the PRS controller to errors in the PPLUT, the preload and afterload variation experiments were repeated with the PPLUT shifted by ± 0.5 W. The maximum deviation of the CO compared to the nominal PRS controller is less than $0.80\,{}^{\mathrm{L}}/_{\mathrm{min}}$; the maximum deviation of the EDV is less than 35 mL. Thus, the PPLUT is considered accurate enough for the PRS controller presented in the current thesis.

Chapter 5

Stability Analysis of the PRS Controller

This chapter describes a stability analysis of the PRS controller using a numerical model of the VAD and the human circulation. Due to the beating of the heart, the equilibria of this system are periodic solutions. Compared to fixed points, the stability of periodic solutions is more difficult to analyze. Therefore, a linear, discrete-time model is derived, which maps the state and input at end diastole to the state at end diastole in the next heartbeat. Finite differences are used to derive this mapping from the nonlinear, continuous-time model of the VAD and the circulation. In order to take into account the fact that the physiology differs from patient to patient, the discrete-time model is computed for 1000 parameter combinations in a Monte Carlo experiment. The PRS controller is implemented by a discrete-time proportional control law. The open loop gain is calculated by a series connection of the PRS controller and the discrete-time model of the VAD and the circulation. The Nyquist diagram of the loop gain shows that the PRS controller with the nominal controller gain is stable for all parameter combinations. This result holds for the advanced and the simplified HR and EDV detection algorithm with and without a delay. The minimum gain margin with the simplified algorithm is 3.35; the minimum gain margin with the advanced algorithm is 2.99. With both algorithms, the phase margin is infinity. In conclusion, if the PRS controller is used with the simplified HR and EDV detection algorithm, with $k_{\mathrm{prsw}} \leq 15\,{}^{\mathrm{J}}/_{\mathrm{L}}$, and with an assumed HR of 90 bpm, the closed loop system is stable in all patients.

The content of this chapter has not been published elsewhere.

5.1 Introduction

The introduction of feedback in control systems is powerful and dangerous at the same time. Feedback is necessary to compensate for unknown disturbances but it can make control systems unstable [44]. Because instability leads to a malfunctioning of the control system or even a destruction of the plant, it is very important that stability can be guaranteed, all the more so for the PRS controller, which is built into a VAD that is implanted into a patient.
The PRS controller is introduced and described in Chapter 4. It is an automatic control algorithm designed to change the pump speed of a VAD based on the EDV of the LV. The controller thereby adapts the pump flow to the requirements of the patient while preventing dangerous situations like ventricular suction. The PRS controller consists of three stages: The first stage extracts the EDV and the HR from the LV volume signal. The second state imitates the PRSW by a proportional gain from the EDV to the desired hydraulic pump power. The third stage computes the desired pump speed from the desired hydraulic pump power using the PPLUT. The investigation in the current chapter is conducted with the advanced and the simplified HR and EDV detection algorithm, i.e., with the input being the actual HR or a constant value of 90 bpm, respectively.
Due to the heartbeat, the equilibria of the system analyzed are periodic solutions. Obviously, compared to fixed points, the stability of periodic solutions is more difficult to analyze. One tool to analyze the stability of periodic solutions for autonomous systems is the Poincaré map [45]: First, a Poincaré section is defined, which is a n–1-dimensional subspace transversal to the periodic solution. The Poincaré map then represents the discrete mapping from crossing position to crossing position in the (n–1-dimensional) Poincaré section. However, due to the time-varying elastance, the system analyzed in the current section is nonautonomous. For nonautonomous systems, an additional state variable can be introduced, which is periodical and describes the progress within the period. In this case, the Poincaré section can be defined by a fixed value of the additional state variable, and the Poincaré map then describes the n-dimensional mapping of the state from period to period. In the current analysis, the mapping from end diastole to end diastole is considered, because the EDV is used as

the input of the PRS controller. If the discrete-time mapping additionally has an input, it is called a controlled Poincaré map [81].
Due to the valves and the flow resistance in the VAD, the system analyzed in the current chapter is nonlinear. Consequently, the controlled Poincaré map is nonlinear as well. But whereas the stability of a fixed point of a linear system is easy to evaluate, the same is difficult for a nonlinear system [45]. The most common approach to analyze the stability of a nonlinear fixed point is to linearize the system around this point and to check the eigenvalues of the state propagation matrix. If all eigenvalues have a magnitude smaller than one, the linearized system is asymptotically stable. Close to the fixed point around which the system is linearized, the stability properties of the linearized and the nonlinear systems agree. However, the global stability of a nonlinear system cannot be evaluated using its linearized version. In order to obtain a more global notion of stability, the nonlinear system can be linearized around various equilibria which result from different model parameters or a different model input. If each linearized system is stable, the nonlinear system can be assumed to be stable as well. However, the stability of the nonlinear system cannot be guaranteed by this approach. In the current chapter, finite differences are used to derive a linearized controlled Poincaré map for various equilibria and parameter combinations describing the human circulation. In total, the map is derived with 1000 parameter combinations, where the parameters are defined by a Monte Carlo simulation. Stability is then investigated using the Nyquist criterion.

5.2 Methods

This section is subdivided into three parts. Section 5.2.1 describes the derivation of the nonlinear, continuous-time model of the human circulation and the VAD. Section 5.2.2 describes how the controlled Poincaré map is derived from the continuous-time model. Section 5.2.3 describes how the model parameters are varied to represent different physiologies and how stability is investigated for each of the 1000 parameter combinations.

5.2.1 Continuous-time model

Circulation model

Compared to the numerical model depicted in Figure 2.3, the model used for the current investigation has been simplified and reduced: The atrium is non beating, the valve flows are static functions, and the end-systolic as well as the end-diastolic elastances are constant. In addition, the circulation is only modeled from the pulmonary to the systemic veins, i.e., the right side of the heart is not included in the model. This last simplification is justified by the slow dynamics of the systemic veins, owing to their high compliance, and by the autoregulation of the venous tone. The pressures in the systemic and the pulmonary veins thus are assumed to be constant and independent of the VAD.
The circulation is represented by four state variables, namely the LA volume $V_{\mathrm{la}}(t)$, the LV volume $V_{\mathrm{lv}}(t)$, the aortic volume $V_{\mathrm{ao}}(t)$, and the arterial resistance $\rho_b(t)$ adapted by the baroreflex mechanism. The input to this part of the model is the flow rate through the VAD $q_{\mathrm{vad}}(t)$. The resulting model is given by

$$\frac{\mathrm{d}}{\mathrm{d}t}\begin{pmatrix} V_{\mathrm{la}}(t) \\ V_{\mathrm{lv}}(t) \\ V_{\mathrm{ao}}(t) \\ \rho_b(t) \end{pmatrix} = \begin{pmatrix} q_{\mathrm{pv}}(t) - q_{\mathrm{mv}}(t) \\ q_{\mathrm{mv}}(t) - q_{\mathrm{av}}(t) - q_{\mathrm{vad}}(t) \\ q_{\mathrm{av}}(t) + q_{\mathrm{vad}}(t) - q_{\mathrm{sa}}(t) \\ \frac{1}{\tau_b}\Big(- \rho_b(t) - k_b\big(p_{\mathrm{ao}}(t) - p_{\mathrm{ao},0}\big)\Big) \end{pmatrix}. \tag{5.1}$$

The flows $q_i(t)$ are computed by

$$q_{\mathrm{pv}}(t) = \frac{p_{\mathrm{pv}} - p_{\mathrm{la}}(t)}{R_{\mathrm{pv}}} \tag{5.2}$$

$$q_{\mathrm{mv}}(t) = \begin{cases} \frac{p_{\mathrm{la}}(t) - p_{\mathrm{lv}}(t)}{R_{\mathrm{mv}}} & \text{if } p_{\mathrm{la}}(t) > p_{\mathrm{lv}}(t) \\ 0 & \text{else} \end{cases} \tag{5.3}$$

$$q_{\mathrm{av}}(t) = \begin{cases} \frac{p_{\mathrm{lv}}(t) - p_{\mathrm{ao}}(t)}{R_{\mathrm{av}}} & \text{if } p_{\mathrm{lv}}(t) > p_{\mathrm{ao}}(t) \\ 0 & \text{else} \end{cases} \tag{5.4}$$

$$q_{\mathrm{sa}}(t) = \frac{p_{\mathrm{ao}}(t) - p_{\mathrm{sv}}}{R_{\mathrm{sa}}(t)}, \tag{5.5}$$

where the variables $p_i(t)$ denote pressures and the parameters R_i denote flow resistances. The resistances in the pulmonary veins, the mitral valve, and the aortic valve are modeled as being constant; the resistance in the systemic arteries depends on the baroreflex mechanism and is computed by

$$R_{\mathrm{sa}}(t) = R_{\mathrm{sa},0} + \rho_b(t), \tag{5.6}$$

where $R_{\mathrm{sa},0}$ is the nominal resistance. The baroreflex mechanism is modeled as a first-order low-pass filter with the deviation of $p_{\mathrm{ao}}(t)$ from its setpoint $p_{\mathrm{ao},0}$ as input and the resistance $\rho_b(t)$ as output. The parameters τ_b and k_b are the time constant and the gain, respectively.
The pressures $p_i(t)$ are computed by

$$p_{\mathrm{la}}(t) = \frac{V_{\mathrm{la}}(t)}{C_{\mathrm{la}}} \tag{5.7}$$

$$p_{\mathrm{lv}}(t) = \frac{V_{\mathrm{lv}}(t)}{C_{\mathrm{lv}}(t)} \tag{5.8}$$

$$p_{\mathrm{ao}}(t) = \frac{V_{\mathrm{ao}}(t)}{C_{\mathrm{ao}}}, \tag{5.9}$$

where the parameters C_i denote the vessel compliances. The atrial and the aortic compliances are modeled as being constant; the ventricular compli-

ance is modeled by a time-varying elastance function:

$$C_{\mathrm{lv}}(t_n) = \begin{cases} \frac{1}{(E_{\mathrm{sys}} - E_{\mathrm{dia}})\sin(3t_n\pi) + E_{\mathrm{dia}}} & \text{if } t_n < \frac{1}{3} \\ \frac{1}{E_{\mathrm{dia}}} & \text{else} \end{cases} \tag{5.10}$$

where E_{dia} is the diastolic elastance, E_{sys} is the systolic elastance, and $t_n \in [0, 1)$ is the normalized time in the cardiac cycle.

VAD model and PRS controller

This section describes the derivation of the VAD model and the PRS controller required for the stability analysis. Figure 5.1a) shows the starting point for this derivation consisting of a nonlinear model for the VAD flow described by (2.1), a model for the controlled pump speed dynamics, and the detailed PRS controller as shown in Figure 4.2. Figure 5.1a) shows how these three parts are connected, whereas Figure 5.1b) shows how the system is modified to be used for the stability analysis. The following three modifications are made: First, the controlled pump speed dynamics are neglected. The time constant of these dynamics is approximately 0.05 s. Compared to the low-pass filter in the PRS controller with a time constant of 1 s, these dynamics are much faster. The value of $N(t)$ thus is assumed to be identical to that of $N_{\mathrm{des}}(t)$. Second, the PPLUT and the low-pass filter are moved from the PRS controller to the VAD model. Finally, the PRS controller is converted to a proportional controller, such that classical control theory can be applied.
The resulting VAD model is given by

$$\frac{\mathrm{d}}{\mathrm{d}t}\begin{pmatrix} v_{\mathrm{filt}}(t) \\ q_{\mathrm{vad}}(t) \end{pmatrix} = \begin{pmatrix} \frac{1}{\tau_{\mathrm{lp}}}\big(-v_{\mathrm{filt}}(t) + v(t)\big) \\ \frac{1}{L_{\mathrm{vad}}}\big(p_{\mathrm{lv}}(t) - p_{\mathrm{ao}}(t) + p_{\mathrm{rot}}(t) - p_{\mathrm{res}}(t)\big) \end{pmatrix}, \tag{5.11}$$

where $v(t)$ and $v_{\mathrm{filt}}(t)$ represent the input from the PRS controller and its filtered version, respectively, τ_{lp} is the time constant of the low-pass filter, and L_{vad} is the inertance of the flow. The pressure generated by the rotor $p_{\mathrm{rot}}(t)$ and the pressure drop due to the resistance $p_{\mathrm{res}}(t)$ are computed by

$$p_{\mathrm{rot}}(t) = k_{\mathrm{vad}} \cdot \mathrm{PPLUT}\big(v_{\mathrm{filt}}(t)\big)^2 \tag{5.12}$$

$$p_{\mathrm{res}}(t) = R_l \cdot q_{\mathrm{vad}}(t) + R_q \cdot q_{\mathrm{vad}}(t) \cdot |q_{\mathrm{vad}}(t)|. \tag{5.13}$$

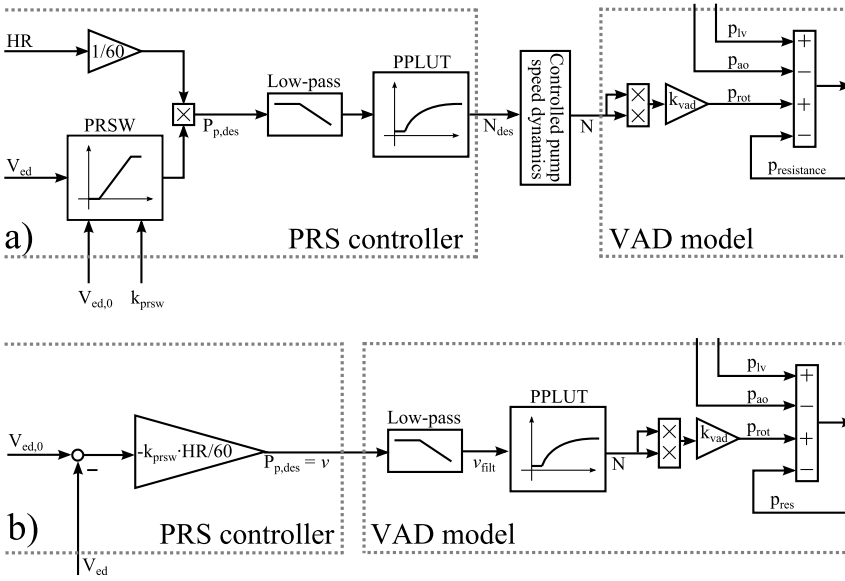

Figure 5.1: Derivation of the modified model of the PRS controller and the VAD: Panel a) shows the PRS controller as depicted in Figure 4.2, the controlled pump speed dynamics, and the model of the VAD as described by (2.1). The HR and EDV detection is introduced later. Panel b) shows the modified model. The controlled pump speed dynamics are neglected due to their fast dynamics, and the PPLUT as well as the low pass filter are moved from the PRS controller to the VAD model. The PRS controller is represented as a classical proportional controller.

Figure 5.1b) shows the PRS controller as it is used for the stability analysis, and it can be described by

$$v(t) = -k_{\text{prsw}} \cdot \frac{\text{HR}}{60} \cdot \big(V_{\text{ed},0} - V_{\text{ed}}(t)\big) \tag{5.14}$$

Combined model

Figure 5.2 shows the controller and the plant derived in this section. The nonlinear, time-varying plant is derived by combining (5.1) and (5.11) and

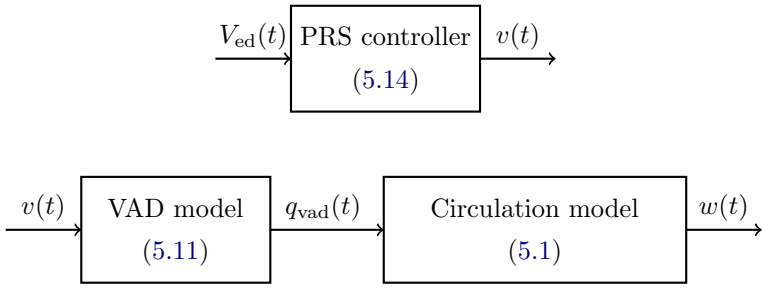

Figure 5.2: The nonlinear, continuous-time models of the controller and the plant. The plant consists of the VAD model and the circulation model.

can be described by

$$\begin{aligned} \frac{\mathrm{d}z(t)}{\mathrm{d}t} &= f\big(z(t), v(t), t\big), \\ w(t) &= g\big(z(t)\big) \end{aligned} \tag{5.15}$$

where $z(t) \in \mathbb{R}^6$ is the state, $v(t) = P_{\mathrm{p,des}}(t) \in \mathbb{R}$ is the input to the VAD model, and $w(t) = V_{\mathrm{lv}}(t) \in \mathbb{R}$ is the output of the circulation model. The PRS controller is described by (5.14). Since the HR and EDV detection algorithm has been neglected thus far, the feedback loop cannot be closed, and the controller as well as the plant are linearized and discretized separately.

5.2.2 Controlled Poincaré map

Circulation and VAD model

This section describes the derivation of the linearized controlled Poincaré map from the nonlinear, continuous-time model (5.15). At the end, the map will show the form

$$\begin{aligned} x_{k+1} &= Ax_k + bu_k \\ y_k &= cx_k, \end{aligned} \tag{5.16}$$

where $x \in \mathbb{R}^6$ is the state, $u \in \mathbb{R}$ is the input, and $y \in \mathbb{R}$ is the output. The values x_k, u_k, and y_k denote deviations from the equilibrium periodic solution at end diastole of the k^{th} heartbeat, and the mapping (5.16) describes

how these deviations propagate from heartbeat to heartbeat. End diastole is chosen because the input to the PRS controller is the EDV. Therefore, the vector c in the output equation of (5.16) is $c = \begin{bmatrix} 0 & 1 & 0 & 0 & 0 & 0 \end{bmatrix}$.
The matrix A and the vector b are computed using finite differences: First, the model (5.15) is simulated with a constant input v_e until the equilibrium periodic solution is reached, and the equilibrium state z_e is extracted at end diastole. Then, one after the other, each state variable is shifted by $\delta = 10^{-4}$ from the z_e and the continuous-time model is simulated for one heartbeat. For each of the six simulations, a final state $z_{f,i}$ ($i \in \{1, 2, 3, 4, 5, 6\}$) is reached. The i^{th} column a_i of the matrix A is then computed by $a_i = \frac{z_{f,i} - z_e}{\delta}$. The vector b is computed analogously by simulating the model with the input $v = v_e + \delta$. After one heartbeat, the final state $z_{f,u}$ is reached and the vector b is computed by $b = \frac{z_{f,u} - z_e}{\delta}$.

PRS controller

The linearized and discretized version of the PRS controller is given by

$$u_k = k_{\text{prsw}} \cdot \frac{\text{HR}}{60} \cdot y_k. \tag{5.17}$$

Because u_k and y_k are deviations from the equilibrium, the setpoint $V_{\text{ed},0}$ drops out.

Combined model

Figure 5.3 shows the combined, linear, discrete-time model used for the stability analysis.

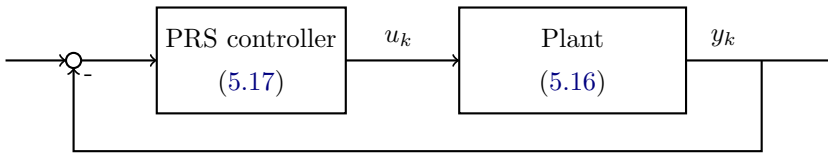

Figure 5.3: Discrete-time closed loop system consisting of the PRS controller and the plant.

5.2.3 Stability analysis of the closed loop system

The stability of the closed loop system is analyzed using the Nyquist criterion [44], which provides information about the stability of the closed loop system from analyzing the open loop system only. In addition, phase and gain margins can be computed, which provide information about the robustness, for instance toward modeling errors. The loop gain used for the Nyquist analysis is obtained by a series connection of the controller (5.17) and the plant (5.16) as shown in Figure 5.3. Both versions of the HR and EDV detection algorithm introduce a certain delay, which varies from heartbeat to heartbeat. Therefore, the Nyquist diagram is analyzed without delay as well as with a delay of 1 s added to the loop gain. The additional delay is introduced in the Nyquist diagram by adding $\varphi_d = \omega \cdot T_d$ to the phase of the loop gain, where ω is the frequency and $T_d = 1\,\mathrm{s}$ is the delay.

In order to obtain a global notion of stability for the PRS controller, the system (5.16) is linearized around different equilibria, i.e., the constant input v_e to reach steady state is varied. In addition, seven model parameters are varied to represent a wide range of patients with different physiologies. Table 5.1 lists all values that are varied for the linearization as well as their lower and upper limits, whereas Table 5.2 lists all parameters that were assumed to be constant. The values or limits for all parameters of the circulation are chosen based on the experience gained with the detailed model of the circulation as described in Section 2.2.3. The values of the VAD model parameters are close approximations of the values provided in Section 2.2.4.

Table 5.1: Varied parameters

Parameter	Unit	Minimum	Maximum
v_e	W	0.5	2.5
p_{pv}	mmHg	5	20
$R_{\mathrm{sa},0}$	$\mathrm{mmHg \cdot s/mL}$	0.5	1.5
E_{sys}	$\mathrm{mmHg/mL}$	1	4
HR	bpm	50	150
C_{ao}	$\mathrm{mL/mmHg}$	0.5	2
τ_b	s	0.5	2
k_b	$\mathrm{s/mL}$	0.005	0.02

Table 5.2: Constant parameters

Parameter	Unit	Value
C_{la}	$^{\mathrm{mL}}/_{\mathrm{mmHg}}$	10
E_{dia}	$^{\mathrm{mmHg}}/_{\mathrm{mL}}$	0.1
R_{mv}	$^{\mathrm{mmHg \cdot s}}/_{\mathrm{mL}}$	0.01
R_{av}	$^{\mathrm{mmHg \cdot s}}/_{\mathrm{mL}}$	0.01
R_{pv}	$^{\mathrm{mmHg \cdot s}}/_{\mathrm{mL}}$	0.01
p_{sv}	mmHg	0
k_{vad}	$^{\mathrm{mmHg}}/_{\mathrm{rpm}^2}$	$6 \cdot 10^{-6}$
L_{vad}	$^{\mathrm{mmHg \cdot s}^2}/_{\mathrm{mL}}$	0.04
R_l	$^{\mathrm{mmHg \cdot s}}/_{\mathrm{mL}}$	0.1
R_q	$^{\mathrm{mmHg \cdot s}^2}/_{\mathrm{mL}^2}$	0.004
τ_{lp}	s	1

Because eight parameters are varied, an exhaustive brute force analysis is not feasible. The parameters are therefore varied using the Monte Carlo method. One thousand parameter combinations are generated, whereby each parameter is randomly selected from a uniform distribution between its lower and upper limits. The computation of the 1000 models in MATLAB requires approximately 5 h on a PC with a dual-core CPU with 2 GHz.

5.3 Results

The panels (a), (b), and (c) of Figure 5.4 show the results of the stability analysis with the nominal controller gain and the simplified HR and EDV detection algorithm, i.e., $k_{\text{prsw}} = 10\,{}^{\text{J}}/_{\text{L}}$ and $\text{HR} = 90\,\text{bpm}$ are used for the PRS controller (5.17). Panel (a) shows the Nyquist diagram of the loop gain without delay for all 1000 parameter combinations. Clearly, the closed loop system is always stable with a minimum gain margin of 5.04 and an infinite phase margin. Panel (b) shows the poles of the complementary sensitivity without delay. Panel (c) shows the Nyquist diagrams of the loop gain with an additional delay of 1 s. The minimum gain margin reduces to 3.35, but the closed loop system is still stable for all parameter combinations.
The panels (d), (e), and (f) of Figure 5.4 show the results of the stability analysis with the nominal controller gain and the advanced HR and EDV detection algorithm, i.e., the HR used for the calculation of the model (5.16) is also used in the PRS controller (5.17). Panel (d) shows the Nyquist diagram of the loop gain without delay for all 1000 parameter combinations. Clearly, the closed loop system is always stable with a minimum gain margin of 7.67 and an infinite phase margin. Panel (e) shows the poles of the closed loop system. Panel (f) shows the Nyquist diagrams of the loop gain with an additional delay of 1 s. Again, the minimum gain margin reduces to 2.99, but the closed loop system is still stable for all parameter combinations.

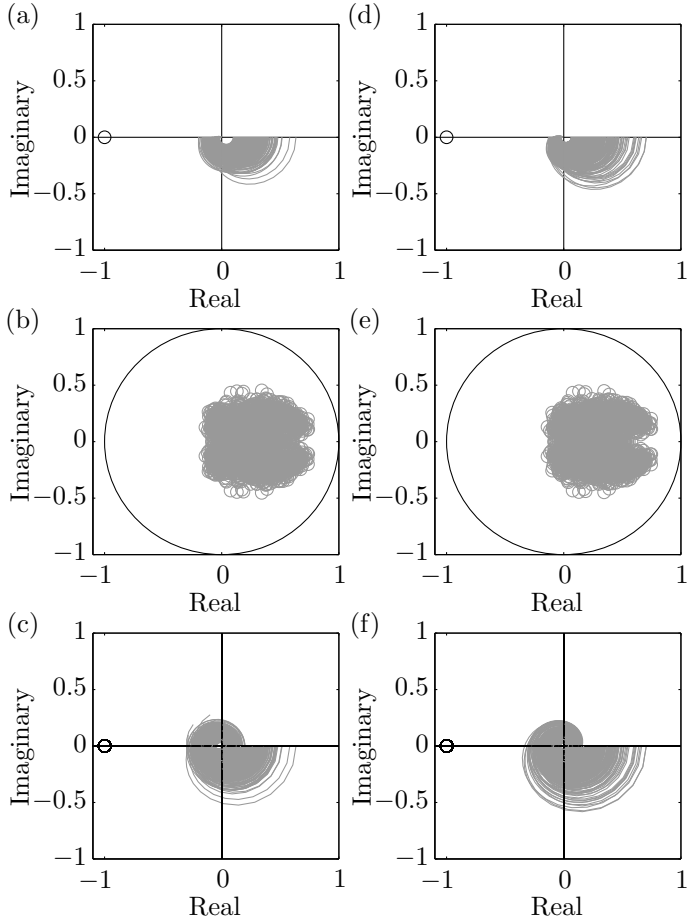

Figure 5.4: Results of the stability analysis for the PRS controller with the simplified HR and EDV detection algorithm in Panels (a), (b) and (c) as well as the advanced algorithm in Panels (d), (e), and (f). Panels (a) and (d) show the Nyquist diagram of the loop gain for all parameter combinations. The minimum gain margin is 5.04 and 7.67, respectively. Panels (b) and (e) show the poles of the complementary sensitivity for all parameter combinations. Panels (c) and (f) show the Nyquist diagram of the loop gain for all parameter combinations with an additional delay of 1 s added to the loop gain. The minimum gain margin reduces to 3.35 and 2.99, respectively.

5.4 Discussion

This chapter investigates the stability of the PRS controller. A linear, discrete-time model of the human circulation and the VAD is derived and stability is analyzed for 1000 randomly selected parameter combinations. The resulting closed loop system is stable for all combinations with a gain margin of at least 2.99 and an infinite phase margin.
For the current investigation, the HR and EDV detection algorithm has been neglected because the EDV is a state variable of the discrete-time model (5.16). However, depending on the implementation, the algorithm introduces a delay. In the current implementation of both versions of the HR and EDV detection algorithm, the delay can vary between a couple of milliseconds and approximately 1 s. Therefore, the Nyquist analysis is conducted without delay as well as with a delay of 1 s. As expected for a system with an infinite phase margin, the gain margin is reduced, but even with the delay taken into account, the stability is preserved.
The PRS controller was developed to imitate the healthy human physiology. The proportional control law is inspired by the PRSW [4], and the nominal controller gain $k_{\mathrm{prsw}} = 10\,\mathrm{J/L}$ is in the physiological range for men [78]. Therefore, it is not surprising that the PRS controller is stable for all parameter combinations. The PRSW is a result of the evolution and is stable in all humans. By closely imitating the PRSW, the PRS controller not only inherits its physiological response but also its stability property.
The high gain margin of the loop gain indicates great robustness, and the controller gain can even be increased above its nominal value of $k_{\mathrm{prsw}} = 10\,\mathrm{J/L}$. However, the analysis in Chapter 4 shows that the behavior of the PRS controller with the nominal gain is already close to that of the native heart at rest. Therefore, the maximum allowed controller gain is defined as $k_{\mathrm{prsw}} = 15\,\mathrm{J/L}$, which yields a very responsive PRS controller and still exhibits a gain margin of more than 2.2 for all parameter combinations and a delay in EDV detection of 1 s.
With the advanced HR and EDV detection algorithm, the gain of the PRS controller is linearly adapted with the HR. This implementation is physiologically motivated, since the PRSW calculates the stroke work per heartbeat, i.e., in order calculate the stroke power of the heart, the stroke work must be multiplied by the HR. From a control point of view, the multiplication of the controller gain by the HR can be viewed as gain

scheduling [45]. In order to preserve the stability property of a controller, gain scheduling is only allowed if the adaptation of the gain is significantly slower than the bandwidth of the controller. This property is not given for the HR and the PRS controller. Therefore, the validity of the stability analysis with the advanced HR and EDV detection is limited such that the further development of the PRS controller will be focused on the simplified HR and EDV detection.

Chapter 6

Conclusion and Outlook

6.1 Conclusion

The hybrid mock circulation has proven to be a valuable tool to test blood pumps. The setup works reliably and the results are highly repeatable. Its behavior is very close to physiological and the numerical implementation of the human circulation makes the mock circulation flexible and adaptable. Furthermore, the possibility to simulate ventricular suction makes the hybrid mock circulation well suited for the testing of physiological VAD controllers. Aside from the Deltastream DP2, other blood pumps were successfully tested with the hybrid mock circulation, namely the PVAD (Thoratec Corporation, Pleasanton, CA, USA), the Excor (Berlin Heart GmbH, Berlin, Germany), and the HVAD (HeartWare Inc., Framingham, MA, USA). However, because the PVAD and the Excor are a pulsatile VADs and because the HVAD only allows manual speed control, none of these pumps could be combined with the PRS controller.
The PRS controller has proven to be a simple and effective algorithm for the physiological adaptation of VADs in vitro. In contrast to other physiological controllers that we implemented and tested on our mock circulation, the PRS controller requires very little tuning and is much simpler to implement. Its greatest advantage, however, is the combination of its being based on a physiological concept (PRSW), while still representing a classical control element (proportional controller). Most other physiological control algorithms are either solutions to an abstract regulator problem without any physiological meaning, or are implemented by if-then-else rules that do not allow for a proper stability analysis as it is presented in the current thesis.

6.2 Outlook

The most important problem that the hybrid mock circulation is faced with is the changing fluid viscosity. Flow observers, which estimate the pump flow based on the motor speed and current, are highly sensitive to blood viscosity. Currently, the fluid viscosity in the hybrid mock circulation is defined by the mixture ratio of glycerol and water. However, the viscosity of this fluid depends on its temperature, which is influenced by the ambient temperature in the laboratory and the operation of the mock circulation. Therefore, since the viscosity in the mock circulation changes constantly, it is not possible to develop a flow observer. In order to overcome this problem in the future, we plan to implement a temperature controller in the mock circulation. By keeping the temperature constant, the viscosity can be kept constant as well. In addition, once the temperature dependency of the viscosity of the fluid is known, the reference temperature can be used to achieve various desired viscosity values with the same mixture ratio of glycerol and water.

Thus far, no experiments have been conducted in vivo, however, such experiments are inevitable for the further development of the PRS controller. Especially the PPLUT and the HR and EDV detection algorithms, which have been developed based on in vitro experiments with the Deltastream DP2 pump, have to be reevaluated once in vitro experiments are conducted. The PPLUT has to be remeasured if the pump or the tubing is changed, and its lower and upper speed limits have to be redefined based on safety or energy consumption concerns. Furthermore, the two versions of HR and EDV detection algorithm will have to be tested with a measured LV volume signal. Due to the results of the stability analysis described in the current thesis, the focus will be on the simplified HR and EDV detection algorithm.

One of the obstacles on the way of using the PRS controller clinically is the required LV volume sensor. While a number of LV volume sensors for animal experiments are available on the market, none of them currently are ready to be used in humans. Therefore, we are in the process of developing an LV volume sensor based on ultrasound transducers integrated in the inlet cannula of a VAD. While this approach seems promising, a great effort will be required to make this sensor ready to be used in humans.

Bibliography

[1] A. C. Guyton and J. E. Hall, *Textbook of Medical Physiology, 12th Edition.* Saunders, 2010.

[2] S. M. Toy, J. Melbin, and A. Noordergraaf, "Reduced models of arterial systems," *IEEE Trans. Biomed. Eng.*, vol. 32, pp. 174–176, 1985.

[3] A. M. Katz, "Ernest Henry Starling, his predecessors, and the 'law of the heart'," *Circ.*, vol. 106, pp. 2986–2992, 2002.

[4] D. D. Glower, J. A. Spratt, N. D. Snow, J. S. Kabas, J. W. Davis, C. O. Olsen, G. S. Tyson, D. C. Sabiston Jr., and J. S. Rankin, "Linearity of the Frank-Starling relationship in the intact heart: the concept of preload recruitable stroke work," *Circ.*, vol. 71, pp. 994–1009, 1985.

[5] V. L. Roger, "Epidemiology of heart failure," *Circ. Res.*, vol. 113, pp. 646–659, 2013.

[6] A. L. Bui, T. B. Horwich, and G. C. Fonarow, "Epidemiology and risk profile of heart failure," *Nat. Rev. Cardiol.*, vol. 8, pp. 30–41, 2011.

[7] D. Malaquin and C. Tribouilloy, "Epidemiology of heart failure," *Rev. Practicien*, vol. 60, p. 911, 2010.

[8] M. Jessup and S. Brozena, "Heart failure," *N. Eng. J. Med.*, vol. 348, pp. 2007–2018, 2003.

[9] M. Strüber, A. Meyer, D. Malehsa, C. Kugler, A. Simon, and A. Haverich, "The current status of heart transplantation and the development of artificial heart systems," *Dtsch. Ärztebl. Int.*, vol. 106, pp. 471–477, 2009.

[10] D. Timms, "A review of clinical ventricular assist devices," *Med. Eng. Phys.*, vol. 33, pp. 1041–1047, 2011.

[11] J. K. Kirklin, D. C. Naftel, R. L. Kormos, L. W. Stevenson, F. D. Pagani, M. A. Miller, J. T. Baldwin, and J. B. Young, "Fifth intermacs annual report: Risk factor analysis from more than 6,000 mechanical circulatory support patients," *J. Heart Lung Transplant.*, vol. 32, pp. 141–156, 2013.

[12] E. J. Birks, P. D. Tansley, J. Hardy, R. S. George, C. T. Bowles, M. Burke, N. R. Banner, A. Khaghani, and M. H. Yacoub, "Left ventricular assist device and drug therapy for the reversal of heart failure," *N. Engl. J. Med.*, vol. 355, pp. 1873–84, 2006.

[13] D. J. Kozik and M. D. Plunkett, "Mechanical circulatory support," *Organogenesis*, vol. 7, pp. 50–63, 2011.

[14] D. J. Farrar, P. G. Compton, J. H. Lawson, J. J. Hershon, and J. D. Hill, "Control modes of a clinical ventricular assist device," *IEEE Eng. Med. Biol.*, vol. 5, no. 1, pp. 19–25, 1986.

[15] M. Vollkron, H. Schima, L. Huber, R. Benkowski, G. Morello, and G. Wieselthaler, "Development of a reliable automatic speed control system for rotary blood pumps," *J. Heart Lung Transplant.*, vol. 24, pp. 1878–1885, 2005.

[16] G. Giridharan, G. Pantalos, S. Koenig, K. Gillars, and M. Skliar, "Achieving physiologic perfusion with ventricular assist devices: Comparison of control strategies," in *Proc. American Control Conference, 2005*, 2005, pp. 3823–3828.

[17] H. Schima, W. Trubel, A. Moritz, G. Wieselthaler, H. G. Stohr, H. Thoma, U. Losert, and E. Wolner, "Noninvasive monitoring of rotary blood pumps: Necessity, possibilities, and limitations," *Artif. Organs*, vol. 16, pp. 195–202, 1992.

[18] M. Pillon, H. Duffour, and M. Jufer, "In vitro experiments: Circulatory assist device interaction with a virtual cardiovascular system," in *Proc. 14th Annual International Conference of the IEEE-EMBS*, 1992, pp. 740–741.

[19] F. M. Colacino, M. Arabia, G. A. Danieli, F. Moscato, S. Nicosia, F. Piedimonte, P. Valigi, and S. Pagnottelli, "Hybrid test bench for

evaluation of any device related to mechanical cardiac assistance," *Int. J. Artif. Organs*, vol. 28, pp. 817–826, 2005.

[20] G. Ferrari, M. Kozarski, C. De Lazzari, K. Gorczynska, G. Tosti, and M. Darowski, "Development of a hybrid (numerical-hydraulic) circulatory model: Prototype testing and its response to IABP assistance," *Int. J. Artif. Organs*, vol. 28, pp. 750–759, 2005.

[21] G. Ochsner, R. Amacher, A. Amstutz, A. Plass, M. Schmid Daners, H. Tevaearai, S. Vandenberghe, M. J. Wilhelm, and L. Guzzella, "A novel interface for hybrid mock circulations to evaluate ventricular assist devices," *IEEE Trans. Biomed. Eng.*, vol. 60, pp. 507–516, 2013.

[22] G. Ochsner, R. Amacher, and M. Schmid Daners, "Emulation of ventricular suction in a hybrid mock circulation," in *Proc. of the 12th European Control Conference, 2013*, 2013, pp. 3108–3112.

[23] G. Ochsner, R. Amacher, M. J. Wilhelm, S. Vandenberghe, H. Tevaearai, A. Plass, A. Amstutz, V. Falk, and M. Schmid Daners, "A physiological controller for turbodynamic ventricular assist devices based on a measurement of the left ventricular volume," *Artif. Organs*, 2013.

[24] R. Amacher, G. Ochsner, A. Ferreira, S. Vandenberghe, and M. Schmid Daners, "A robust reference signal generator for synchronized ventricular assist devices," *IEEE Trans. Biomed. Eng.*, vol. 60, no. 8, pp. 2174–2183, 2013.

[25] R. Amacher, J. Asprion, G. Ochsner, H. Tevaearai, M. J. Wilhelm, A. Plass, A. Amstutz, S. Vandenberghe, and M. Schmid Daners, "Numerical optimal control of turbo dynamic ventricular assist devices," *Bioeng.*, vol. 1, pp. 22–46, 2014.

[26] R. Amacher, G. Ochsner, and M. Schmid Daners, "Synchronized pulsatile speed control of turbodynamic left ventricular assist devices: Review and prospects," *Artif. Organs*, 2014.

[27] S. E. Jahren, G. Ochsner, F. Shu, R. Amacher, J. F. Antaki, and S. Vandenberghe, "Analysis of pressure head-flow loops of pulsatile rotodynamic blood pumps," *Artif. Organs*, vol. 38, pp. 316–326, 2014.

[28] R. Amacher, "Optimization of cardiac-cycle synchronized control for ventricular assist devices," Ph.D. dissertation, Diss., Eidgenössische Technische Hochschule ETH Zürich, Nr. 21702, 2014.

[29] P. Verdonck, A. Kleveln, R. Verhoeven, B. Angelsen, and J. Vandenbogaerde, "Computer-controlled in vitro model of the human left heart," *Med. & Biol. Eng. & Comput.*, vol. 30, pp. 656–659, 1992.

[30] P. Segers, F. Dubois, D. D. Wachter, and P. Verdonck, "Role and relevancy of a cardiovascular simulator," *CVE*, vol. 3, pp. 48–56, 1998.

[31] O. Dur, M. Lara, D. Arnold, S. Vandenberghe, B. B. Keller, C. DeGroff, and K. Pekkan, "Pulsatile in vitro simulation of the pediatric univentricular circulation for evaluation of cardiopulmonary assist scenarios," *Artif. Organs*, vol. 33, pp. 967–976, 2009.

[32] D. L. Timms, S. D. Gregory, N. A. Greatrex, M. J. Pearcy, J. F. Fraser, and U. Steinseifer, "A compact mock circulation loop for the in vitro testing of cardiovascular devices," *Artif. Organs*, vol. 35, pp. 384–391, 2010.

[33] S. Vandenberghe, F. Shu, D. K. Arnold, and J. F. Antaki, "A simple, economical, and effective portable paediatric mock circulatory system," in *Proc. Inst. Mech. Eng. H.*, 2011, pp. 648–656.

[34] G. Ferrari, C. De Lazzari, R. Mimmo, G. Tosti, D. Ambrosi, and K. Gorczynska, "A computer controlled mock circulatory system for mono- and biventricular assist device testing," *Int. J. Artif. Organs*, vol. 21, pp. 26–36, 1998.

[35] L. A. Baloa, J. R. Boston, and J. F. Antaki, "Elastance-based control of a mock circulatory system," *Ann. Biomed. Eng.*, vol. 29, pp. 244–251, 2001.

[36] M. Kozarski, G. Ferrari, F. Clemente, K. Groczynska, C. D. Lazzari, M. Darowski, R. Mimmo, G. Tosti, and M. Guaragno, "A hybrid mock circulatory system: Development and testing of an electro-hydraulic impedance simulator," *Int. J. Artif. Organs*, vol. 26, pp. 53–63, 2003.

[37] M. Loh and Y.-C. Yu, "Feedback control design for an elastance-based mock circulatory system," in *Proc. 2004 American Control Conference*, 2004, pp. 1639–1644.

[38] M. Vaes, M. Rutten, R. van de Molengraft, and F. van de Vosse, "Left-ventricular assist device evaluation with a model-controlled mock circulation," in *Proc. ASME 2007 Summer Bioengineering Conference (SBC2007)*, 2007.

[39] F. M. Colacino, F. Moscato, F. Piedimonte, G. A. Danieli, S. Nicosia, and M. Arabia, "A modified elastance model to control mock ventricles in real-time: Numerical and experimental validation," *Asaio J.*, vol. 54, pp. 563–573, 2008.

[40] K.-W. Gwak, B. E. Paden, J. F. Antaki, and I.-S. Ahn, "Experimental verification of the feasibility of the cardiovascular impedance simulator," *IEEE Trans. Biomed. Eng.*, vol. 57, pp. 1176–1183, 2010.

[41] Y. Yokoyama, O. Kawaguchi, T. Shinshi, U. Steinseifer, and S. Takatani, "A new pulse duplicator with a passive fill ventricle for analysis of cardiac dynamics," *J. Artif. Organs*, vol. 13, pp. 189–196, 2010.

[42] F. Moscato, G. A. Danieli, and H. Schima, "Dynamic modeling and identification of an axial flow ventricular assist device," *Int. J. Artif. Organs*, vol. 32, pp. 336–343, 2009.

[43] F. M. Colacino, F. Moscato, F. Piedimonte, M. Arabia, and G. A. Danieli, "Left ventricle load impedance control by apical VAD can help heart recovery and patient perfusion: A numerical study," *Asaio J.*, vol. 53, pp. 263–277, 2007.

[44] L. Guzzella, *Analysis and Synthesis of Single-Input Single-Output Control Systems*. Vdf Hochschulverlag AG, 2011.

[45] H. K. Khalil, *Nonlinear Systems*. Prentice-Hall, 1996.

[46] S. Choi, J. F. Antaki, J. R. Boston, and D. Thomas, "A sensorless approach to control of a turbodynamic left ventricular assist system," *IEEE Trans. Control Syst. Technol.*, vol. 9, pp. 473–482, 2001.

[47] F. Moscato, M. Vollkron, H. Bergmeister, G. Wieselthaler, E. Leonard, and H. Schima, "Left ventricular pressure-volume loop analysis during continuous cardiac assist in acute animal trials," *Artif. Organs*, vol. 31, pp. 369–376, 2007.

[48] A. L. Ferreira, Y. Wang, J. Gorcsan, and J. F. Antaki, "Assessment of cardiac function during mechanical circulatory support: the quest for a suitable clinical index," in *Proc. 33rd Annual International Conference of the IEEE EMBS*, 2011, pp. 223–226.

[49] D. Morley, K. Litwak, P. Ferber, P. Spence, R. Dowling, B. Meyns, B. Griffith, and D. Burkhoff, "Hemodynamic effects of partial ventricular support in chronic heart failure: Results of simulation validated with in vivo data," *J. Thorac. Cardiov. Surg.*, vol. 133, pp. 21–28, 2007.

[50] P. Naiyanetr, F. Moscato, M. Vollkron, D. Zimpfer, G. Wieselthaler, and H. Schima, "Continuous assessment of cardiac function during rotary blood pump support: A contractility index derived from pump flow," *J. Heart Lung Transplant.*, vol. 29, pp. 37–44, 2010.

[51] G. A. Giridharan, G. M. Pantalos, K. J. Gillars, S. C. Koenig, and S. Mikhail, "Physiologic control of rotary blood pumps: An in vitro study," *Asaio J.*, vol. 50, pp. 403–409, 2004.

[52] S. Skogestad and I. Postlethwaite, *Multivariable Feedback Control.* Wiley, 2005.

[53] K.-W. Gwak, M. Ricci, S. Snyder, B. E. Paden, J. R. Boston, M. A. Simaan, and J. F. Antaki, "In-vitro evaluation of multi-objective hemodynamic control of heart-assist pump," in *Proc. of the 43rd IEEE Conference on Decision and Control*, 2004, pp. 1069–1074.

[54] A. Ferreira, J. R. Boston, and J. F. Antaki, "A control system for rotary blood pumps based on suction detection," *IEEE Trans. Biomed. Eng.*, vol. 56, pp. 656–665, 2009.

[55] K.-W. Gwak, J. F. Antaki, B. E. Paden, and B. H. Kang, "Safety-enhanced optimal control of turbodynamic blood pumps," *Artif. Organs*, vol. 35(7), pp. 725–732, 2011.

[56] L. A. Baloa, D. Liu, J. R. Boston, M. A. Simaan, and J. F. Antaki, "Control of rotary heart assist devices," in *Proc. of the American Control Conference*, 2000, pp. 2982–2986.

[57] J. R. Boston, M. A. Simaan, J. F. Antaki, and Y.-C. Yu, "Control issues in rotary heart assist devices," in *Proc. 2000 American Control Conference*, 2000, pp. 3473–3477.

[58] D. V. Amin, J. F. Antaki, P. Litwak, D. Thomas, Z. Wu, Y. C. Yu, S. Choi, J. R. Boston, and B. P. Griffith, "Controller for an axial-flow blood pump," *Biomed. Instrum. Techn.*, vol. 31, pp. 483–487, 1997.

[59] T. Iijima, T. Inamoto, M. Nogawa, and S. Takatani, "Control of centrifugal blood pump based on the motor current," *Artif. Organs*, vol. 21, pp. 655–660, 1997.

[60] Y. Takami, G. Otsuka, J. Mueller, Y. Ohashi, E. Tayama, H. Schima, H. Schmallegger, E. Wolner, and Y. Nos, "Flow characteristics and required control algorithm of an implantable centrifugal left ventricular assist device," *Heart Vessels*, vol. 12, pp. 92–97, 1997.

[61] K. Araki, M. Oshikawa, T. Onitsuka, K. Nakamura, H. Anai, and H. Yoshihara, "Detection of total assist and sucking points based on the pulsatility of a continuous flow artificial heart: in vitro evaluation," *Asaio J.*, vol. 44, pp. 708–711, 1998.

[62] A. Yukhi, E. Hatoh, M. Nogawa, M. Miura, Y. Shimazaki, and S. Takatani, "Detection of suction and regurgitation of the implantable centrifugal pump based on the motor current waveform analysis and its application to optimization of pump flow," *Artif. Organs*, vol. 26, pp. 532–537, 1999.

[63] M. Oshikawa, K. Araki, G. Endo, H. Anai, and M. Sato, "Sensorless controlling method for a continuous flow left ventricular assist device," *Artif. Organs*, vol. 24, pp. 600–605, 2000.

[64] K. Nakata, M. Yoshikawa, T. Takano, Y. Sankai, G. Ohtsuka, J. Glueck, A. Fujisawa, K. Makinouchi, M. Yokokawa, S. Nosaka, and Y. Nose, "Control system for an implantable rotary blood pump," *Ann. Thorac. Cardiovasc. Surg.*, vol. 6, pp. 242–246, 2000.

[65] M. Vollkron, H. Schima, L. Huber, R. Benkowski, G. Morello, and G. Wieselthaler, "Development of a suction detection system for axial blood pumps," *Artif. Organs*, vol. 28, no. 8, pp. 709–716, 2004.

[66] G. Endo, K. Araki, M. Oshikawa, K. Kojima, T. Saitoh, K. Nakamura, and T. Onitsuka, "Control strategy for biventricular assistance with mixed-flow pumps," *Artif. Organs*, vol. 24, pp. 594–599, 2000.

[67] K.-W. Gwak, "Application of extremum seeking control to turbodynamic blood pumps," *Asaio J.*, vol. 53, pp. 403–409, 2007.

[68] A. Arndt, P. Nüsser, K. Graichen, J. Müller, and B. Lampe, "Physiological control of a rotary blood pump with selectable therapeutic options: Control of pulsatility gradient," *Artif. Organs*, vol. 32, pp. 761–771, 2008.

[69] S. Choi, J. R. Boston, and J. F. Antaki, "Hemodynamic controller for left ventricular assist device based on pulsatility ratio," *Artif Organs*, vol. 31(2), pp. 114–125, 2007.

[70] H. Konishi, J. F. Antaki, D. V. Amin, R. Boston, J. P. Kerrigan, W. A. Mandarino, P. Litwak, K. Yamazaki, M. Macha, K. C. Butler, H. S. Borovetz, and R. L. Kormos, "Controller for an axial flow blood pump," *Artif. Organs*, vol. 20, pp. 618–620, 1996.

[71] T. Waters, P. Allaire, G. Tao, M. Adams, G. Bearnson, N. Wei, E. Hilton, M. Baloh, D. Olsen, and P. Khanwilkar, "Motor feedback physiological control for a continuous flow ventricular assist device," *Artif. Organs*, vol. 23, pp. 480–486, 1999.

[72] E. Bullister, S. Reich, and J. Sluetz, "Physiologic control algorithms for rotary blood pumps using pressure sensor input," *Artif. Organs*, vol. 26, pp. 931–938, 2002.

[73] G. A. Giridharan and M. Skliar, "Physiological control of blood pumps using intrinsic pump parameters: A computer simulation study," *Artif. Organs*, vol. 30(4), pp. 301–307, 2006.

[74] Y. Wu, P. E. Allaire, G. Tao, and D. Olsen, "Modeling, estimation, and control of human circulatory system with a left ventricular assist device," *IEEE Trans. Contr. Syst. Tech.*, vol. 15(4), pp. 754–767, 2007.

[75] K. Ohuchi, D. Kikugawa, K. Takahashi, M. Uemura, M. Nakamura, T. Murakami, T. Sakamoto, and S. Takatani, "Control strategy for rotary blood pumps," *Artif. Organs*, vol. 25, no. 5, pp. 366–370, 2001.

[76] J. F. Antaki, J. R. Boston, and M. A. Simaan, "Control of heart assist devices," in *Proc. 42nd IEEE Conference on Decision and Control, 2003*, 2003, pp. 4084–4089.

[77] J. Boston, J. Antaki, and M. Simaan, "Hierarchical control of heart-assist devices," *IEEE Trans. Robot Autom.*, vol. 10, pp. 54–64, 2003.

[78] M. Takeuchi, M. Odake, H. Takaoka, Y. Hayashi, and M. Yokoyama, "Comparison between preload recruitable stroke work and the end-systolic pressure-volume relationship in man," *Eur. Heart J.*, vol. 13, pp. 80–84, 1992.

[79] M. Andersen, R. Videbk, S. Boesgaard, K. Sander, P. B. Hansen, and F. Gustafsson, "Incidence of ventricular arrhythmias in patients on long-term support with a continuous-flow assist device (HeartMate II)," *J. Heart Lung Transplant.*, vol. 28, pp. 733–735, 2009.

[80] H. Schima, M. Vollkron, U. Jantsch, R. Crevenna, W. Roethy, R. Benkowski, G. Morello, M. Quittan, M. Hiesmayr, and G. Wieselthaler, "First clinical experience with an automatic control system for rotary blood pumps during ergometry and right-heart catheterization," *J. Heart Lung Transplant.*, vol. 25, pp. 167–173, 2006.

[81] A. L. Fradkov and A. Y. Pogromsky, *Introduction to control of oscillations and chaos*. World Scientific, 1998, vol. 35.